

Analysis of Structures in the Magellanic Clouds with Minkowski Tensors

Master's Thesis in Physics

Presented by
Caroline Collischon
7. April 2020

Friedrich-Alexander-Universität Erlangen-Nürnberg



Supervisors: Prof. Dr. Klaus Mecke
Prof. Dr. Manami Sasaki

Abstract

In this thesis, I develop morphometric data analysis methods for the detection of stellar bubbles with Minkowski tensors. Minkowski functionals and their generalization to tensors are shape descriptors from integral geometry. They characterize all additive shape information of unions of convex bodies, like in pixelated black and white images. Grayscale images can be analyzed by choosing a brightness threshold to define a discrete body and calculating them in a marching square. By averaging the resulting maps for several thresholds and smoothing, one obtains a Minkowski map at the smoothing window size. The irreducible Minkowski tensor ψ_2 responds to elongated structures such as filaments and using its phase, lines perpendicular to the filaments are drawn.

Regions of high line density at a chosen smoothing window size show areas where structures of similar size should originate. Centers of bubbles then appear as regions of increased line density where the lines from the border meet. Additionally, the scale normalized $|\psi_2|$ falls or stagnates when increasing the window size. These two criteria are used to successfully detect bubbles in $H\alpha$, SII, and OIII images of the Magellanic Clouds. Noise impairs the detection, but leaving more noise in the images proves to be better than smoothing or choosing higher thresholds. The parameters need to be adjusted manually, but impressive results can be achieved without time-consuming optimization.

Bubbles are created by massive stars, so their respective distributions should be correlated. Methods of spatial statistics, so-called marked correlation functions, are used to compare the point patterns of detected bubbles and massive stars in the catalog of Bonanos et al. (2009). It is found that bubbles detected in $H\alpha$, SII, and OIII correlate with the stars as expected. The distribution of detected bubbles should thus represent the actual distribution of bubbles well. Line density maps at intermediate (70 px, 11.7', 170 pc) and large scales (250 px, 41.7', 600 pc) were also compared to the stellar distribution. The OIII data show the strongest correlation in both cases due to the more localized emission around present-day stars. The SII line densities do not correlate with the stars at any scale. The emission is more extended than the modern stellar distribution and likely older than the stars in the catalog. $H\alpha$ correlates with the stars at 70 px, but not at 250 px, showing smaller, younger structures and larger older ones.

Additionally, a possible correlation of line densities at larger scales and supergiant shells is found. All nine LMC shells (Meaburn, 1980) contain or directly border a local maximum of line density. The small sample size does not allow for a more precise statement. The line density may correlate to recent star formation in general.

Contents

1	Astronomical background	1
1.1	Selected diffuse emission regions	1
1.2	The Magellanic Clouds	3
2	Image analysis with Minkowski tensors	7
2.1	Basics and definitions	7
2.1.1	Minkowski functionals	7
2.1.2	Minkowski tensors	8
2.2	Threshold-dependent MF/MT	10
2.3	Minkowski map algorithm	10
2.4	Bubble detection	12
2.4.1	Line density condition	12
2.4.2	Falling $ \psi_2 $ condition	13
2.4.3	Parameter estimation	13
2.4.4	Preparation for statistical analysis	15
2.5	Large-scale structure	19
2.6	SMC bubble detection	21
2.6.1	Noise dependence of ψ_2 and bubbles	24
3	Statistical and astronomical analysis	33
3.1	Basics of point process statistics	33
3.1.1	Marked point processes	33
3.1.2	Intensity	33
3.1.3	Summary characteristics	34
3.2	Comparison to distribution of massive stars	34
3.2.1	Random superposition test	34
3.2.2	Application of correlation test	36
3.3	Notable individual regions	42
3.3.1	Supergiant shells, line density and star formation	42
3.3.2	Line density and SMC X-ray emission	45
4	Summary and Outlook	47
A	Detected bubble tables	53
A.1	LMC	53
A.2	SMC	56
B	banana documentation	63
C	banana graphs and images	67
C.1	Bubbles	67
C.2	Non-bubbles	75
D	Statistical analysis graphs	83

Chapter 1

Astronomical background

1.1 Selected diffuse emission regions

The interstellar medium (ISM) is composed of gas and dust between stars. It has been found to consist of three phases (McKee and Ostriker, 1977; Cox, 2005): A mostly hot phase with low density ($T \sim 10^6$ K, $n \lesssim 10^{-2} \text{ cm}^{-3}$), a warm intermediate-density phase ($T \sim 10^4$ K, $n \sim 0.1 - 1 \text{ cm}^{-3}$), and a phase of cold dense clouds ($T \sim 10^2$ K, $n \sim 10 \text{ cm}^{-3}$). The hot phase is heated and ionized by the winds of massive stars and supernova remnants (SNRs); the warm phase is partially ionized by soft stellar X-rays and UV radiation. Estimations and observations show that the majority of the volume is occupied by the low-density phase in large tunnels and cavities (Cox, 2005).

The relevant objects in this thesis are closely related to the heating of the warm and hot regions: stellar bubbles, superbubbles, and supergiant shells blown into the surrounding medium by massive stars. They are discussed in further detail below. The related H II regions and a few selected emission lines are introduced along with the Magellanic Clouds as the objects of investigation.

The main aim of this thesis is the automatic detection of bubbles and superbubbles using the so-called Minkowski tensors, which are introduced starting in section 2.1. An algorithm to detect bubbles is presented in section 2.4 and the following sections describe its usability and noise tolerance. Chapter 3 contains a comparison of the spatial distribution of the bubbles in the Large Magellanic Cloud and the large-scale structure to the distribution of massive stars. Further notable astronomical correlations are discussed in section 3.3. The results are summarized in chapter 4.

H II regions

Massive stars can create structures in the surrounding medium by photoionization, stellar winds, and supernova explosions. Photoionization is mostly relevant for H II regions¹.

These regions form out of giant molecular clouds with massive star formation (Anderson et al., 2009). The newly formed stars emit UV radiation, ionizing the surrounding medium and dissociating molecules in an ionization front (Hollenbach and Tielens, 1997). Since the radiation is densest in the center of the region, higher ionization states are found more closely around the central stars (see e.g. Osterbrock 1988 for a review of emission line observations). Over time, a supersonic shock front forms due to the pressure gradient between the heated gas and the cold surrounding region and passes the ionization front. The velocity difference depends on the cloud density gradient and may become zero for steeply falling density. Then, the H II region expands supersonically (Franco et al., 1990). Franco et al. (1990) also found that H II regions at cloud boundaries leak out ionizing radiation into the interstellar medium.

¹Astronomic ion notation gives the name of the element and its charge plus one in roman numerals, e.g. C IV refers to C^{3+}

Optically, H II regions can be observed by their H α emission, which comes from a transition in excited atomic hydrogen after photoionization and recombination. Other popular lines that will be used in this work are the forbidden emission lines [O III] λ 5007 (from now on OIII) and [S II] λ 6731, 6716 (from now on SII). Due to their low radiative transition probability, they are collisionally excited by electrons and slowly radiatively de-excited if the density is too low for collisional de-excitation.

The OIII line is caused by a transition between two excited states in doubly ionized oxygen. Because of its double charge, it is found closer to the ionizing stars. In the Galactic warm ionized medium, only faint OIII background emission is found (Reynolds, 1985).

SII is usually found in shock heated environments (see e.g. Osterbrock and Ferland 2006). This is because in photoionized H II regions the sulfur is further ionized into the S $^{++}$ state. In shock-heated regions such as SNRs, the shock front collisionally heats the gas to high temperatures and higher ionization states out of thermodynamic equilibrium. The ions then recombine to lower states such as S $^+$ over time. The electron density and temperature is sufficient to create the observed SII emission.

The SII emission relative to H α is used to distinguish H II regions from SNRs. SNRs are expected to have higher SII/H α ratios than H II regions, usually higher than 0.5 (Fesen et al., 1985; Mathewson et al., 1985; Filipovic et al., 1998; Stupar et al., 2018).

Stellar bubbles and superbubbles

Stellar winds and supernovae will blow hot bubbles into the surrounding ISM. The former consist of mass lost by massive stars at rates on the order of $10^{-6} M_{\odot}/\text{yr}$ (Castor et al., 1975). This mass loss is driven by both elastic Thomson scattering between photons coming from the star and particles in the atmosphere, and line-driving. In the latter, a photon is absorbed and then re-emitted in a random direction, yielding an average momentum away from the star. Further away from the star the stellar wind creates a shock wave as it compresses the ISM.

Weaver et al. (1977) created an analytic description of such a stellar wind-blown bubble surrounded by uniform cold gas. They divide the ensuing bubble into several shells. In the innermost part, the wind expands adiabatically. Further out the wind is shocked adiabatically into a hot shell pushing onto a warm shell of compressed interstellar medium. Thermal conduction takes place between the two and the warm shell evaporates into the hot region. The bubbles may reach sizes of up to several tens of parsecs.

This model, although simplistic, has been the basis for many more complex descriptions of stellar bubbles. It has become clear that effects such as stellar evolution into later stages with stronger winds and clumps in the surrounding medium greatly affect the bubble (for a review see Chu 2008).

Bubbles powered by winds and supernova explosions of several stars are called superbubbles. As the supernova blast waves are decelerated inside before reaching the shell, superbubble models can be based on the models of wind-blown bubbles (Mac Low and McCray, 1988). They reach sizes on the order of 10^2 pc and ages of $\sim 10^6$ yr (Chu, 2008). In general, the analytic models fit reasonably well, but the size is often smaller than expected (Oey, 2007). Possible reasons for this include overestimation of input power or underestimation of ambient density, pressure, or radiative cooling.

Supergiant shells

Supergiant shells (SGS) are formed over several generations of star formation and reach sizes of more than 1000 pc (Chu, 2008). They may contain superbubbles and bubbles. Meaburn (1980) found nine supergiant shells in the Large Magellanic Cloud in H α images.

A prominent example showing the size differences is the LMC SGS 4, whose edges contain various younger superbubbles and bubbles. Images demonstrating the size differences and gen-

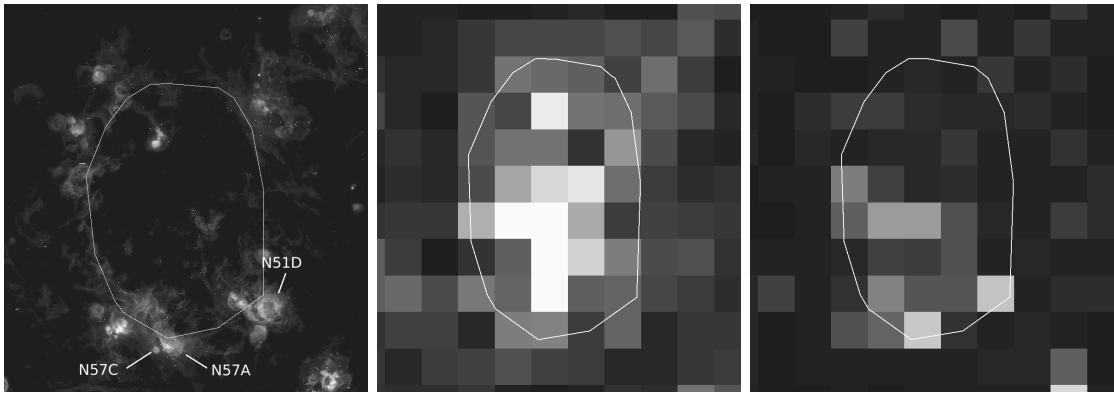


Figure 1.1: Left: The LMC SGS 4 in $H\alpha$ (white contour) with selected superbubbles LHA 120-N51D and -N57A, and bubble LHA 120-N57C for size comparison (inspired by Chu 2008, Fig. 1). Center: The star formation rate in the region 20 Myr ago. Right: Star formation rate 7 Myr ago. Movement of star formation from the center of the SGS to the modern superbubbles is visible. Star formation rates taken from the star formation history by Harris and Zaritsky (2009).

erations of star formation are shown in Fig. 1.1. 20 Myr ago, the star formation took place mainly in the center of SGS 4 and then moved to the present-day superbubbles LHA 120-N51D and LHA 120-N57A at the edge (Harris and Zaritsky, 2009).

1.2 The Magellanic Clouds

The Magellanic clouds are a pair of irregular dwarf galaxies orbiting the Milky Way. They are located in a direction far enough from the Galactic plane to make them good observation targets without large amounts of Galactic gas and dust in the line of sight. An image showing both clouds is given in Fig. 1.2.

The metallicity² of the Magellanic Clouds is significantly lower than the solar metallicity $Z_{\odot} = 0.142$ (Asplund et al., 2009): In the Large Magellanic Cloud (LMC) $Z_{\text{LMC}} \simeq 0.5 Z_{\odot}$ and in the Small Magellanic Cloud (SMC) $Z_{\text{SMC}} \simeq 0.2 Z_{\odot}$ (Russell and Dopita, 1992). This has an impact on many parameters such as the stellar mass-luminosity relation (e.g. Nadyozhin and Razinkova 2005) or mass-loss by stellar winds (e.g. Castor et al. 1975; Vink et al. 2001).

The LMC

The gas of the LMC is the main subject of this thesis. A view in $H\alpha$, SII, and OIII is shown in Fig. 1.3. These images stem from the UM/CTIO Magellanic Cloud Emission Line Survey (MCELS, Smith et al. 2000) and will be the basis for further analysis. One can easily see the more concentrated nature of OIII around certain brighter regions as opposed to SII and $H\alpha$.

It is viewed nearly face-on at an inclination angle of $\sim 33 - 45^{\circ}$ (Westerlund, 1997), making it simpler to observe its structure. Choi et al. (2018) suggest an even lower inclination angle of $25.86^{+0.73}_{-1.39}$ degrees and a twisted shape where different parts have different inclination angles. The overlap between different regions due to projection effects will not be treated as problematic here and different absolute sizes due to different distances will be neglected.

Its mean distance was determined by Pietrzyński et al. (2019) to be 49.59 ± 0.09 (statistical) ± 0.54 (systematic) kpc, which is relatively close.

²Metallicity Z is defined as the mass fraction of metals: $Z = \frac{m_{\text{metal}}}{m_{\text{tot}}}$. All elements heavier than Helium are referred to as metals.



Figure 1.2: The Magellanic Clouds (left: Small/right: Large Magellanic Cloud). Credit: ESO/S. Brunier

The LMC is an actively star-forming galaxy (Harris and Zaritsky, 2009). This means that there is a population of young massive stars. They have been described e.g. by Bonanos et al. (2009), who cataloged 1750 massive stars along with photometric data for 1268 of them. The catalog will be used for statistical analysis later in this thesis.

The SMC

The SMC is located at a distance of about 62 kpc (de Grijs and Bono, 2015). Unlike the LMC, it is viewed at a high inclination angle (Westerlund, 1997). Its extension along the line of sight gives it a more chaotic appearance, making the analysis of its images a greater challenge. A MCELS view in $H\alpha$, SII, and OIII is shown in Fig. 1.4. Just like the LMC, the SMC has been and is still forming stars (Harris and Zaritsky, 2004), leading to all related structures.

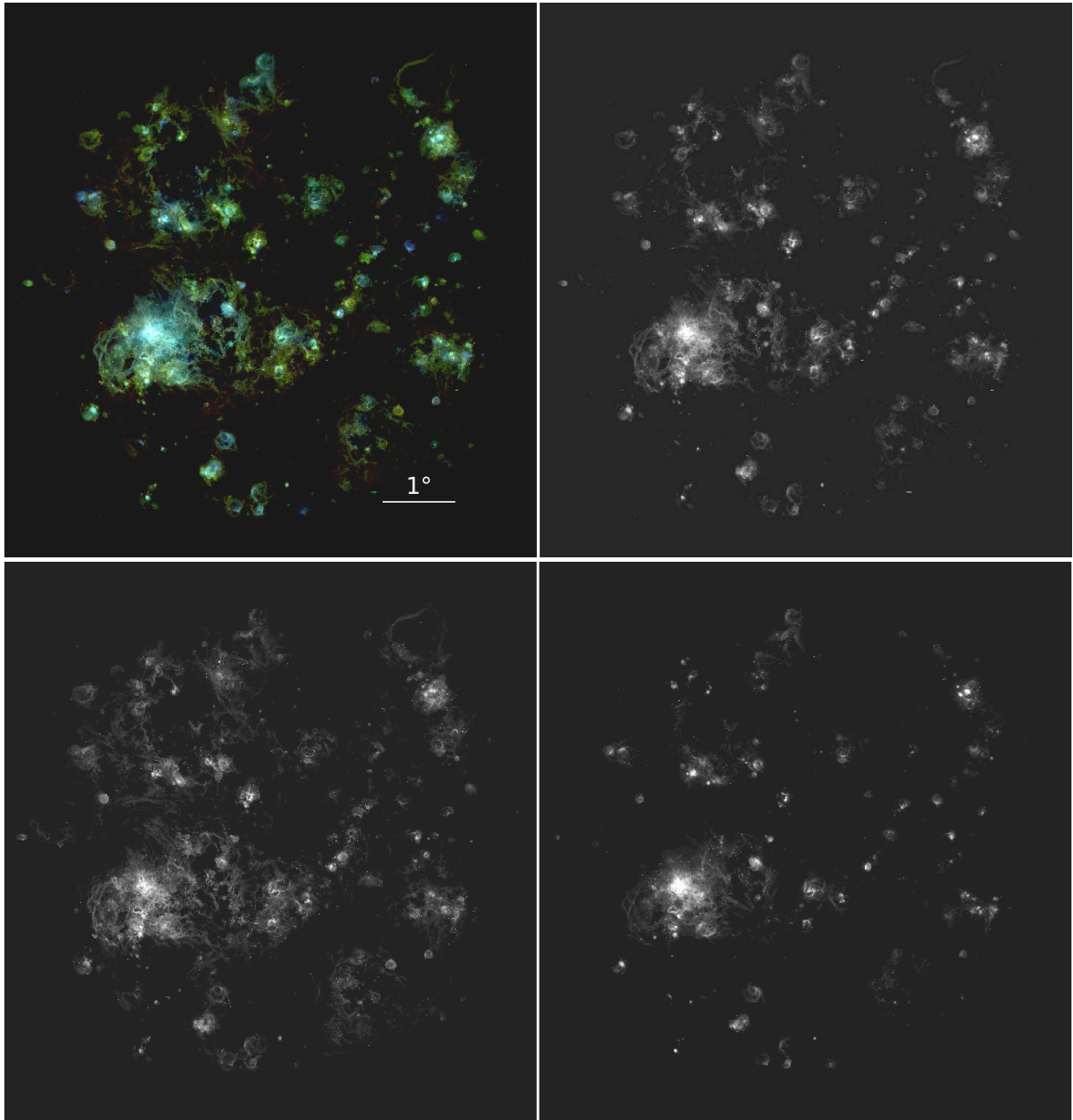


Figure 1.3: Top left: The LMC in SII (red), H α (green), OIII (blue). The 1 $^\circ$ line corresponds to a length of ~ 870 pc at a distance to the LMC of about 50 kpc (Pietrzyński et al., 2019). Top right: The LMC in H α . Bottom: The LMC in SII (left) and OIII (right). Images: MCELS, Smith et al. (2000).

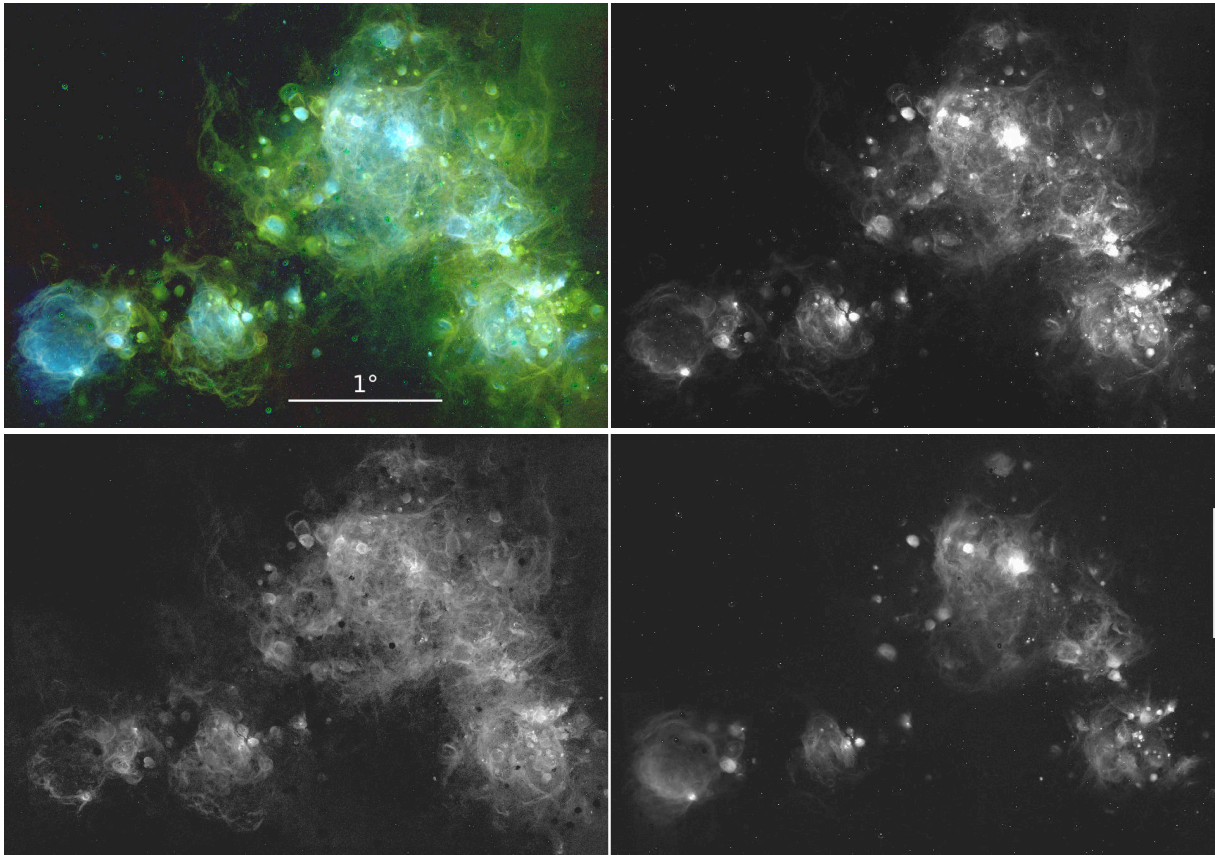


Figure 1.4: Top left: The SMC in SII (red), H α (green), OIII (blue). The 1° line at the bottom corresponds to a length of ~ 1.1 kpc at a distance to the SMC of about 62 kpc (de Grijs and Bono, 2015). Top right: The SMC in H α . Bottom: The LMC in SII (left) and OIII (right). Images: MCELS, Smith et al. (2000).

Chapter 2

Image analysis with Minkowski tensors

2.1 Basics and definitions

2.1.1 Minkowski functionals

Minkowski functionals (MF) are scalar shape indicators of compact bodies. Up to prefactors they are also known as quermassintegrale or intrinsic volumes (Hadwiger, 1957). They have been used e.g. for detecting extended sources in gamma ray sky maps of the H.E.S.S. telescope (Göring et al., 2013; Klatt and Mecke, 2019), exploring non-Gaussianity of the cosmic microwave background (e.g. Hikage and Matsubara 2012), or analyzing the large-scale morphology of galaxy distributions (e.g. Kerscher et al. 2001a,b).

For d -dimensional bodies there exist $d+1$ Minkowski functionals W_ν , in 2D (up to prefactors) given by area A , perimeter P , and Euler characteristic χ (the number of components minus the number of cavities for compact bodies). Expressed as integrals over a smooth body K or its contour ∂K they can be written as

$$W_0(K) = \int_K d^2r \quad \text{and} \quad W_\nu(K) := \frac{1}{2} \int_{\partial K} G_\nu dr \quad (2.1)$$

where $G_1 = 1$ and $G_2 = \kappa$, the local curvature of ∂K . One observes $A = W_0$, $P = 2W_1$, and $\chi = W_2/\pi$. In the case of convex polygons or other bodies with sharp edges or corners the curvature-dependent MF can be calculated by constructing the parallel or dilated body for $\varepsilon > 0$:

$$K_\varepsilon := \{x \in \mathbb{R}^n \mid \exists y \in K : \|x - y\| \leq \varepsilon\}. \quad (2.2)$$

The local curvature of this body is finite everywhere and MF of K can be obtained in the limit $\varepsilon \rightarrow 0$: $W_\nu(K) = \lim_{\varepsilon \rightarrow 0} W_\nu(K_\varepsilon)$. The volume $V_\varepsilon(K)$ of K_ε may be used for a more general definition of MF in d dimensions. Expressed as a series in ε one gets the Steiner formula:

$$V_\varepsilon(K) = \sum_{\alpha=0}^d \binom{d}{\alpha} W_\alpha(K) \varepsilon^\alpha \quad (2.3)$$

Non-convex bodies that are a finite union of convex bodies can be treated by decomposing them into their convex subsets. Then, the additivity property can be used:

$$W_\nu(K \cup K') = W_\nu(K) + W_\nu(K') - W_\nu(K \cap K') \quad (2.4)$$

for convex K, K' .

In general, Hadwiger's theorem states that any continuous, additive, and motion-invariant functional F of a convex body K can be expressed in terms of the MF (Hadwiger, 1957):

$$F(K) = \sum_{k=0}^d \alpha_k W_k(K) \quad (2.5)$$

This means the MF are a versatile and comprehensive way of describing a convex object's shape.

2.1.2 Minkowski tensors

Minkowski tensors (MT) are generalizations of the MF and can be used to characterize the anisotropy and orientation of objects. They can again be defined by integrals over the body and its boundary. Let \vec{r} be position and \vec{n} normal vectors of ∂K . Define the notation

$$\vec{r}^a \otimes \vec{n}^b := \underbrace{\vec{r} \otimes \dots \otimes \vec{r}}_{a \text{ times}} \otimes \underbrace{\vec{n} \otimes \dots \otimes \vec{n}}_{b \text{ times}} \quad (2.6)$$

using the symmetric tensor product $(\vec{x} \otimes \vec{x})_{ij} = x_i x_j$ and

$$(\vec{r}^a \otimes \vec{n}^b)_{i_1 \dots i_{a+b}} = \frac{1}{(a+b)!} \sum_{\sigma \in S_{a+b}} r_{i_{\sigma(1)}} \dots r_{i_{\sigma(a)}} \cdot n_{i_{\sigma(a+1)}} \dots n_{i_{\sigma(a+b)}}. \quad (2.7)$$

Here S_n is the permutation group of n elements. Then the MT of rank $a+b$ in 2D are given by

$$W_0^{a,0}(K) := \int_K \vec{r}^a d^2r \quad \text{and} \quad W_\nu^{a,b}(K) := \frac{1}{2} \int_{\partial K} \vec{r}^a \otimes \vec{n}^b G_\nu dr \quad (2.8)$$

Extension to bodies with edges or corners is again performed as for the scalar functionals. Note that the MT are in general not translation invariant due to the appearance of \vec{r} on the right-hand side of the equation. Additionally, there are linear dependencies among the MT and the MF (multiplied with the unit tensor). They have been treated more extensively in e.g. Schröder-Turk et al. (2013, 2010).

Some MT have well-known physical applications, for example the Minkowski vector $W_0^{1,0}/W_0$ is the center of mass of the body, assuming constant density. A more thorough description of the interpretation of specific MT is provided in Schröder-Turk et al. (2013).

In my work there is particular interest in the translation-invariant and hence origin-independent rank- s tensors $W_1^{0,s}(K) = \frac{1}{2} \int_{\partial K} \vec{n}^s dr$. Since anisotropy analysis with the tensors in this form involves the calculation of eigenvalue ratios and eigenvectors (Schröder-Turk et al., 2011), a more elegant approach is chosen here.

A useful reformulation of the above Cartesian MT are the irreducible Minkowski tensors (IMTs). They can be derived in 2D as follows:

Take a convex sufficiently smooth body with normal vector density $\rho_K(\varphi)$ with respect to direction φ . This means $\rho_K(\varphi)$ takes large values at φ if a large amount of the body's surface is directed perpendicular to that angle. An example shape and its normal density is shown in Fig.2.1. For a polygon with edges denoted by indices k with length L_k this reduces to $\rho_K(\varphi) = \sum_k L_k \delta(\varphi - \varphi_k)$.

The IMTs are then obtained by decomposition into representations of the rotation group, which in 2D is the Fourier transform of ρ :

$$\psi_s(K) = \int_0^{2\pi} d\varphi \exp(is\varphi) \rho_K(\varphi) \stackrel{\text{polygon}}{=} \sum_{k=-\infty}^{\infty} L_k \exp(is\varphi_k) \quad (2.9)$$

The case $s=0$ yields the perimeter (or $2 \cdot W_1$) and $\psi_1(K) = 0$ for closed bodies. The higher orders denote exactly s -fold symmetries. Figure 2.2 shows a series of bodies where $\psi_s(K) \neq 0$ for only one s , higher s leading to higher frequencies in ρ_K . With full knowledge of all ψ_s , the shape of the body can be reconstructed by recreating $\rho_K(\varphi)$ by Fourier transforming again.

The behavior under rotation $O(\alpha)$ at an angle α is the following:

$$\psi_s(O(\alpha)K) = \int_0^{2\pi} d\varphi \exp(is\varphi) \rho_K((\varphi + \alpha)) = \int_0^{2\pi} d\varphi \exp(is(\varphi - \alpha)) \rho_K(\varphi) = \psi_s(K) e^{-is\alpha} \quad (2.10)$$

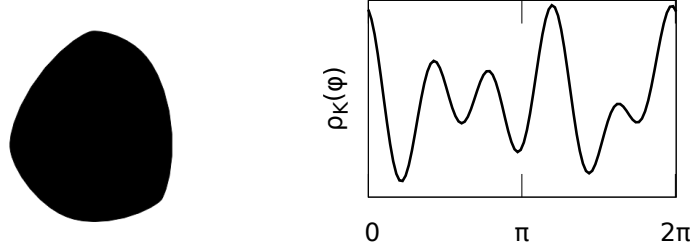


Figure 2.1: A convex body K and its normal density $\rho_K(\varphi)$.³ The minima of the density correspond to the “corners” of the body with high curvature. The maxima correspond to the almost flat regions of the contour.

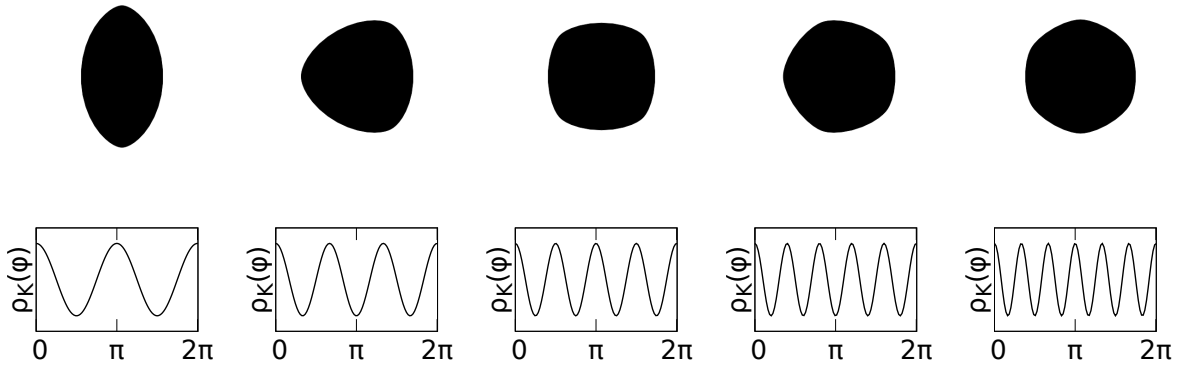


Figure 2.2: Top: Shapes with $\psi_s \neq 0$ for exactly one s and phase zero³. Bottom: Corresponding normal densities (arbitrary units). From left to right: $s = 2, 3, 4, 5, 6$. Since the ψ_s are Fourier coefficients of $\rho_K(\varphi)$, here the ρ_K are given by harmonic waves with increasing frequency.

The phase of ψ_s is changed by s times the rotation angle. This can be made plausible when looking at Fig. 2.2: A rotation at $\alpha = \frac{2\pi}{s}$ must yield the same value of ψ_s because of the s -fold symmetry. Additionally, s preferred directions where maxima of $\rho_K(\varphi)$ are located are at

$$\phi_n = \frac{2\pi n + \arg(\psi_s)}{s}, \quad n \in \{0, \dots, s-1\}. \quad (2.11)$$

As shown in equation 2.9 the IMTs are scaling linearly with the size of the body: $\psi_s(\lambda K) = \lambda \psi_s(K)$. In order to have scale-independent shape indices, it is suitable to consider the IMTs divided by the perimeter:

$$q_s = \frac{|\psi_s(K)|}{\psi_0(K)} \quad (2.12)$$

Now $q_s(K)$ quantifies the occurrence of s -fold symmetry in a body, whereas $\arg(q_s(K)) = \arg(\psi_s(K))$ gives the preferred directions of this symmetry.

³Created with Morphometer 19.04, Schaller (2019)

2.2 Threshold-dependent MF/MT

Since the MF/MT are not defined for grayscale images, but rather for sets that would be represented by binary images, a threshold is chosen. The body used for the calculation of the MF/MT is represented by all pixels above this threshold. Grayscale information lost otherwise is considered by an interpolation algorithm as described in Mantz et al. (2008), where pixel centers are moved slightly to smooth the contour according to the true pixel values.

The marching-squares algorithm used here is part of the papaya2-library (Kapfer et al., 2019). A 2x2 window is moved over the image and the desired Minkowski-tensor or -functional of this window is calculated. The area outside the window is assumed to be open (below threshold). In the case of binary images, the 16 possible configurations can be calculated beforehand. This is not possible in the case of grayscale images, but computation time is still reduced. To obtain the total values for a specific section of the image, the values obtained in the 2x2 windows are summed up, using the additivity property.

It is now possible to choose a range of thresholds and compute several MF/MT for each of them. This has been done for an example image in Fig. 2.3.

I tested this as a method to detect bubbles in the LMC. From the diffuse source catalog described in Davies et al. (1976), objects that look like bubbles and those that are not bubbles were manually selected and various threshold-dependent MF and MT were calculated. The plots were searched for obvious differences, but no useful result was achieved due to wild fluctuations of the MT for both images of bubbles and non-bubbles (as in Fig. 2.3). A longer list of bubbles and non-bubbles including H α -images and plots is shown in the appendix section C. No clear automatic separation on this basis was possible, so the approach was discarded.

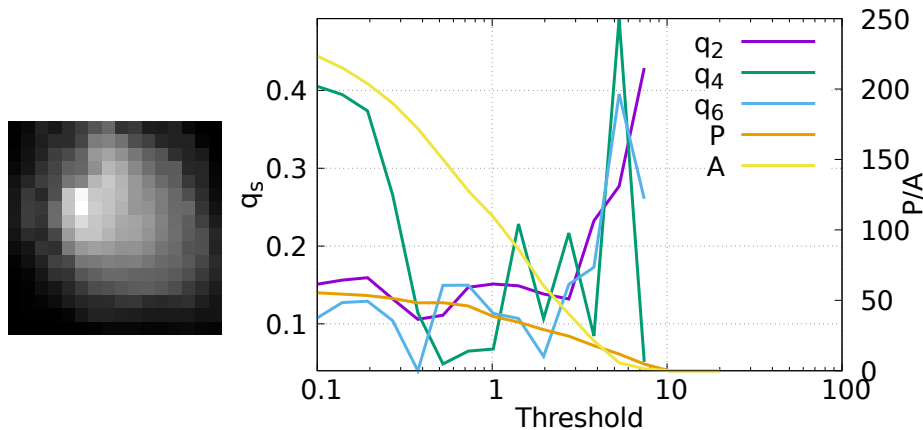


Figure 2.3: The bubble LHA 120-N20 (left) and values of q_2 , q_4 , q_6 , area and perimeter in pixel units for various intensity thresholds.

2.3 Minkowski map algorithm

Often the global MF and MT of an image do not provide the desired information and rather a more localized analysis is suitable. This is achieved by calculating so-called Minkowski maps.

After an image is analyzed with the marching 2x2 square, a localized map of MF/MT (a Minkowski map) at a scale of 2 pixels is obtained. To move to larger sizes the map can be smoothed using the MT's additivity property. Smoothing here means moving a window over the image, calculating some weighted average of the pixel values, and using these averages as the pixel values of a new image as it is done in classical image processing. If the image is a Minkowski map and the average is calculated linearly, the result is another Minkowski map. Like this, the 2-pixel map is turned into a map at scales proportional to the window size. I

chose a circular window with weights decaying linearly from the center. This emphasizes the center of the window while still taking regions further away into account. Comparing to maps where the weights were constant (directly summing up the values of the smaller scaled map in each window), the qualitative difference was small. Linearly decreasing weights proved to be sufficient for further work, but other weight functions were not tested.

The averaged values in each window were normalized by dividing by the square root of the window area. This cancels out the scale dependence of the ψ_s while keeping the phase, so that their absolute values at different window sizes could be compared. The size information is conserved as the window area is known for each map. All further mentions of ψ_s in Minkowski maps refer to this normalized version.

Since calculating the smoothed value at every position requires a lot of computation time while providing information at much larger distances, the window is moved in steps one sixth of its diameter. This gives an image consisting of larger tiles.

To use as much image information as possible several thresholds are used and the resulting complex maps averaged. The lowest threshold should be low enough to show the fainter sections of an image, but if it is too low the next higher threshold will correspond to essentially the same image, skewing the average. The highest threshold should be chosen such that brighter regions are allowed to stand out, but a too high threshold will lead to an image mostly equal to zero. The number of thresholds should be high enough that the contours of any relevant structure are captured. Experience showed that strongly increasing the number did not visibly alter the Minkowski maps. The chosen parameters for the LMC images used here are listed in table 2.1. The resulting Minkowski maps of $|\psi_2|$ for a window size of 150 pixels and all three original images are shown in Fig. 2.4. It can be seen that $|\psi_2|$ is sensitive to elongated structures (filaments).

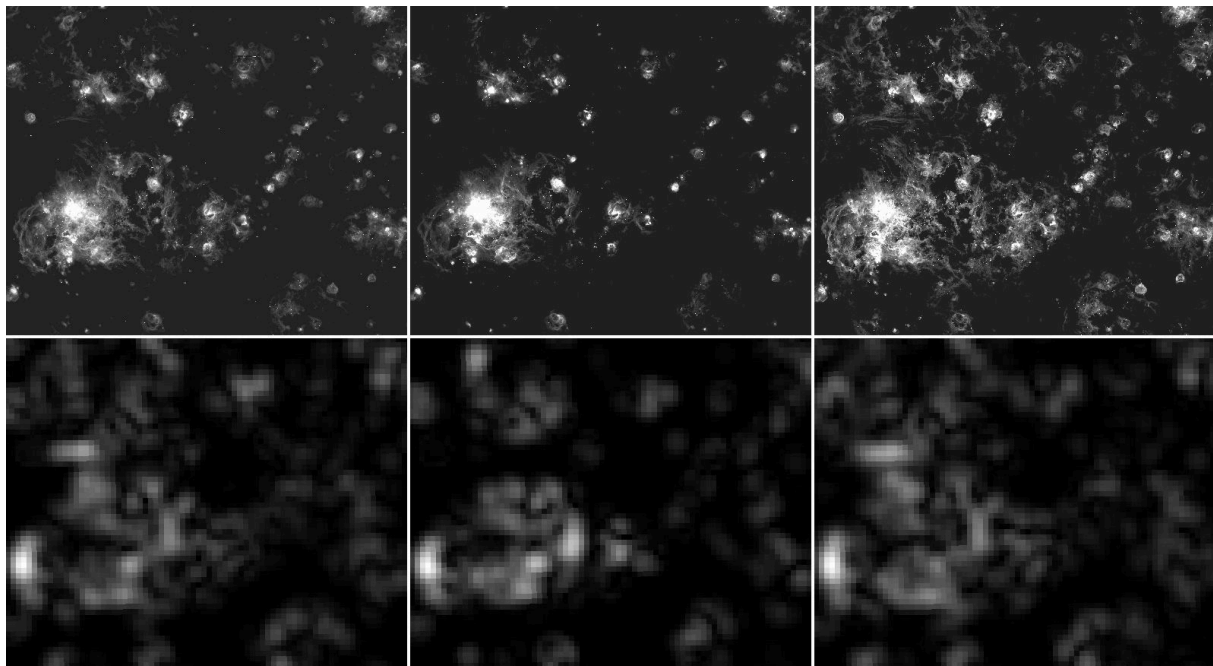


Figure 2.4: Original images (top) and Minkowski maps of $|\psi_2|$ (bottom) for a window size of 150 pixels. Left: $H\alpha$, middle: OIII, right: SII

Image	Min	Max	Nr.
H α	0.1	40	9
OIII	0.1	40	9
SII	0.045	40	10

Table 2.1: Threshold parameters for Minkowski map generation for the LMC images. Thresholds were logarithmically spaced and included the borders.

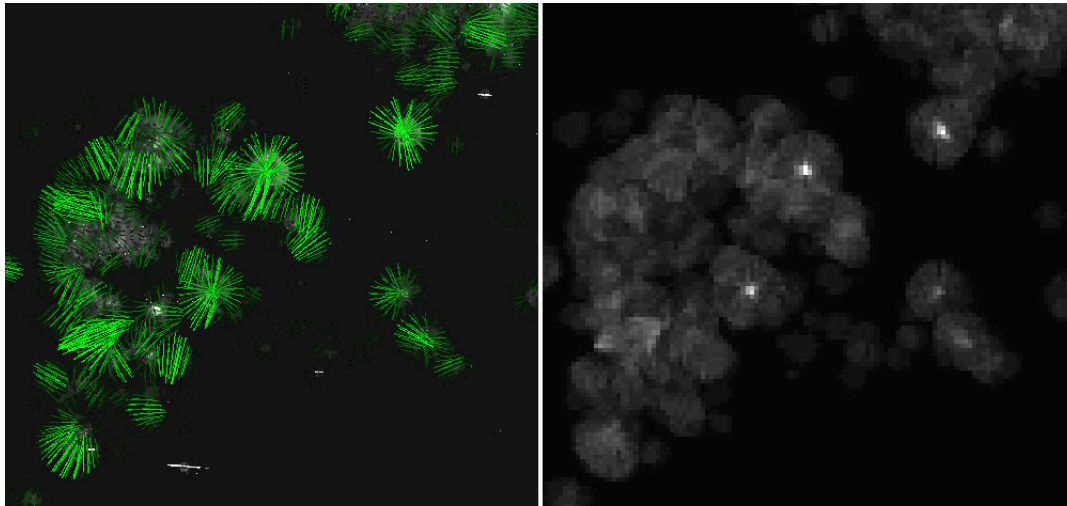


Figure 2.5: Left: Lines perpendicular to filaments for a window size of 40 px, determined via the phase of ψ_2 . Right: line density of left image

2.4 Bubble detection

2.4.1 Line density condition

Bubbles are assumed to have a circular border consisting of filaments and all filaments must have been driven by an energy source somewhere along a line perpendicular to it. For any filament of a bubble, this point is in the center where all lines meet. This may be used for automatic bubble detection via the absolute value and the phase of ψ_2 .

With the phase φ , the orientation of a given filament is measured and a line perpendicular to it is drawn. Since a phase shift of 2π only corresponds to a rotation of π , the angle of the line is given by $0.5 \cdot (\pm\pi - \varphi)$. The length l of the line is chosen proportional to the window size w and to $|\psi_2|/m$ where m is a free parameter: $l = w \cdot \frac{|\psi_2|}{m}$. This is illustrated on the left in Fig. 2.5. m can be treated as the value of $|\psi_2|$ at which the line is as long as the window diameter.

In the center of a bubble, the lines coming from its border should meet. This is seen as an increase in the number of lines per tile (the line density). The line density is obtained by checking which tiles are crossed by a line. The right panel of Fig. 2.5 shows the line density map corresponding to the lines in the left panel.

Thus for bubble detection, a threshold line density should be surpassed. When several neighbors are above the threshold, only the square with the highest value is chosen to avoid multiple detections of the same bubble. If two neighbors have the same value above the threshold, the one on top/to the right is chosen. The optimal threshold strongly depends on the image itself. Smaller substructures and noise lead to shorter lines and lower line densities.

2.4.2 Falling $|\psi_2|$ condition

Additionally, for a round bubble $|\psi_2|$ should decrease when going to a higher window size w' since contributions from different phases cancel out: $|\psi_{2,w}| > |\psi_{2,w'}|$ for $w \gg w'^4$. This can be seen in the example bubble shown in Fig. 2.6. The filaments strongly pronounced in the 40 px-map disappear in the 100 px-map. The rotation of the phase along the bubble is clearly visible.

In practice, an average of $|\psi_{2,w}|$ over a central square with size equal to $w/2$ was taken and $|\psi_{2,w'}|$ at the higher scaled map is allowed to be up to 0.05 higher than in the original map, since most bubbles are not perfectly spherical and thus have non-vanishing $\psi_{2,w'}$. This has shown to be a sufficient compromise between a high bubble acceptance in total numbers and low non-bubble detection fraction.

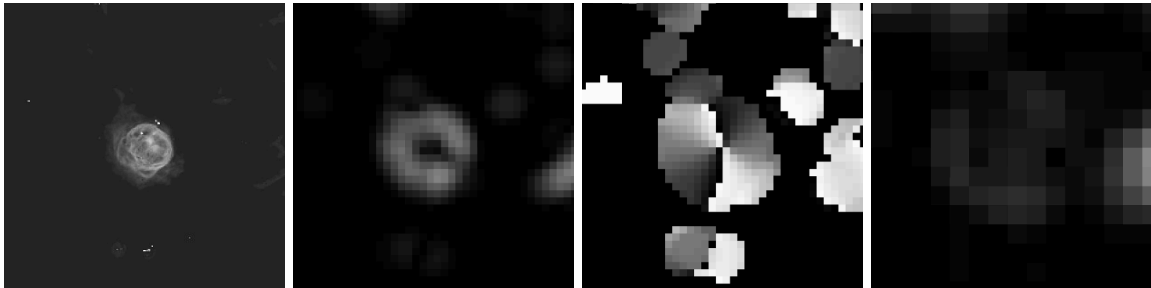


Figure 2.6: The region LHA 120-N 70 in H α (left) and the corresponding ψ_2 Minkowski maps for window size 40 px (absolute value: center left, phase: center right) and 100 px absolute value (right). In the right panel contributions from all sides of the bubble cancel each other out due to the phase rotation along the bubble.

Examples: Simple shapes

The detection methods are further demonstrated in Fig. 2.7. Here, circles and ellipses of varying boundary types are shown along with the corresponding $|\psi_2|$ Minkowski map at the window size of the circle diameter, the line density, and the Minkowski map at triple the previous window size. Detected bubbles are shown as squares around the circles. For this, the line density threshold was chosen low enough to contain the lowest local maximum at the center of a circle. The line density criterion thus includes all bubbles. The falling $|\psi_2|$ condition then accepts all of them since the Minkowski map for larger windows is generally darker.

The importance of the falling $|\psi_2|$ condition is demonstrated in Fig. 2.8, where several intersecting lines are shown. They lead to increased line density at a window size comparable to the space between the lines, but $|\psi_2|$ at the larger scaled map is higher as it reacts to the elongated nature of the lines. Even for low line density thresholds, no bubble is detected.

2.4.3 Parameter estimation

The algorithm described here has three free parameters: the above mentioned m determining the length of a line, the line density threshold, and the higher window size w' at which $|\psi_2|$ should not increase significantly. These need to be manually optimized. For the data used in this work, this was done by looking at changes when modifying one or two parameters and a change was accepted if significantly more bubbles than non-bubbles were added/more non-bubbles than bubbles were removed by the change. This was done for window diameters varying from 12 to 70 pixels. For lower sizes, the detection failed. The bubbles at such small sizes do not appear as round as necessary to produce meaningful line densities. Additionally, since the maps here consist of tiles of size $1/6$ of the window diameter, window sizes smaller than 12 are evaluated

⁴Note that this only holds because of the normalization of the ψ_s with the square root of the window area.

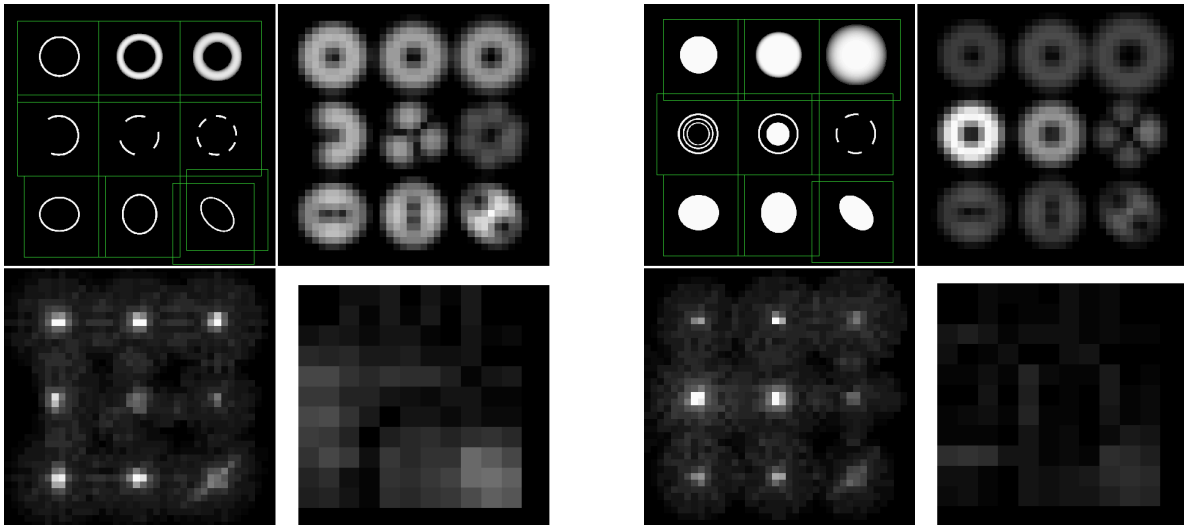


Figure 2.7: Both subfigures respectively: Several circles and ellipses with detected bubbles (top left), the $|\psi_2|$ Minkowski map at window size = circle diameter of top left circle (top right), the resulting line density (bottom left), and the the $|\psi_2|$ Minkowski map at window size = 3-circle diameter (bottom right, same scale as other Minkowski map). All circles are recognized as bubbles due to high line density and falling $|\psi_2|$.

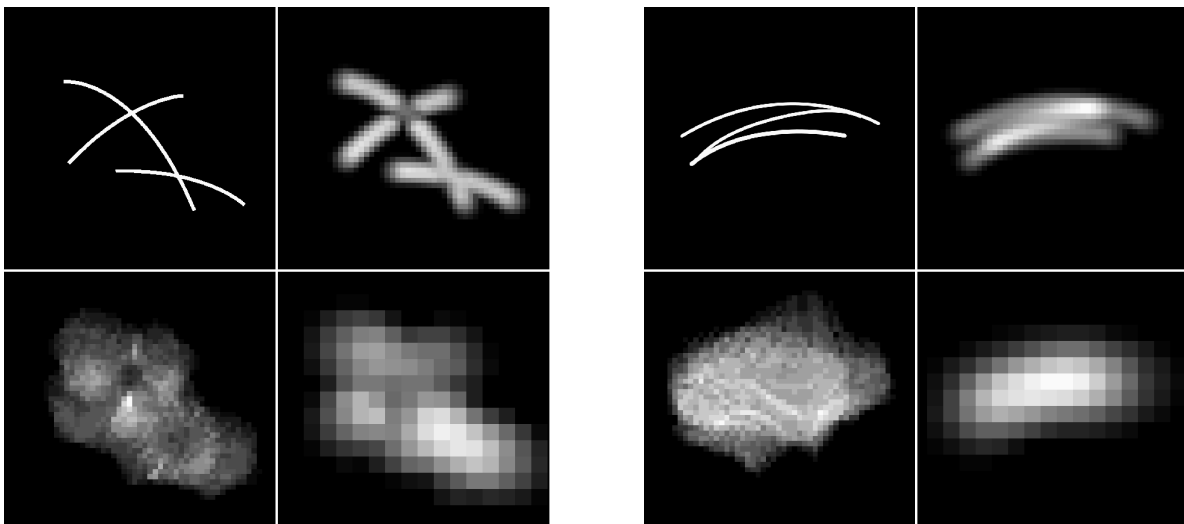


Figure 2.8: Both subfigures respectively: Several intersecting (top left), the $|\psi_2|$ Minkowski map at window size large enough for an increased line density (top right), the resulting line density (bottom left), and the the $|\psi_2|$ Minkowski map at triple window size (bottom right, same scale as other Minkowski map). In spite of setting a low line density threshold, no part of the image is detected as a bubble due to the falling $|\psi_2|$ condition not being fulfilled.

diameter [px]	m	threshold	compare size [px]
12	0.25	23	40
15	0.25	24	50
20	0.25	20	60
30	0.3	16	100
40	0.3	17	100
50	0.3	16	150
60	0.3	17	200
70	0.3	24	250

diameter [px]	m	threshold	compare size [px]
12	0.25	21	40
15	0.25	22	50
20	0.25	18	60
30	0.3	14	100
40	0.3	15	100
50	0.3	14	150
60	0.3	15	200
70	0.3	20	250

Table 2.2: Manually determined bubble detection parameters in LMC H α /OIII (top) /SII (bottom) image. 10 px correspond to about 1.67' or 24 pc at a distance of 50 kpc.

at every pixel, which strongly raises computation time.

Generally, m should be in the range of “typical” $|\psi_2|$ values of filaments which is usually 0.2–0.5 depending on the image. If m is too high, the lines from a bubble’s edge cannot meet in its center and if it is too low, random structures that are not bubbles can also reach high line densities. The line density threshold strongly depends on the image. A starting value can either be manually determined by regarding a few obvious bubbles or guessed in the range of 10 to 20 and then adapted. Optimizing the line density threshold is more straightforward than optimizing m . If a lot of false positives are detected, it should be raised and if too few objects are found in general, it should be lowered. The optimal larger window size w' to check for falling $|\psi_2|$ always turned out close to $3w$. Nearby unrelated filaments with high $|\psi_2|$ should not influence the detection too much, which is why here a stagnation or slight rise was still accepted, but the bubble itself should cancel out.

The resulting parameters for the LMC H α , SII, and OIII images are listed in table 2.2. In OIII the same parameters as in H α could be used. In SII however, the line density threshold had to be lowered. This seems to be due to more extended structures being visible in the SII data, blurring out single filaments. It was tested whether raising the lowest threshold of the Minkowski maps to 0.1 (the lowest threshold of the H α and OIII maps as stated in section 2.3) improved the detection, but instead less bubbles were found. An image showing the detected bubbles in H α is given in Fig. 2.9, SII bubbles are in Fig. 2.10, and OII bubbles in Fig. 2.11.

2.4.4 Preparation for statistical analysis

For further statistical analysis, a point pattern of bubbles is desired. To combine all bubbles detected at different sizes to one list, it is necessary to estimate which objects seen at different sizes stem from the same physical object. In the images in this section detected bubbles are marked by squares with size $2w$. They shall be referred to as the squares or boxes of the bubbles. It shall be assumed that all boxes of the same or similar size come from the same object if they have a large overlap. However, if a small bubble is part of a larger bubble and no intermediate

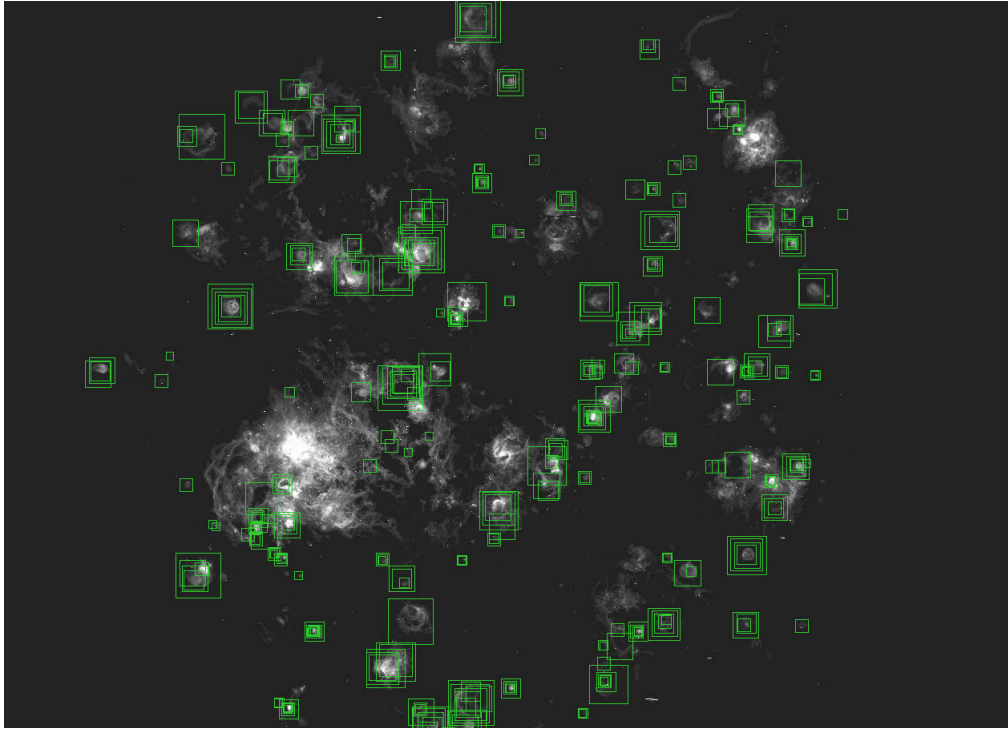


Figure 2.9: Bubbles detected in the $H\alpha$ image at window sizes ranging from 12 to 70 pixels with square-size twice the window diameter.

sized one is detected, they should be treated as different objects due to their largely different size.

This is achieved the following way: First, all bubbles of the smallest size are compared and if the center of one bubble is inside the square of the other, both are assumed to be originating from the same object and merged into a list. Then it is checked whether the center of a bubble detected at a size one step higher is contained within the square of a smaller bubble. If this is the case, it is combined with the smaller one(s) and the step is repeated for the next higher size. In the end, for each physical bubble that was detected a list of corresponding squares is returned.

To turn these lists into a point pattern, the average of the centers of the squares is calculated. This gives an average bubble position at different window sizes and can be used as a point pattern. The result for the $H\alpha$ -bubbles is shown in Fig. 2.12. A list of all combined bubbles is available in the appendix for $H\alpha$ in table A.2, for SII in table A.1, and for OIII in table A.3.

While some bubbles still have several boxes which do not simply refer to different parts, most of the boxes stemming from the same object are now combined. The image is much less cluttered than Fig. 2.9. The bubble-point patterns are analyzed using point process statistics in chapter 3.

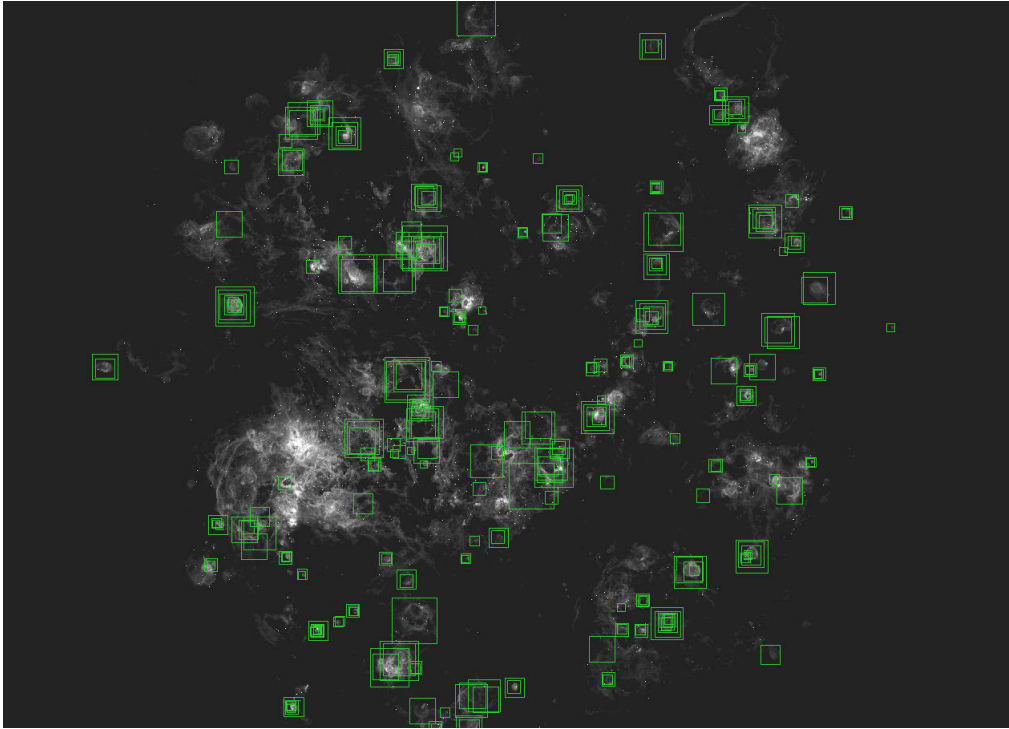


Figure 2.10: Bubbles detected in the SII image at window sizes ranging from 12 to 70 pixels with square-size twice the window diameter.

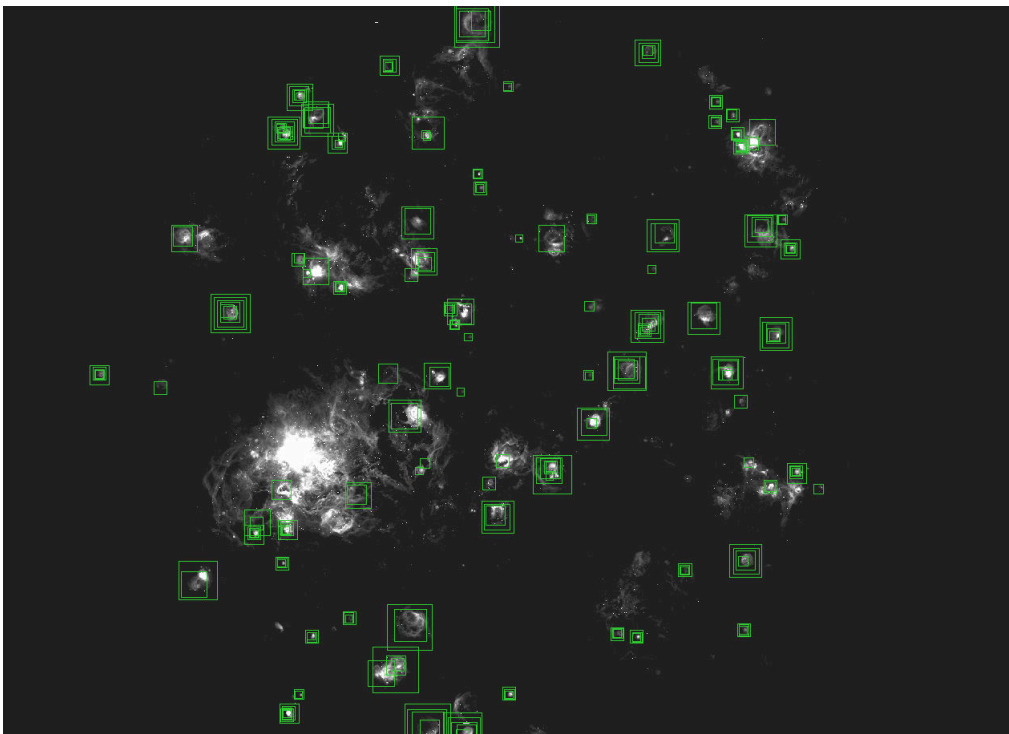


Figure 2.11: Bubbles detected in the OIII image at window sizes ranging from 12 to 70 pixels with square-size twice the window diameter.

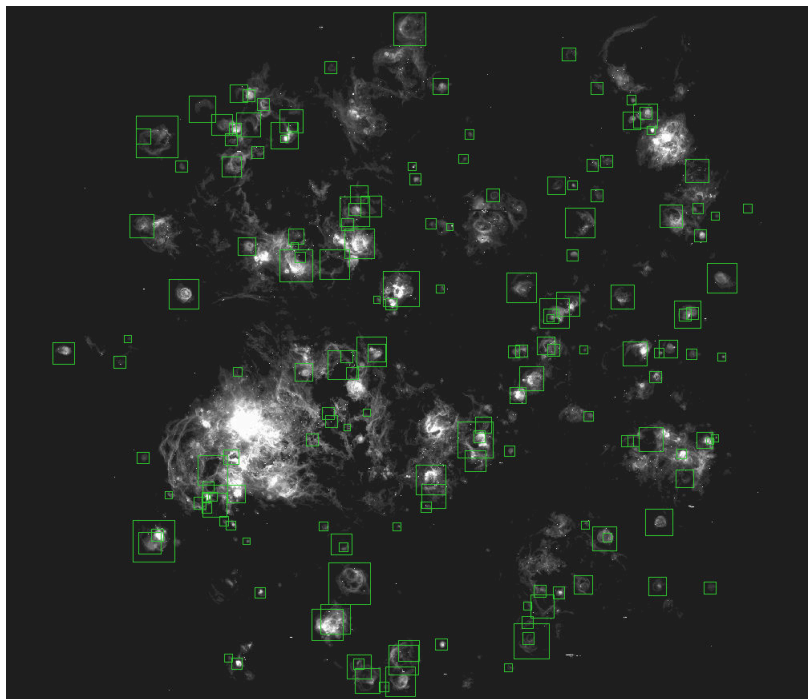


Figure 2.12: Bubbles detected in the $H\alpha$ image at window sizes ranging from 12 to 70 pixels combined. Bubble centers and sizes are averages from original boxes in Fig. 2.9.

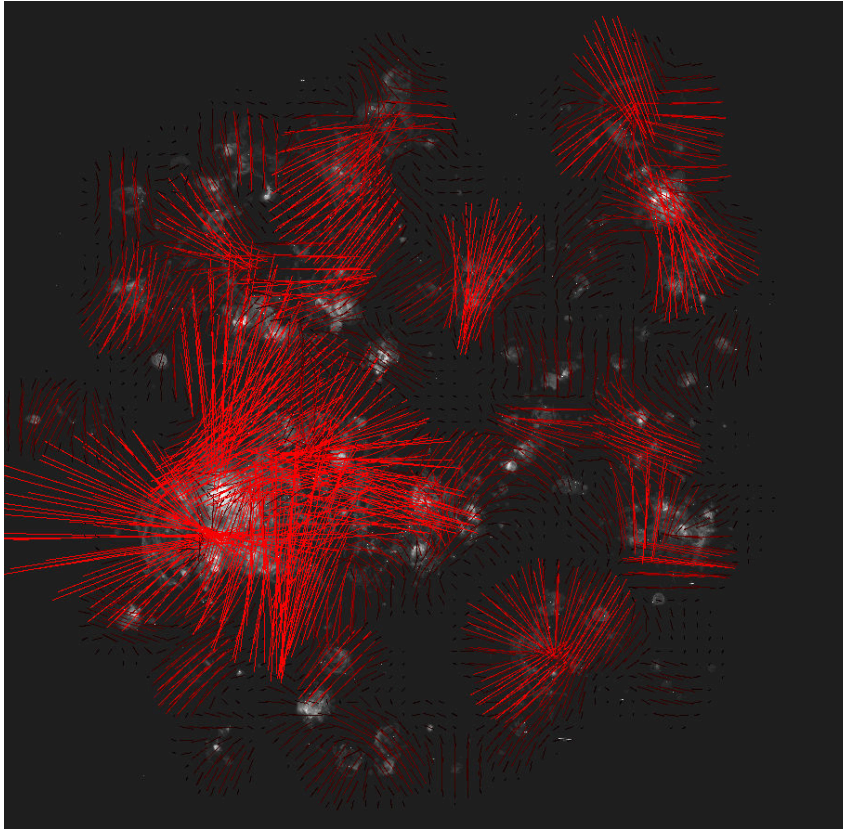


Figure 2.13: Lines in the $H\alpha$ image at window size 250 px, $m = 0.4$.

2.5 Large-scale structure

The bubbles detected in the previous section represent smaller structures in the LMC. The line and line density maps may also be used to analyze larger structures when increasing the window size. This is shown in Figures 2.13, 2.14, and 2.15 for $H\alpha$, SII, and OIII, respectively, at window size 250 px.

Strong lines originate from clear filaments, regardless of their brightness. There are several regions where many lines meet; they partially coincide with the LMC supergiant shells. Especially the filamentary region east and southeast of 30 Dor causes long intersecting lines meeting at the supergiant shell LMC SGS 2. This relation of line densities and shells is further discussed in section 3.3.1.

Comparing the different wavelengths, $H\alpha$ and SII look similar in general. The SII image contains many faint filaments that slightly affect the line maps. In OIII however, the lines follow the smaller extension of the OIII emission.

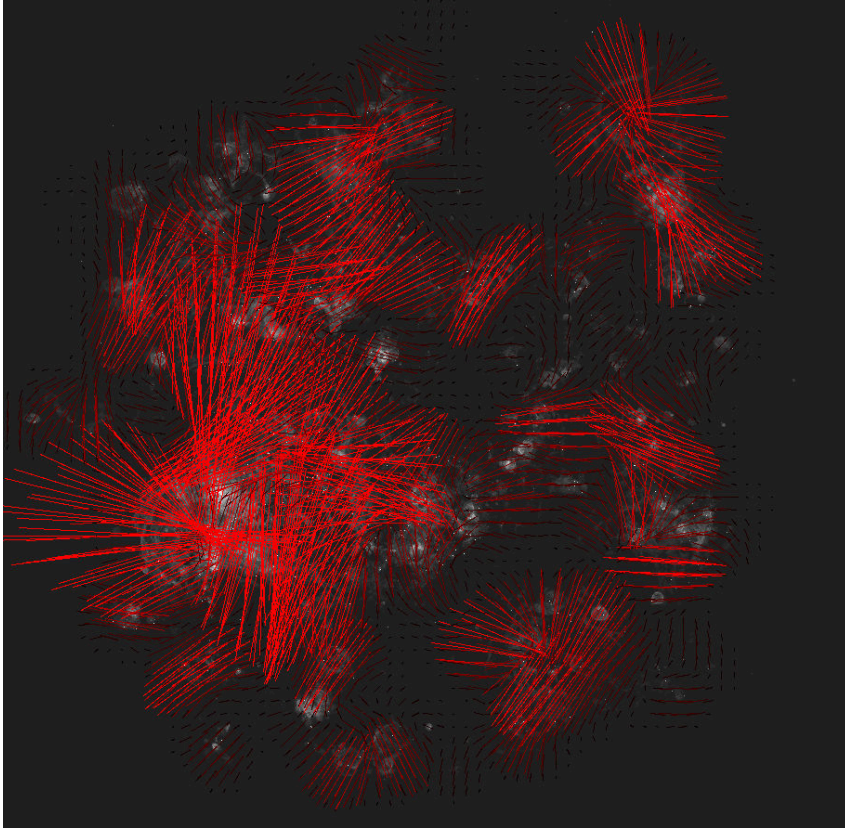


Figure 2.14: Lines in the SII image at window size 250 px, $m = 0.4$.

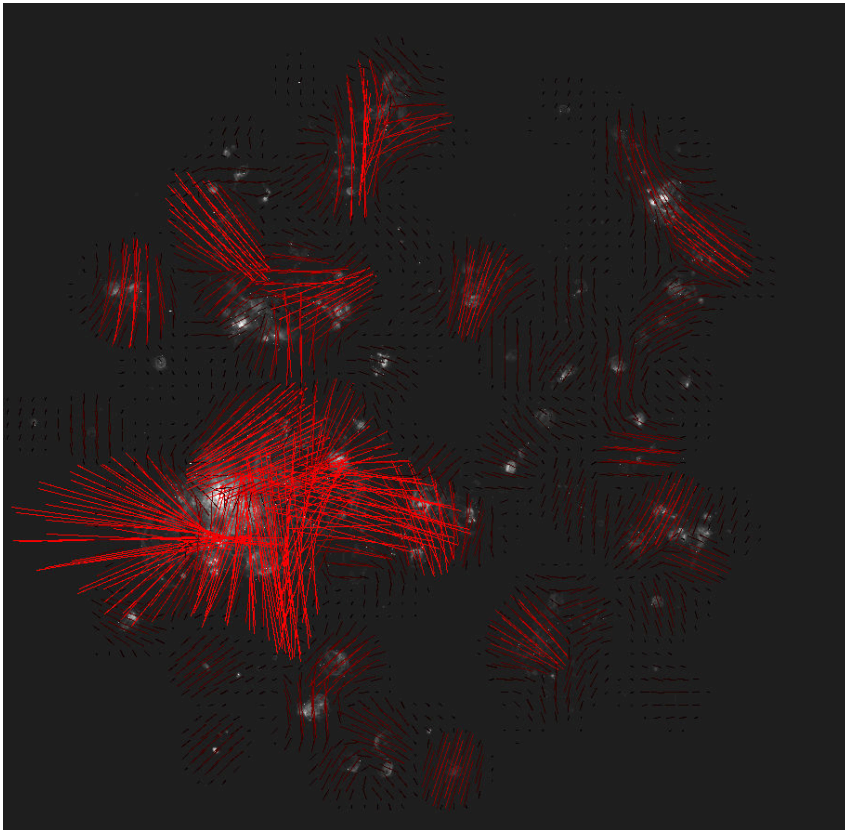


Figure 2.15: Lines in the OIII image at window size 250 px, $m = 0.4$.

2.6 SMC bubble detection

Optimizing the bubble detection in the LMC requires manually adjusting six free parameters. Additionally, the images contain very little noise which was useful for developing methods but is often not the case for other data. To check the universality and noise response of the bubble detection, the noisier SMC data were used; the SII data containing stronger noise than OIII and H α .

The initial images needed to be binned and smoothed. For a quick test, the images were opened⁵ with a window diameter of five (H α , OIII) or three (SII) and the resulting images were binned by a factor of three in each axis. Opening with a diameter of three pixels thus does not introduce noticeable blur in the binned images while removing bright stars.

Minkowski map generation parameters were visually estimated to the settings in table 2.3. No extensive optimization of the bubble detection was performed in order to find out how easily the algorithm could be used. All bubbles detected in this section are listed in the appendix section A.2. The SMC in H α with all bubbles found is shown in Fig. 2.16. Even with this simple approach, a large number of objects is detected.

				diameter	m	threshold	threshold	compare
				[px]		(H α , OIII)	(SII)	size [px]
				12	0.25	10	10	40
				15	0.25	10	10	50
				20	0.25	12	10	60
Image	Min	Max	Nr.	30	0.3	10	10	100
H α , OIII	6	2500	12	40	0.3	10	12	100
SII	3	1300	12	50	0.3	10	12	150
				60	0.3	10	12	200
				70	0.3	12	12	250

Table 2.3: Left: Initial Minkowski map threshold parameters. Thresholds were logarithmically spaced and included the boundaries. Right: Non-optimized bubble detection parameters. 10 px correspond to about 1.67' or 24 pc at a distance of 50 kpc.

The results are comparable to the LMC data: single structures are easily detected, but bubbles surrounded by complex structures often are not. Surprisingly, a lot of bubbles in the south-west that are embedded in a more chaotic region are marked. These are, however, only part of the actual amount of bubbles. Further inspection reveals that in darker regions noise may impair bubble detection as nothing is detected e.g. in a large part northwest of the bar. An example of a bubble where noise possibly disturbs bubble detection by decreasing the absolute value of ψ_2 at its edges is shown in Fig. 2.17. This might also explain the low number of medium-sized (30-60 px) bubbles. It is possible that optimizing the detection parameters could decrease the effects of noise.

OIII bubbles are shown in Fig. 2.19. Despite the less extended emission, many bubbles were found, especially in the south-west and some larger bubbles that were not detected in H α . The lower extension might be advantageous as the bubbles stand out more. Additionally, the noise in this image is weaker.

The SII results are shown in Fig. 2.18. Noise is more important than before and leads to a few false detections. Now most bubbles are detected in regions with either intrinsically lower noise or in brighter regions with a better signal-to-noise ratio.

⁵Opening is an image smoothing technique consisting of first eroding (setting a pixel value to the lowest of its neighbors in a neighborhood) and then dilating (setting a pixel value to the highest of its neighbors). It removes small brighter regions.

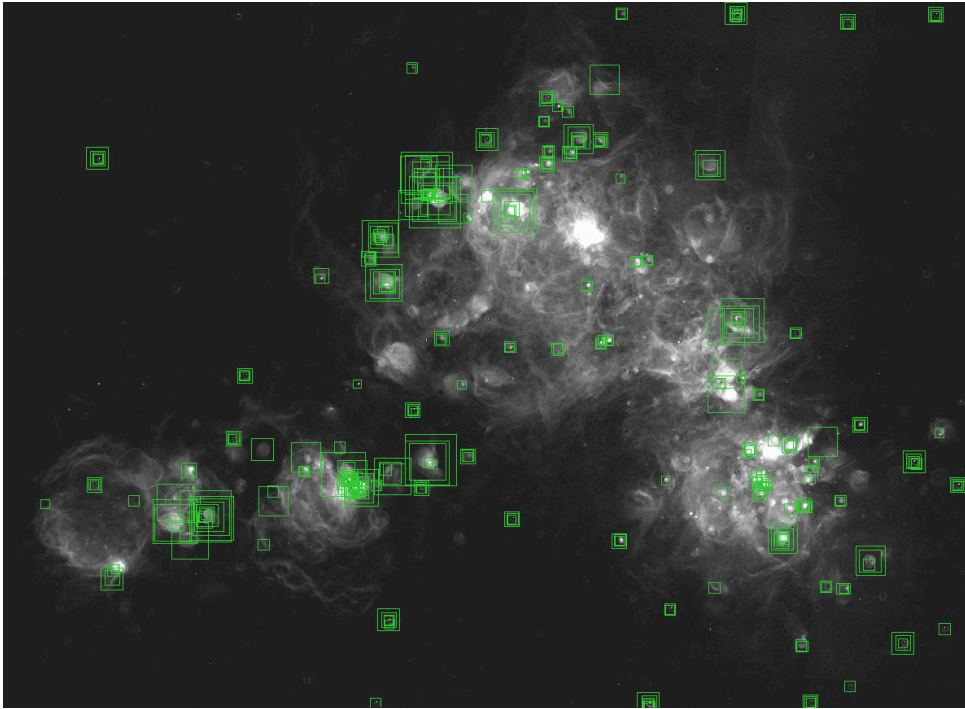


Figure 2.16: Bubbles detected in the SMC $H\alpha$ image at window sizes ranging from 12 to 70 pixels with square-size twice the window diameter. Parameters were not optimized. All bubbles are listed in the appendix Tab. A.4.

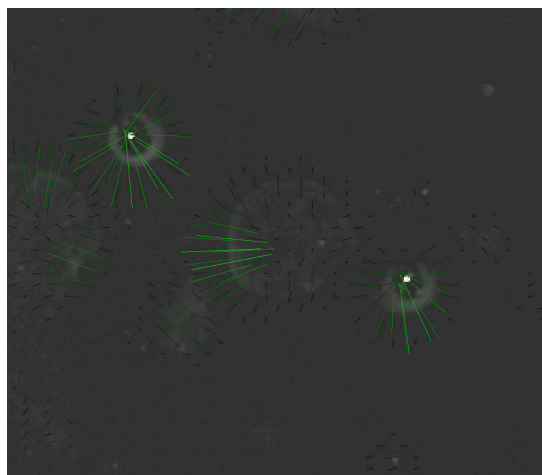


Figure 2.17: Lines around a bubble at window size 30 in the SMC $H\alpha$ image. In areas where the edge of the bubble is dominated by noise, the absolute value of ψ_2 is decreased.

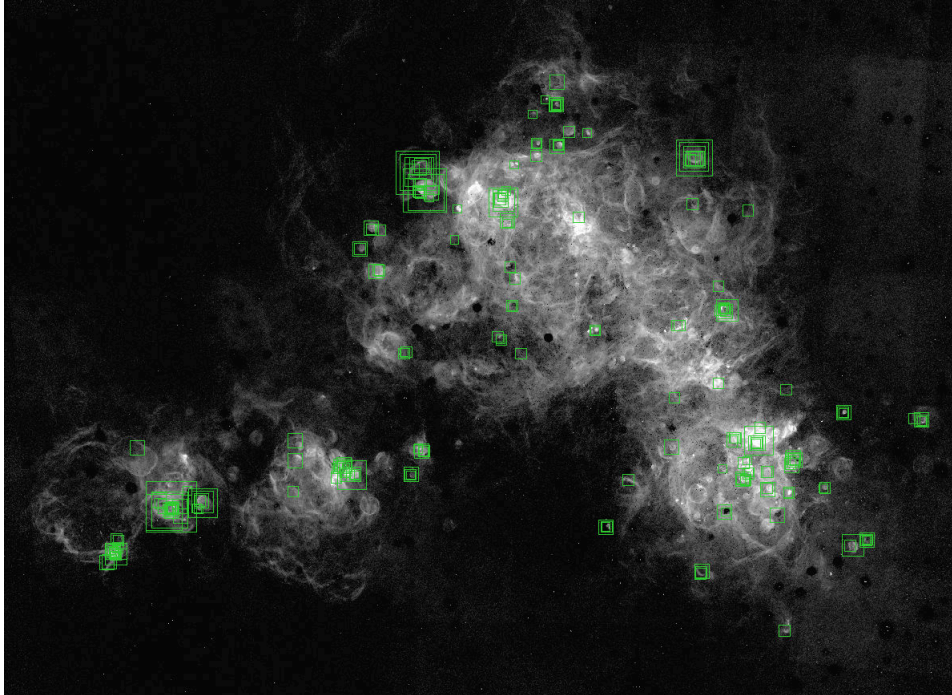


Figure 2.18: Bubbles detected in the SMC SII image at window sizes ranging from 12 to 70 pixels with square-size twice the window diameter. Parameters were not optimized. All bubbles are listed in the appendix Tab. A.7.

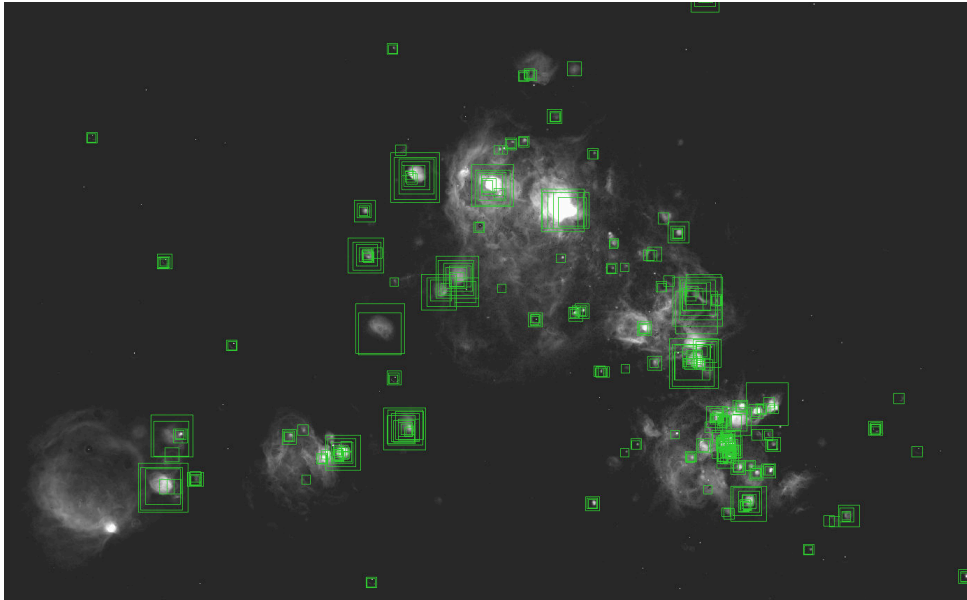


Figure 2.19: Bubbles detected in the SMC OIII image at window sizes ranging from 12 to 70 pixels with square-size twice the window diameter. Parameters were not optimized. All bubbles are listed in the appendix Tab. A.9.

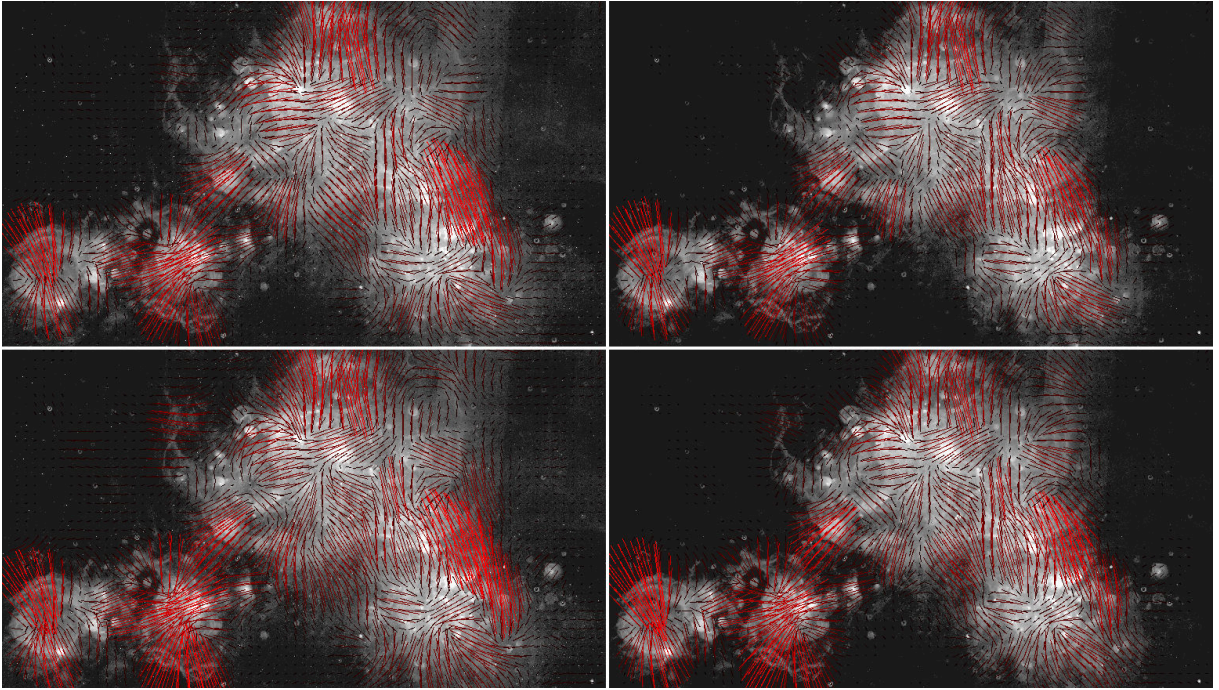


Figure 2.20: Lines at window size 250, $m = 0.4$, on SMC $H\alpha$ -data. Top: 12 thresholds between 6 and 2500, bottom: 12 thresholds between 3 and 1300 used for Minkowski map generation. Left: original image opened with diameter 3 px (more noise), right: opening diameter 5 px (less noise).

2.6.1 Noise dependence of ψ_2 and bubbles

The previous results showed that image noise affects the detection of bubbles. The lower Minkowski map generation threshold is also strongly affected by the treatment of noise: Should it be chosen higher than most noise, but cutting off fainter structures, or should the noise be part of the Minkowski map? To test the influence of the initial opening and the lower threshold, lines at different window sizes were calculated for opening with diameter three and five, and the two threshold settings used above.

A comparison of these settings is shown in Fig. 2.20 ($H\alpha$), Fig. 2.21 (SII), and Fig. 2.22 (OIII). Whereas no large difference is apparent in $H\alpha$, in SII $|\psi_2|$ seems to be lower for the more strongly denoised images and higher thresholds. Large parts of the SMC create nearly horizontal lines in SII, although most filaments seem similar to $H\alpha$. The angle of the lines persists when further raising the lower Minkowski map thresholds to exclude more noise. This makes a systematic effect of the mosaic nature of the images unlikely. The few horizontal filaments might be more disturbed by the noise and not clear enough to significantly change the angle of the lines. Additionally, some regions that cause vertical lines in the north in $H\alpha$ are not present in SII. In general, these lines are shorter than their LMC counterparts despite similar thresholds. The anisotropy of the SMC at this scale is weaker.

In OIII, the region in the center of the images changes the most for the different settings: $|\psi_2|$ is strongest for low thresholds and more noise and with larger opening diameters and higher thresholds, the structure apparently partially falls below the lowest threshold.

The lines at window size 40 were compared the same way, shown in Fig. 2.23 ($H\alpha$), Fig. 2.24 (SII), and Fig. 2.25 (OIII). Only a portion of the whole image is shown to keep single lines distinguishable. Here, the apparent differences are smaller in general. The most distinct features appear in all settings in similar magnitude, but in the more chaotic region in the northwest of the images, the pattern varies more.

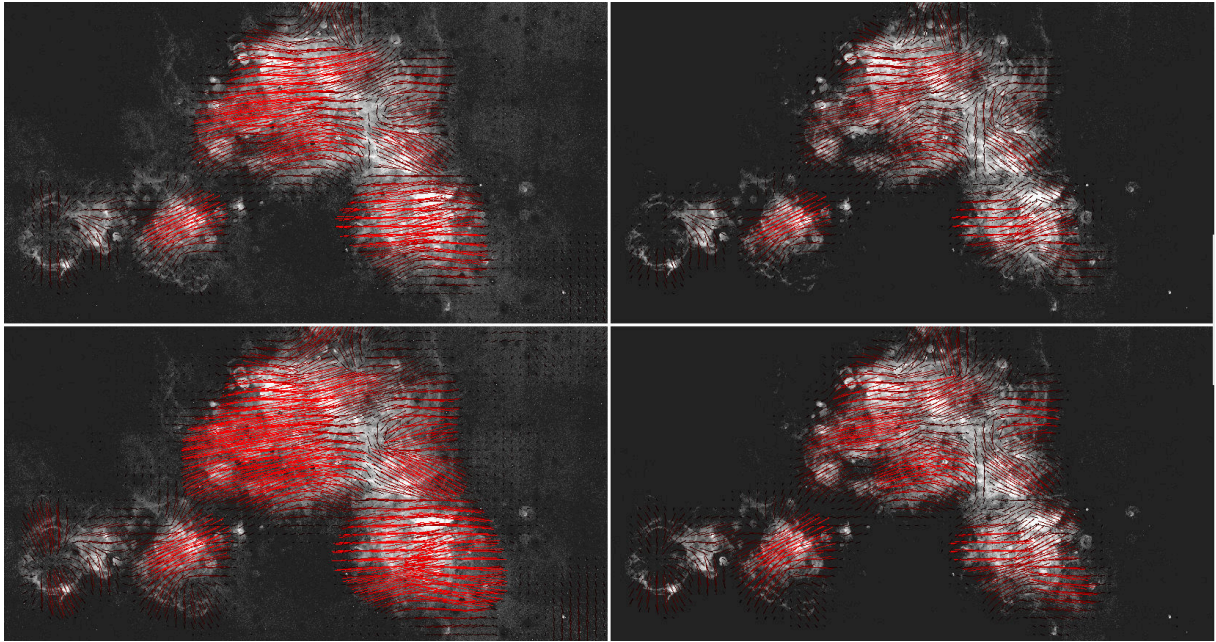


Figure 2.21: Lines at window size 250, $m = 0.4$, on SMC SII-data. Top: 12 thresholds between 6 and 2500, bottom: 12 thresholds between 3 and 1300 used for Minkowski map generation. Left: original image opened with diameter 3 px (more noise), right: opening diameter 5 px (less noise).

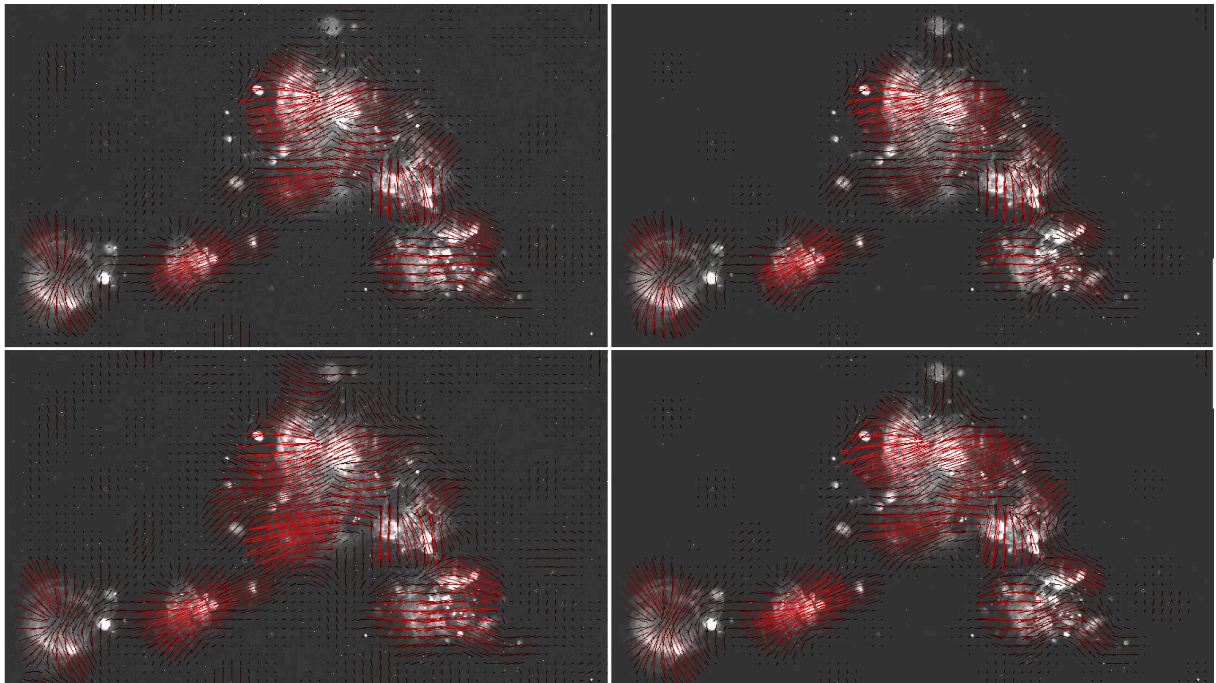


Figure 2.22: Lines at window size 250, $m = 0.4$, on SMC OIII-data. Top: 12 thresholds between 6 and 2500, bottom: 12 thresholds between 3 and 1300 used for Minkowski map generation. Left: original image opened with diameter 3 px (more noise), right: opening diameter 5 px (less noise).

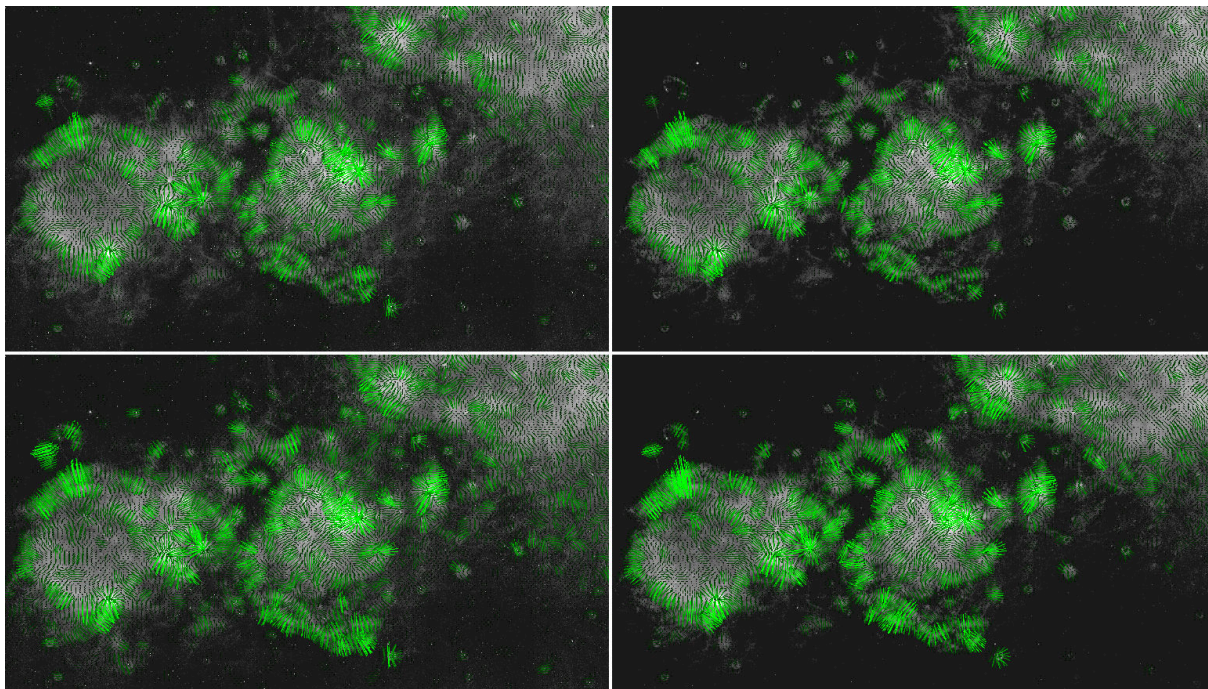


Figure 2.23: Lines at window size 40, $m = 0.3$, on SMC $H\alpha$ -data. Top: 12 thresholds between 6 and 2500, bottom: 12 thresholds between 3 and 1300 used for Minkowski map generation. Left: original image opened with diameter 3 px (more noise), right: opening diameter 5 px (less noise).

The variation still has an impact on bubble detection. Figure 2.26 shows the bubbles detected in $H\alpha$ at window size 40 px. The different settings lead to a comparable amount of bubbles, but partially different objects are detected. In the high Minkowski-map threshold images (top row), regions at the noisier borders are avoided.

The situation is similar in SII (Fig. 2.27). Overall, fewer bubbles are detected due to noise and the number of detected non-bubbles is high.

In OIII, noise is a smaller problem in general and for all settings tested here, a large amount of bubbles is found (Fig. 2.28). It appears that the initial image was denoised too much (right column) and in the noisier images on the left, more objects were found.

To check for possible improvements, the $H\alpha$ -detection was repeated for lower thresholds and more noise (bottom left images), the SII detection with less noise (bottom right images), and the OIII detection with more noise (top left images).

The bubbles detected with the new settings in $H\alpha$ are shown in Fig. 2.29. The number of detections rose from 153 to 287 after combining, most of them smaller bubbles. Part of this high number results from falsely not combining squares of the same object and there are some errors, but in general, the quality of the detections is good. Still, many bubbles visible to the bare eye are not marked. This shows room for further manual improvement. Apparently, bubbles at larger window sizes suffered under the increased noise: There were no detections at window sizes 50 and 60 px. Bubbles of this size should be detected at the edge of the brighter regions here, where noise has the largest effect.

The detection of bubbles with less noise in SII is shown in Fig. 2.30. The line density threshold had to be raised to 12 for all window sizes except 30 since the number of non-bubbles among the detections was very high otherwise. Additionally, the number of detected objects decreased from 100 to 61. This shows that keeping finer structures in the data is more important than denoising in these images. Single small noise maxima are canceled out in the Minkowski maps when going to larger window sizes, whereas opening can join them to larger structures that disturb the detection.

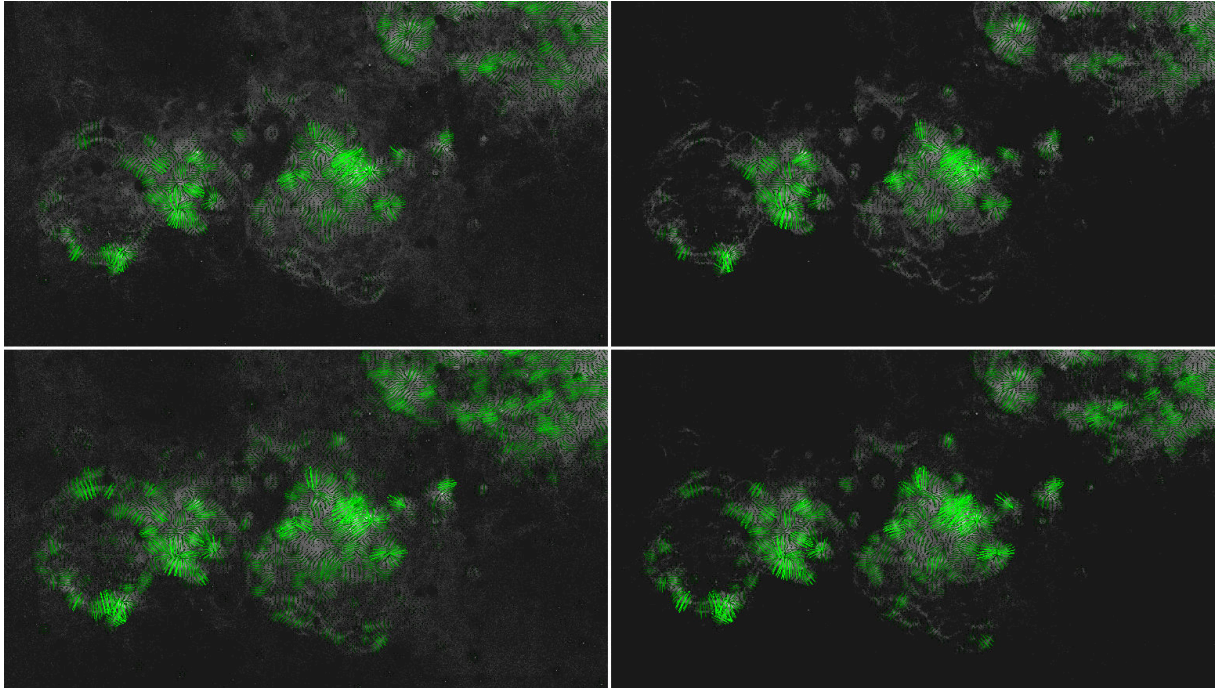


Figure 2.24: Lines at window size 40, $m = 0.3$, on SMC SII-data. Top: 12 thresholds between 6 and 2500, bottom: 12 thresholds between 3 and 1300 used for Minkowski map generation. Left: original image opened with diameter 3 px (more noise), right: opening diameter 5 px (less noise).

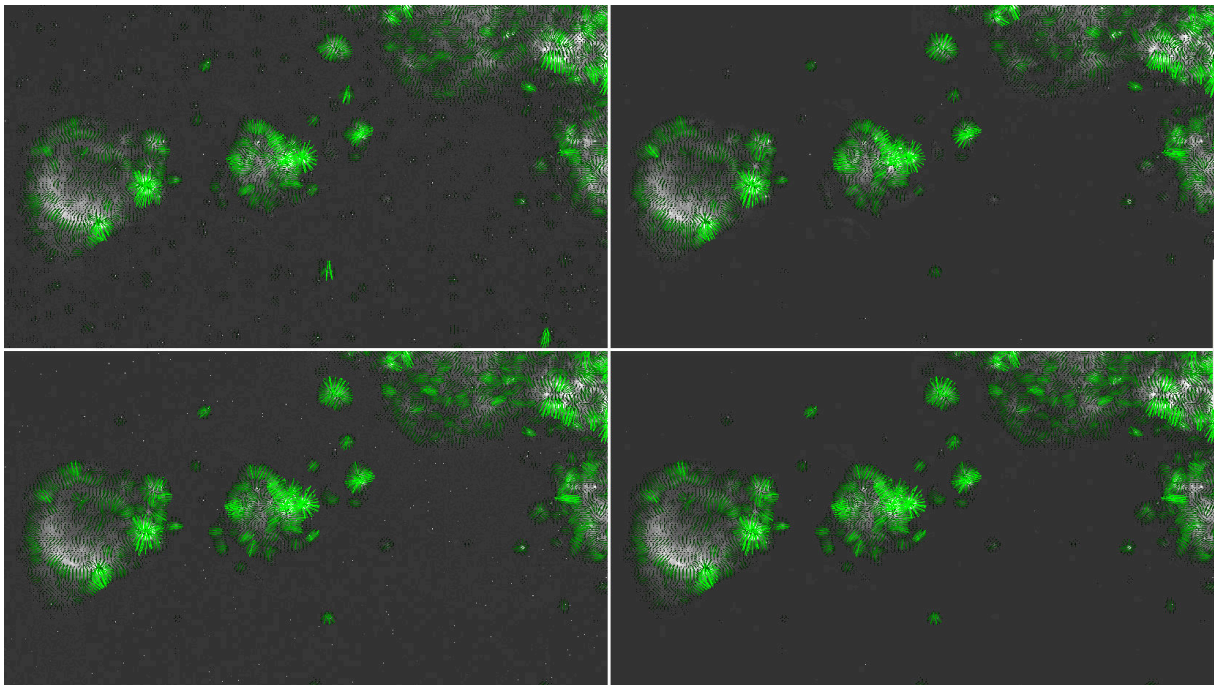


Figure 2.25: Lines at window size 40, $m = 0.3$, on SMC OIII-data. Top: 12 thresholds between 6 and 2500, bottom: 12 thresholds between 3 and 1300 used for Minkowski map generation. Left: original image opened with diameter 3 px (more noise), right: opening diameter 5 px (less noise).

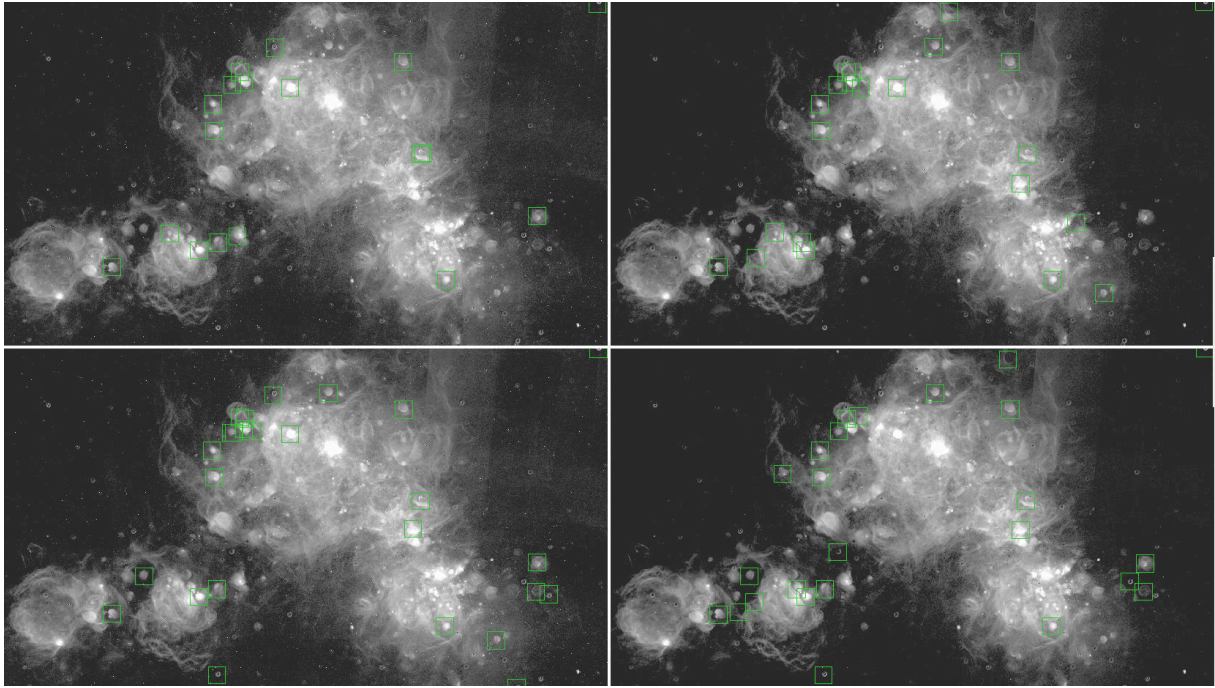


Figure 2.26: Bubbles detected at window size 40, $m = 0.3$, line density threshold 10, in SMC $H\alpha$ -data. Top: 12 thresholds between 6 and 2500, bottom: 12 thresholds between 3 and 1300 used for Minkowski map generation. Left: original image opened with diameter 3 px (more noise), right: opening diameter 5 px (less noise). Noise and the thresholds strongly influence bubble detection.

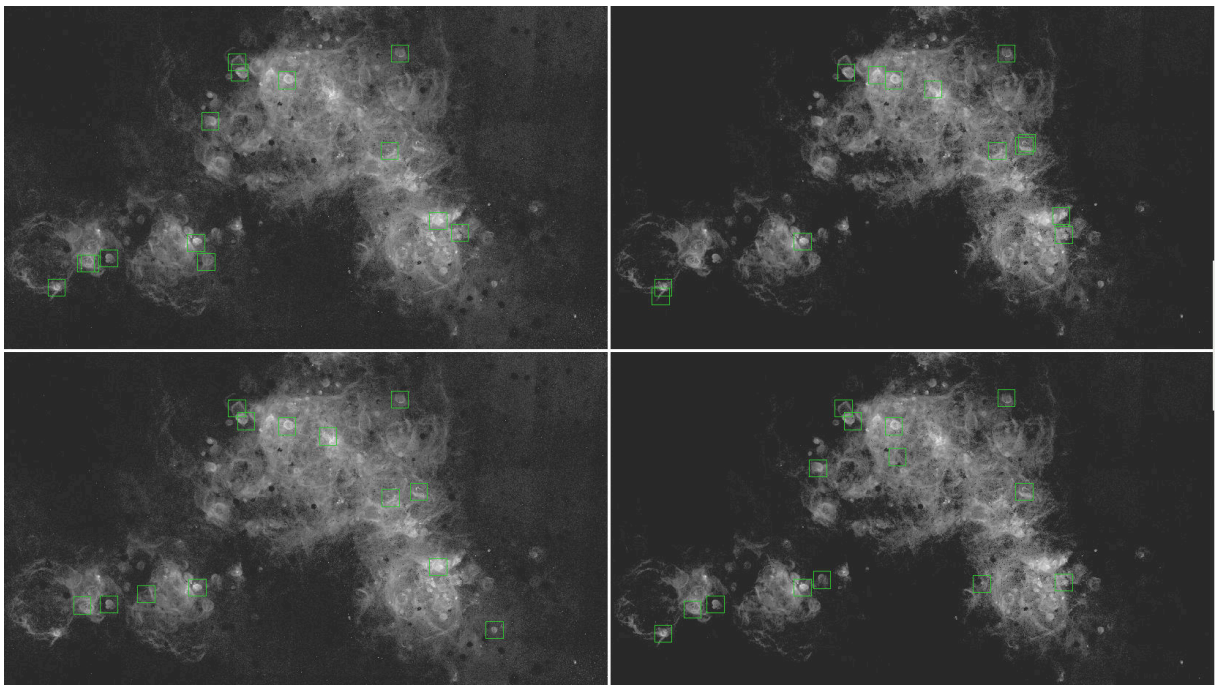


Figure 2.27: Bubbles detected at window size 40, $m = 0.3$, line density threshold 10, in SMC SII-data. Top: 12 thresholds between 6 and 2500, bottom: 12 thresholds between 3 and 1300 used for Minkowski map generation. Left: original image opened with diameter 3 px (more noise), right: opening diameter 5 px (less noise). Noise and the thresholds strongly influence bubble detection.

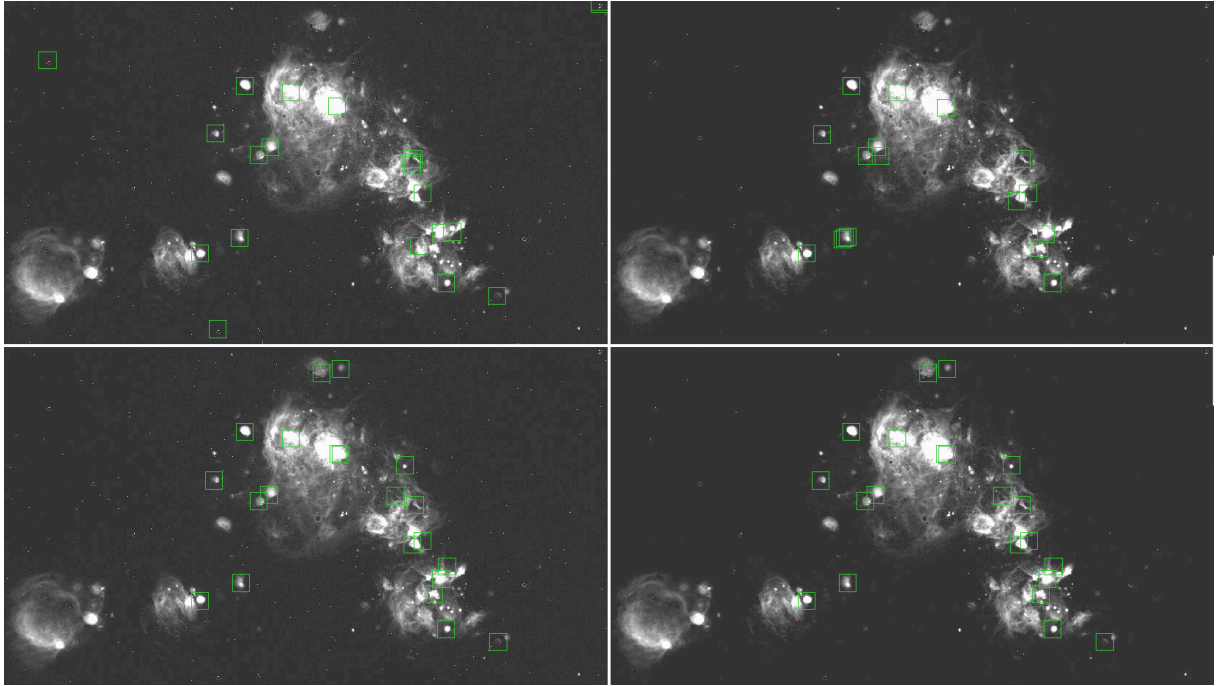


Figure 2.28: Bubbles detected at window size 40, $m = 0.3$, line density threshold 10, in SMC OIII-data. Top: 12 thresholds between 6 and 2500, bottom: 12 thresholds between 3 and 1300 used for Minkowski map generation. Left: original image opened with diameter 3 px (more noise), right: opening diameter 5 px (less noise). Noise and the thresholds strongly influence bubble detection.

In OIII, the detection changed less than for the others and the number of detections rose from 131 to 146 (Fig. 2.31). Noise plays a smaller role in general compared to SII and $H\alpha$, so denoising makes a smaller difference.

The conclusions are the following: it is possible to detect an acceptable amount of bubbles by quickly adjusting the detection parameters, mainly the line density threshold. Minkowski map generation thresholds should be chosen rather low so that they include parts of the noise. The noise itself should not be smoothed out too much, especially if the data is intrinsically noisier.

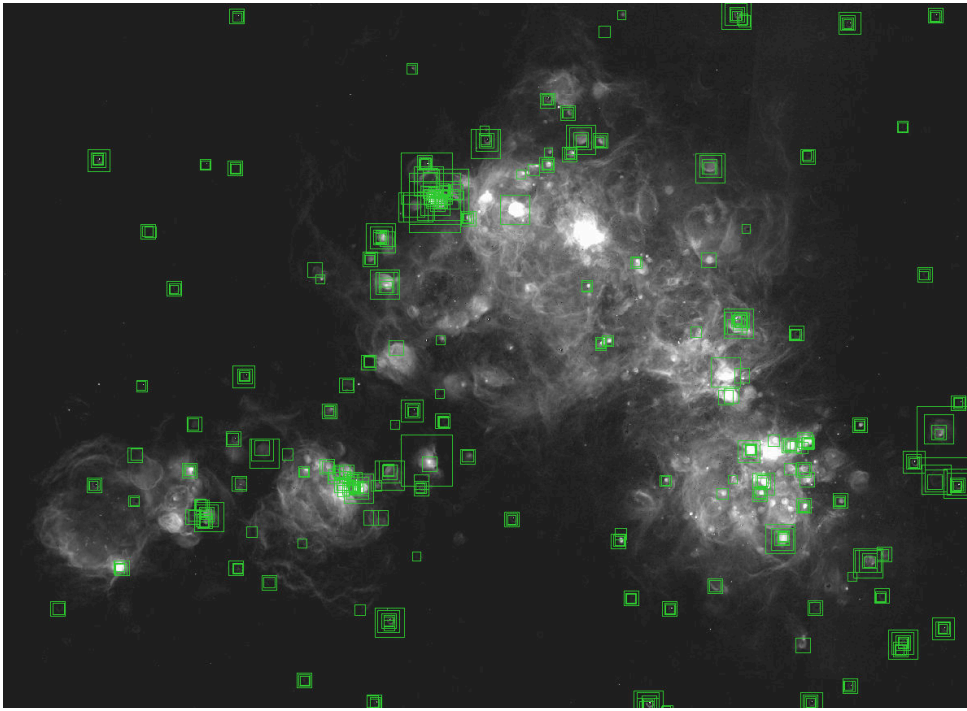


Figure 2.29: Bubbles detected in the SMC H α image at window sizes ranging from 12 to 70 pixels with square-size twice the window diameter. Minkowski map generation thresholds were lowered and more noise left in the image compared to Fig. 2.16. Corresponds to settings in bottom left image in Fig. 2.23. All bubbles are listed in the appendix Tab. A.5 & A.6.

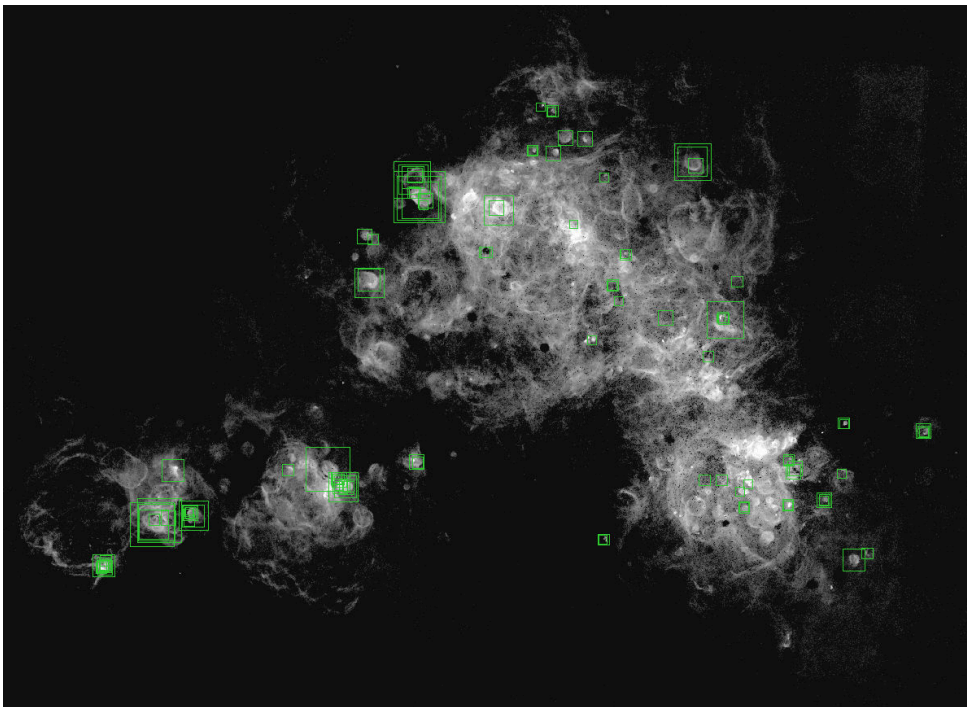


Figure 2.30: Bubbles detected in the SMC SII image at window sizes ranging from 12 to 70 pixels with square-size twice the window diameter. More noise was smoothed out of the image, and all line density thresholds were set to 12 compared to Fig. 2.18. Corresponds to settings in bottom right image in Fig. 2.24. All bubbles are listed in the appendix Tab. A.8.

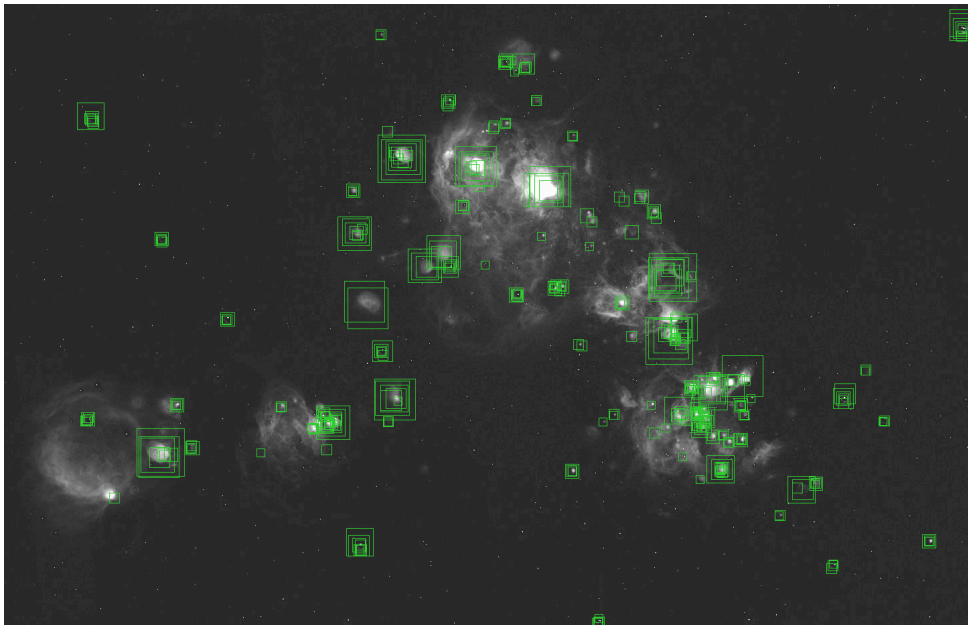


Figure 2.31: Bubbles detected in the SMC OIII image at window sizes ranging from 12 to 70 pixels with square-size twice the window diameter. Less noise was smoothed out of the image compared to Fig. 2.19. Corresponds to settings in top left image in Fig. 2.25. All bubbles are listed in the appendix Tab. A.10.

Chapter 3

Statistical and astronomical analysis

3.1 Basics of point process statistics

In this chapter, the bubble positions are checked for spatial correlations with each other and with massive stars in the LMC. Therefore, we use rigorous methods from spatial statistics. The notation and concepts are introduced in this section following the presentation of Illian et al. (2008).

The field of point process statistics provides the methods to analyze random spatial patterns of point-like objects. Here, this means the detected bubbles and stars are represented by a point pattern in two dimensions to make them mathematically accessible.

Point processes are abstract stochastic models to describe *point patterns*. Point patterns can be interpreted as realizations of a point process. Patterns are often written as a numbered list of points $\{x_1, \dots, x_n\}$, but the numbering is arbitrary and does not imply any particular order. While point patterns can be defined in more general spaces, only the Euclidean plane is relevant here due to the face-on orientation of the LMC and all further discussion will be restricted to it.

3.1.1 Marked point processes

It is possible to add further information to a pattern with marks. Marks are an additional property of each point and can be qualitative, real-valued, or more complex objects such as continuous variates. This means a pattern consisting of points $\{x_1, \dots, x_n\}$ turns into a marked pattern $\{(m_1, x_1), \dots, (m_n, x_n)\}$ where m_i is the mark of point x_i . Qualitative marks serve as discrete labels to separate the pattern into several groups, such as different tree species or trees infected or not infected with a certain disease. Here I will use qualitative marks to differentiate between stars and bubbles.

Marks can make a model a lot more powerful and make it possible to search for further correlations e.g. concerning differently qualitatively marked points or correlations between qualitative and quantitative marks.

3.1.2 Intensity

The number of points in a given Borel subset $A \subseteq \mathbb{R}^2$ is a random variable denoted by $N(A)$. For $n \in \mathbb{N}_0$, $P(N(A) = n)$ denotes the probability that there are exactly n points located in A .

For bounded A , it makes sense to calculate an expectation value \mathbf{E} of $N(A)$, which then is a measure of A :

$$\Lambda(A) = \mathbf{E}(N(A)) \tag{3.1}$$

This is called the intensity measure. If Λ is absolutely continuous with respect to the Lebesgue measure, one can define a density function λ , such that

$$\Lambda(A) = \int_A \lambda(x) dx . \tag{3.2}$$

$\lambda(x)$ is called the intensity function.

If the intensity measure is translation-invariant ($\Lambda(A) = \Lambda(A + t)$ for any A with constant $t \in \mathbb{R}^2$), the process is called homogeneous or stationary. Then $\Lambda(A) = \lambda\nu(A)$, where $\nu(A)$ is the area of A and λ is the constant intensity.

3.1.3 Summary characteristics

Often, more complex and problem-specific measures to characterize a point process or pattern than the intensity are necessary. An important function on which my further analysis is based is Ripley's K (Ripley, 1976, 1981). It is defined such that $\lambda K(r)$ is the mean amount of points within distance r to a random point in the point pattern (not counting the random point itself). Formally, it is defined using the theory of Palm distributions (see e.g. Chiu et al. 2013).

Ripley's K can be used to check patterns for clustering or regularity¹. This is usually done by comparing them to the K -function of the homogeneous Poisson process. Points of this process are completely independent and its intensity is constant, giving $K_{\text{Poisson}}(r) = \pi r^2$. If the pattern is clustered, the K -function takes values above this reference, since any point is more likely to be part of a cluster with many close neighbors. If the pattern is regular, it takes lower values, since the points are more separated.

At large r , estimators of K often have a high variance due to its cumulative nature. To mitigate this and for better visualization a variance stabilized transform called L , first proposed by Besag (1977), can be used:

$$L(r) = \sqrt{\frac{K(r)}{\pi}}. \quad (3.3)$$

In the case of a Poisson process, $L(r) = r$, so deviations can be found by comparing to a line. The pair correlation function is another popular transform of K :

$$g(r) = \frac{K'(r)}{2\pi r}. \quad (3.4)$$

It can be visualized as the normalized expected number of points in an infinitesimal ring around a random point. It is a standard function in statistical physics.

All these functions can be applied to qualitatively marked patterns by only considering points with marks of one type in relation to points of the other type. Then $\lambda_j K_{\text{cross}, i, j}(r)$ denotes the mean amount of points of type j at distance smaller than r from points of type i . L and g follow. These correlation functions are symmetric in i and j , so for the patterns of stars and bubbles here, only one direction needs to be calculated.

3.2 Comparison to distribution of massive stars

Stellar bubbles stem from massive stars (see section 1.1). This means that they should be located close to each other. In the following analysis, LMC bubbles, points in patterns generated from line densities, and massive stars described in Bonanos et al. (2009) were treated as differently marked points in a point pattern.

3.2.1 Random superposition test

To check for a possible spatial correlation, a random superposition hypothesis was tested. The test described in the following section was inspired by Lotwick and Silverman (1982) and Illian et al. (2008, Chapter 7.5). Random superposition refers to a qualitatively marked point pattern formed by combining two independent point patterns (as opposed to e.g. randomly assigning marks in an existing pattern). After combining, a summary function such as K_{cross} between the two can be calculated. Note that a simple comparison to the homogeneous Poisson case is not sufficient here since the stars are obviously clustered.

¹“Regularity” would be called “repulsion” by a physicist. It denotes a pattern with separated points.

If the datasets are uncorrelated, it should be possible to shift one of the sets relative to the other without significantly altering the summary functions, since the original positions were not special. This means that shifting the patterns often and calculating a summary function each time is a means of determining correlation. It can be implemented the following way:

The shifted patterns are treated as representations of a null hypothesis of independence. A summary function is calculated for each pattern (in the following referred to as the shifted functions). A strong deviation of the original function from the shifted functions means that the original position is special in some way, hence a positive or negative correlation can be assumed.

For determining the significance of a deviation, acceptance envelopes around the mean value of the shifted functions are generated and compared to the original function. There are three common envelope methods shown in the further plots here (for further discussion of envelope methods see Baddeley et al. 2014):

1. Pointwise envelopes: At each value of r , the respective n -th highest and lowest values of the shifted functions are plotted. If the observed function obeys the null hypothesis, it has a chance of $\alpha = 2 \cdot n / (1 + n_{\text{sim}})$ to exceed the envelope at a pre-chosen r where n_{sim} is the number of simulations. As random fluctuations exceeding the envelope at *any* point are more likely than α , this is not equal to the significance level when looking at a range of radii (Ripley, 1981; Baddeley et al., 2014). In the corresponding plots in the appendix $n_{\text{sim}} = 300$ and $n = \lfloor n_{\text{sim}}/40 \rfloor = 7$, corresponding to $\alpha \simeq 0.047$
2. Standard deviations: Pointwise standard deviations of the shifted functions can be calculated. These do not have an exact quantitative interpretation in terms of significance level since the full distribution is not known. The corresponding plots in the appendix show three standard deviation-envelopes.
3. Global Maximum Absolute Deviation (MAD): The simulated mean value is taken from $n_{\text{sim}}/2$ of the simulations. For the remaining patterns, the highest absolute deviation from this mean is calculated. Then, again the n -th largest of these deviation values is used as a critical value d_{crit} . The envelope then has upper/lower boundary values $\text{mean} \pm d_{\text{crit}}$ at a constant width $2 \cdot d_{\text{crit}}$. The null hypothesis is rejected if the observed function exceeds this envelope at any value of r . The MAD test has significance level $\alpha = n / (1 + n_{\text{sim}}/2) \simeq 0.046$ (Ripley, 1981).

The analysis described here was implemented in R using the functions `envelope`, `Kcross.inhom`, and `pcfcross.inhom` available in the `spatstat`-library (Baddeley et al., 2015). The figures in this section will show the MAD envelopes as the most rigorous method, but all envelope types are shown in the appendix chapter D.

The kernel width σ for the inhomogeneous density estimate was set to a value of 200 px which is significantly larger than the size of a typical stellar cluster in the Bonanos et al. (2009) catalog. Variation of σ down to values $\gtrsim 150$ px mostly lead to slightly larger pointwise and standard deviation envelopes, but did not change the result of the analysis. Envelopes fluctuated wildly and often appeared step-like when decreasing σ to values smaller than ~ 150 px. This is expected due to the more wildly varying intensity distribution. Since we are not interested in the positions of single stars, but rather the general distribution of clusters in the LMC (which can be described by self-correlation of stars at small distances), an intensity distribution wider than an average cluster is justifiable. An image of the intensity distribution at $\sigma = 200$ px and the stars of Bonanos et al. (2009) is shown in Fig. 3.1.

To minimize effects of the finite extension of the LMC, a rectangular region excluding its borders has been chosen for all further analysis. It is shown in Fig. 3.2. When shifting the patterns, periodic boundary conditions were used: points shifted out of the window on one side are placed inside the window on the opposite side.

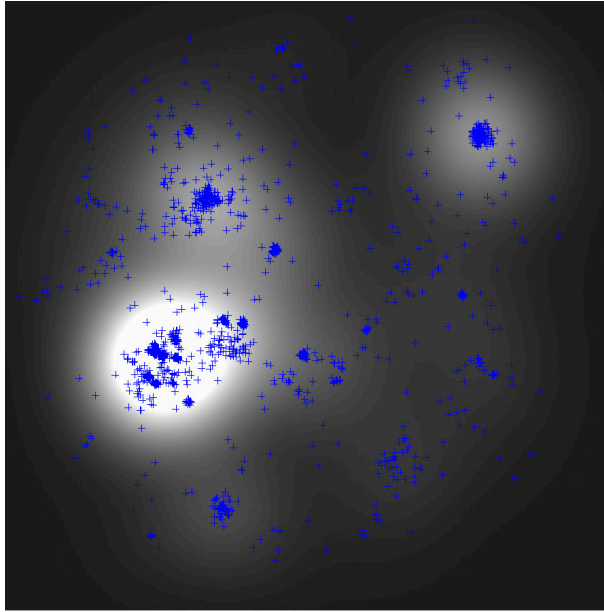


Figure 3.1: The stars of the catalogue of Bonanos et al. (2009) and their intensity distribution generated with a gaussian kernel with $\sigma = 200$ px.

3.2.2 Application of correlation test

Bubbles vs. bubbles

LMC bubbles detected in $H\alpha$, SII, and OIII were compared using Ripley's L and the listed methods. Results are shown in Fig. 3.3. All envelopes are shown in Fig. D.1.

Since many of the detected bubbles in different wavelengths are located at similar positions, the observed L quickly jumps to higher values than in the shifted patterns. As expected (since they stem from the same astronomical objects), the bubbles are highly correlated at very low distances. The null hypothesis of independence is rejected. This shows that the random superposition test is capable of finding existing correlations.

Stars vs. bubbles

Next, the bubbles were compared to the stars in Bonanos et al. (2009). The L -functions are shown in Fig. 3.5 and the pair correlation functions in Fig. 3.6. All envelopes are shown in Fig. D.2 and D.3. In all wavelengths, a significant deviation of L and the pair correlation function from the simulated mean is visible. Looking at the pair correlation function, the correlation seems to occur at radii $\lesssim 50$ px where local maxima are located, but the divergence at small r makes a more exact interpretation difficult. There seem to be a lot of bubbles and stars in very close proximity in both the shifted patterns and the original pattern, but the effect is stronger in the original case. This is what makes $g(r)$ exceed the MAD envelope.

The deviation from the null hypothesis is strongest for bubbles detected in OIII. For comparison, the combined bubbles in $H\alpha$, OIII, and the stars are shown in Fig. 3.4. The emission in OIII is less extended than in SII or $H\alpha$ and fewer bubbles were detected in general. Their distribution follows the brighter structures of the LMC more closely than the bubbles in other wavelengths, where many small bubbles are scattered wildly across the LMC. The stars also form clusters around several prominent structures and only single stars are distributed over the emptier regions, comparable to the OIII bubbles. This is due to the higher ionization of OIII. It is observable mostly around photoionizing present-day stars and less extended than the other wavelengths. Shifting the OIII bubbles is more likely to place the star clusters in empty regions, thus the stronger deviation.

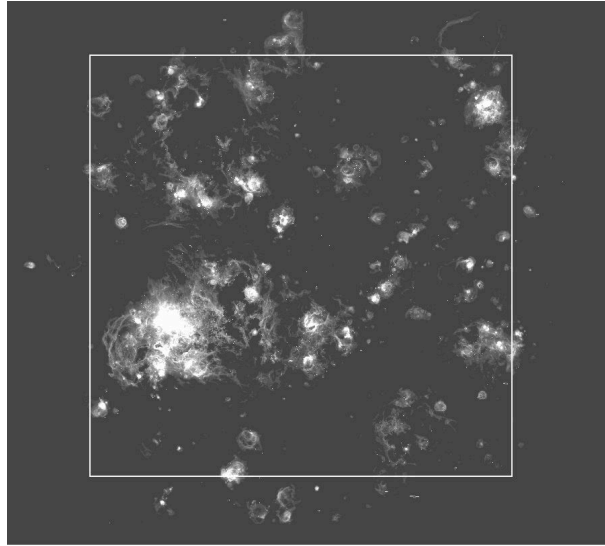


Figure 3.2: The region of the LMC selected for statistical analysis.

This comparison confirms that the bubbles detected here and massive stars are spatially correlated as expected. Thus, the spatial distribution of bubbles found seems to be a good representation of all bubbles in the LMC.

Line densities vs. stars

In order to compare the general structure of the gas to the stellar distribution, point patterns of ~ 5000 points were generated from the line densities at different window sizes. Areas with higher intensity are represented by adding multiple points at the same tile. The resulting patterns are then compared to the stars of Bonanos et al. (2009). Since the lines are perpendicular to the underlying filaments, the filaments must have been driven from some position along the line. Large line densities are expected to be an indicator of energy input by massive stars. This was used on smaller scales for bubble detection and now, on larger scales, the lines should indicate the source of larger structures.

The line density at window size 70 px ($11.7'$) is shown in Fig. 3.7 and the corresponding L-functions in Fig. 3.8. A correlation is found for $H\alpha$ and OIII, but not for SII, which only exceeds the pointwise envelope (see Fig. D.4). Again, the correlation seems to be stronger in OIII for the same reasons as above. With the exception of SII, the structure of the LMC at this scale may stem from the locations of these stars. All envelopes are shown in Fig. D.4.

SII emission and consequently its line density is more extended than the others. This is unlike the stellar distribution and the opposite of the OIII case, leading to only small deviations from the randomly shifted patterns. Large parts of the filaments only present in SII are not very bright but still cause high line densities. This may distort the pattern towards older filaments unrelated to the present-day population.

The same was done for the line densities at a window size of 250 px ($41.7'$) shown in Fig 3.9. Here, only the OIII data exceed the envelopes (Fig. 3.10, rest in Fig. D.5). This means that overall, the stars in this catalog cannot be made responsible for the large-scale structure of the LMC in $H\alpha$ and SII. It is possibly older than the massive stars currently observable. OIII, which depicts more recent and localized energy input, follows the recent star formation instead.

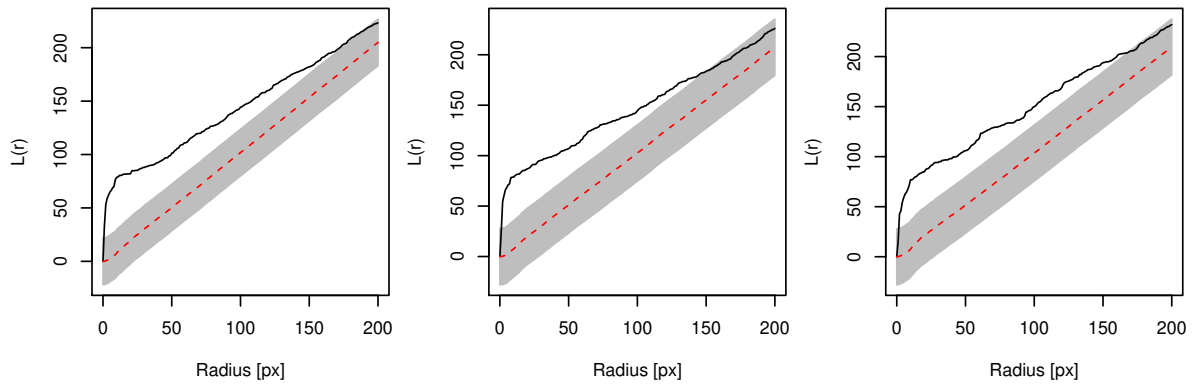


Figure 3.3: Bivariate Ripley's L comparing bubbles detected in $H\alpha$ and SII (left), $H\alpha$ and OIII (center), and SII and OIII (right). Black solid line: L estimated from original pattern, Red dashed line: pointwise mean of half of the shifted patterns, Grey envelopes: MAD. For a detailed explanation of methods see Sec. 3.2.1. All bubble sets are correlated as expected. 10 px correspond to about $1.67'$ or 24 pc at a LMC distance of 50 kpc.

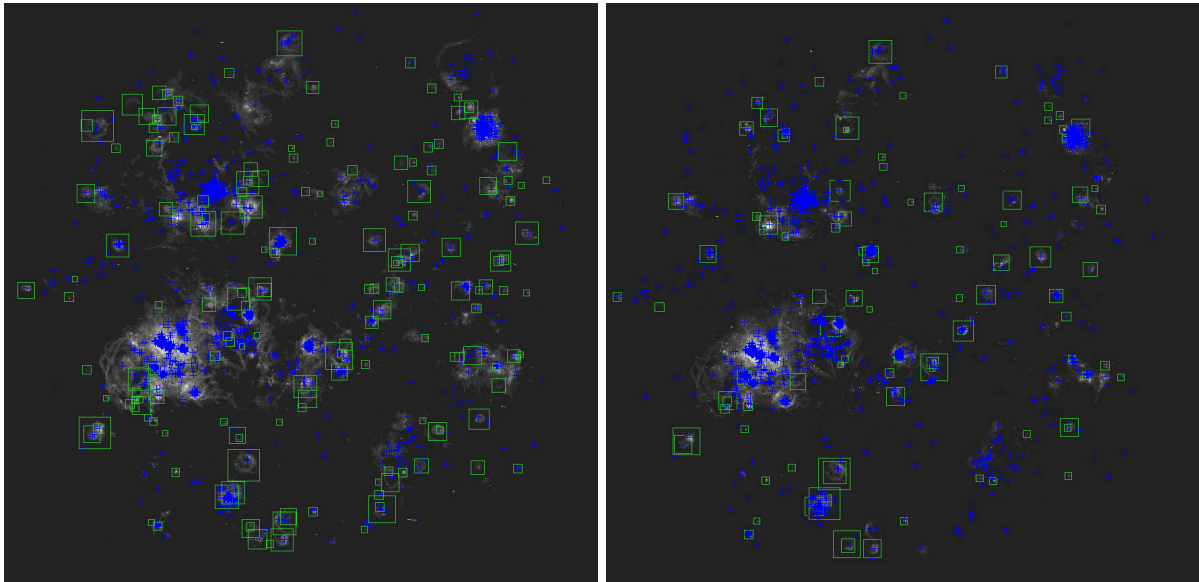


Figure 3.4: Stars in Bonanos et al. (2009) and bubbles detected in $H\alpha$ (left)/OIII (right) on the respective line emission.

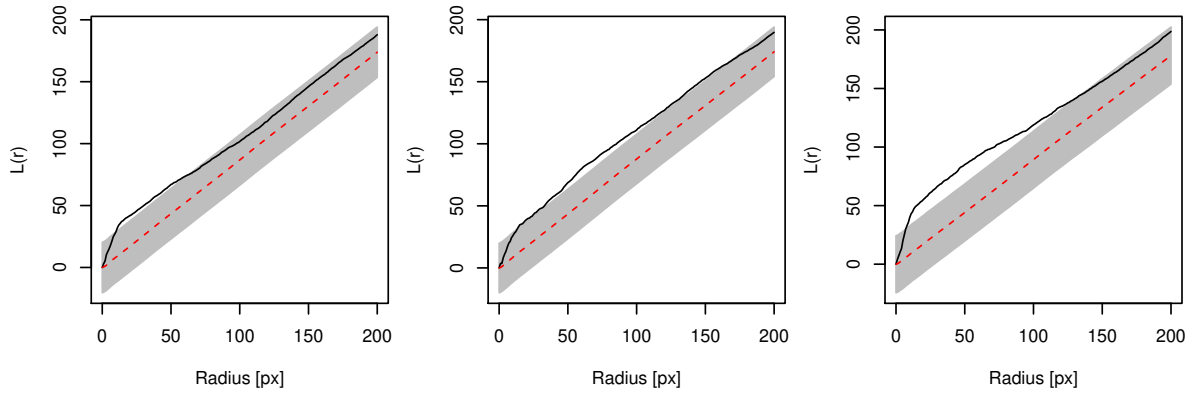


Figure 3.5: Bivariate Ripley's L comparing stars in Bonanos et al. (2009) and bubbles detected in $H\alpha$ (left), SII (center), and OIII (right). Black solid line: L estimated from original pattern, Red dashed line: pointwise mean of half of the simulated patterns, Grey envelopes: MA. For a detailed explanation of methods see Sec. 3.2.1. Stars and bubbles are correlated. 10 px correspond to about $1.67'$ or 24 pc at a LMC distance of 50 kpc.

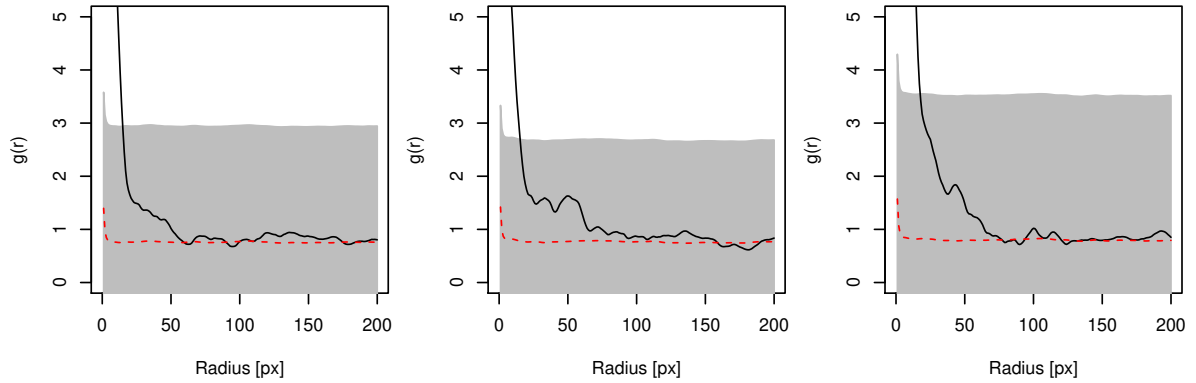


Figure 3.6: Cross-correlation function g comparing stars in Bonanos et al. (2009) and bubbles detected in $H\alpha$ (left), SII (center), and OIII (right). Black solid line: g estimated from original pattern, Red dashed line: pointwise mean of half of the simulated patterns, Grey envelopes: MAD. For a detailed explanation of methods see Sec. 3.2.1. 10 px correspond to about $1.67'$ or 24 pc at a LMC distance of 50 kpc.

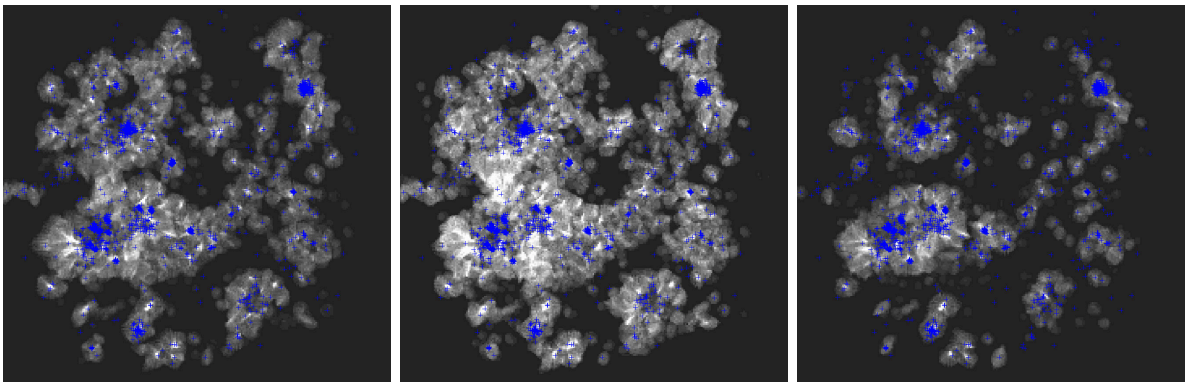


Figure 3.7: Line densities at window size 70 px ($m = 0.3$) in $H\alpha$ (left), SII (center), and OIII (right) along with stats in (Bonanos et al., 2009).

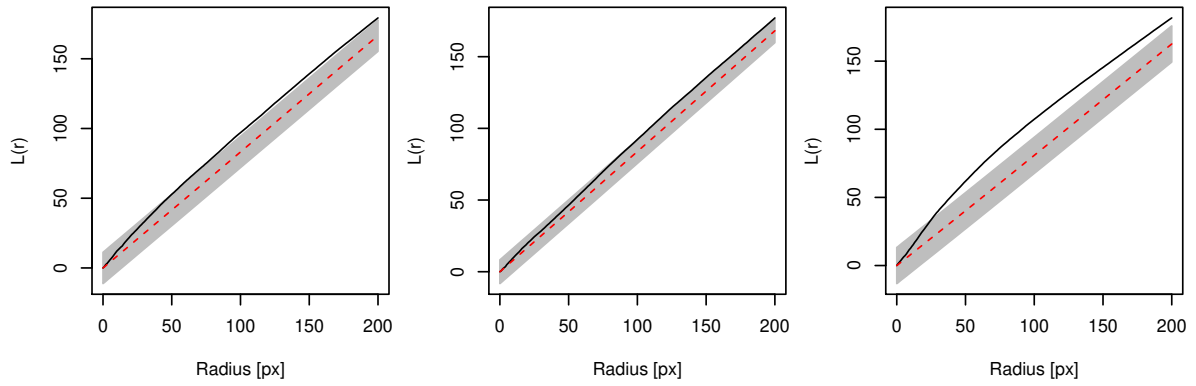


Figure 3.8: Bivariate Ripley's L comparing stars in Bonanos et al. (2009) and line densities at window size 70, $m = 0.3$, in $H\alpha$ (left), SII (center), and OIII (right). Black solid line: L estimated from original pattern, Red dashed line: pointwise mean of half of the simulated patterns, Grey envelopes: MAD. For a detailed explanation of methods see Sec. 3.2.1. Stars and structures in SII at this window size are not correlated due to the large extension of SII. 10 px correspond to about $1.67'$ or 24 pc at a LMC distance of 50 kpc.

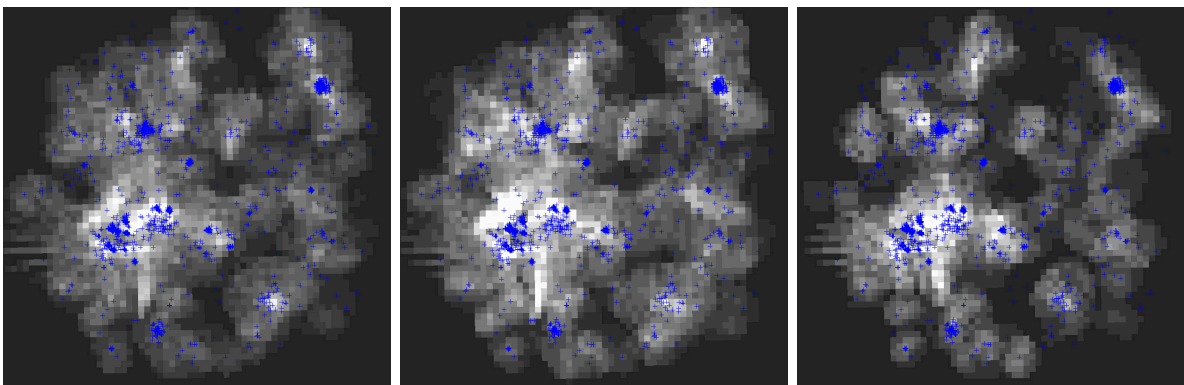


Figure 3.9: Line densities at window size 250 px ($m = 0.4$) in $H\alpha$ (left), SII (center), and OIII (right) along with stars in (Bonanos et al., 2009).

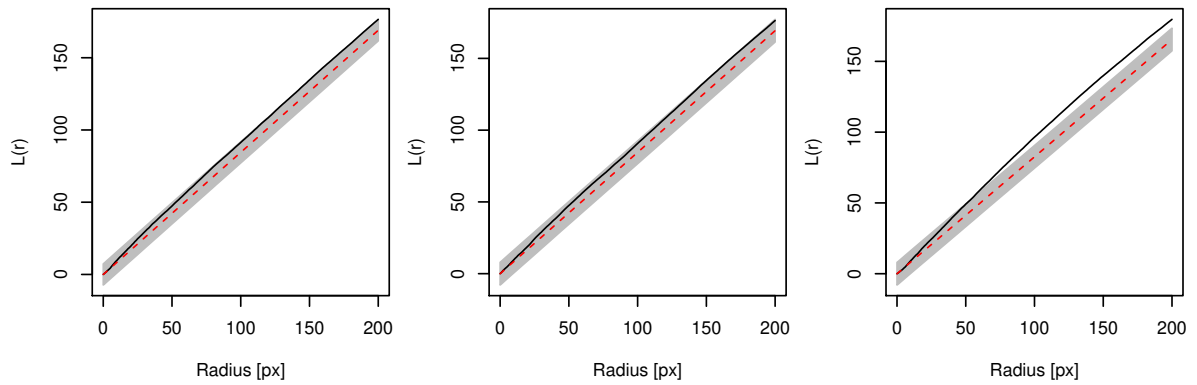


Figure 3.10: Bivariate Ripley's L comparing stars in Bonanos et al. (2009) and line densities at window size 250, $m = 0.4$, in $H\alpha$ (left), SII (center), and OIII (right). Black solid line: L estimated from original pattern, Red dashed line: pointwise mean of half of the simulated patterns, Grey envelopes: MAD. For a detailed explanation of methods see Sec. 3.2.1. Only stars and structures in OIII at this window size are correlated due to the more localized extension of OIII around modern stars. 10 px correspond to about $1.67'$ or 24 pc at a LMC distance of 50 kpc.

3.3 Notable individual regions

Not all of the possible correlations in the original images and the line density maps are suitable for analysis with the methods of the last section. This is the case for samples with small numbers like the nine LMC supergiant shells (SGS) or single regions where astronomical implications need to be discussed individually.

3.3.1 Supergiant shells, line density and star formation

Line density maps at larger scales (window size ≥ 150 px, $m = 0.4$ for all lines) were manually checked for correlations to other data. It was found that there are some correlations with the nine LMC SGS described by Meaburn (1980).

The approximate contours of the LMC shells given there are shown in $H\alpha$ in Fig. 3.11. The line densities with the same contours at 150, 250, and 400 px window size in $H\alpha$, SII, and OIII are shown in Fig. 3.12. The location of the shells was also compared to the star formation history (SFH) of the LMC as calculated by Harris and Zaritsky (2009). Maps of the star formation rate (SFR) at different points in time are shown in Fig. 3.13. Additionally, the one SMC SGS is shown in Fig. 3.14 along with the line density at window size 150 and 250 px.

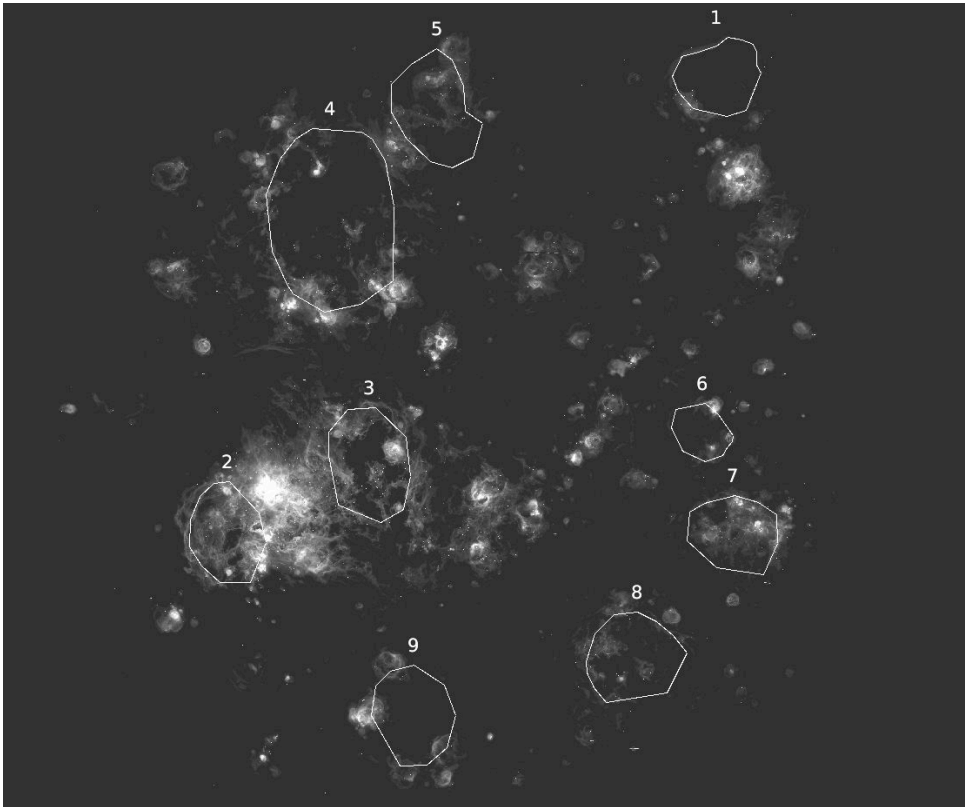


Figure 3.11: Approximate contours of the nine LMC SGS as described by Meaburn (1980) in $H\alpha$.

Notes on individual shells

No large differences in the line density behavior of the SGS in the different wavelengths are visible apart from LMC SGS 1, whose shell is not visible in OIII. Therefore the further discussion focuses on $H\alpha$ but is still valid for the other wavelengths.

The shells can be grouped with respect to their line density. There are several shells where an increase in line density is located close to their center and the maximum is contained within the shell. This is the case mainly in the 250 map for SGS 1, 5, 7, and 8. SGS 6 also contains

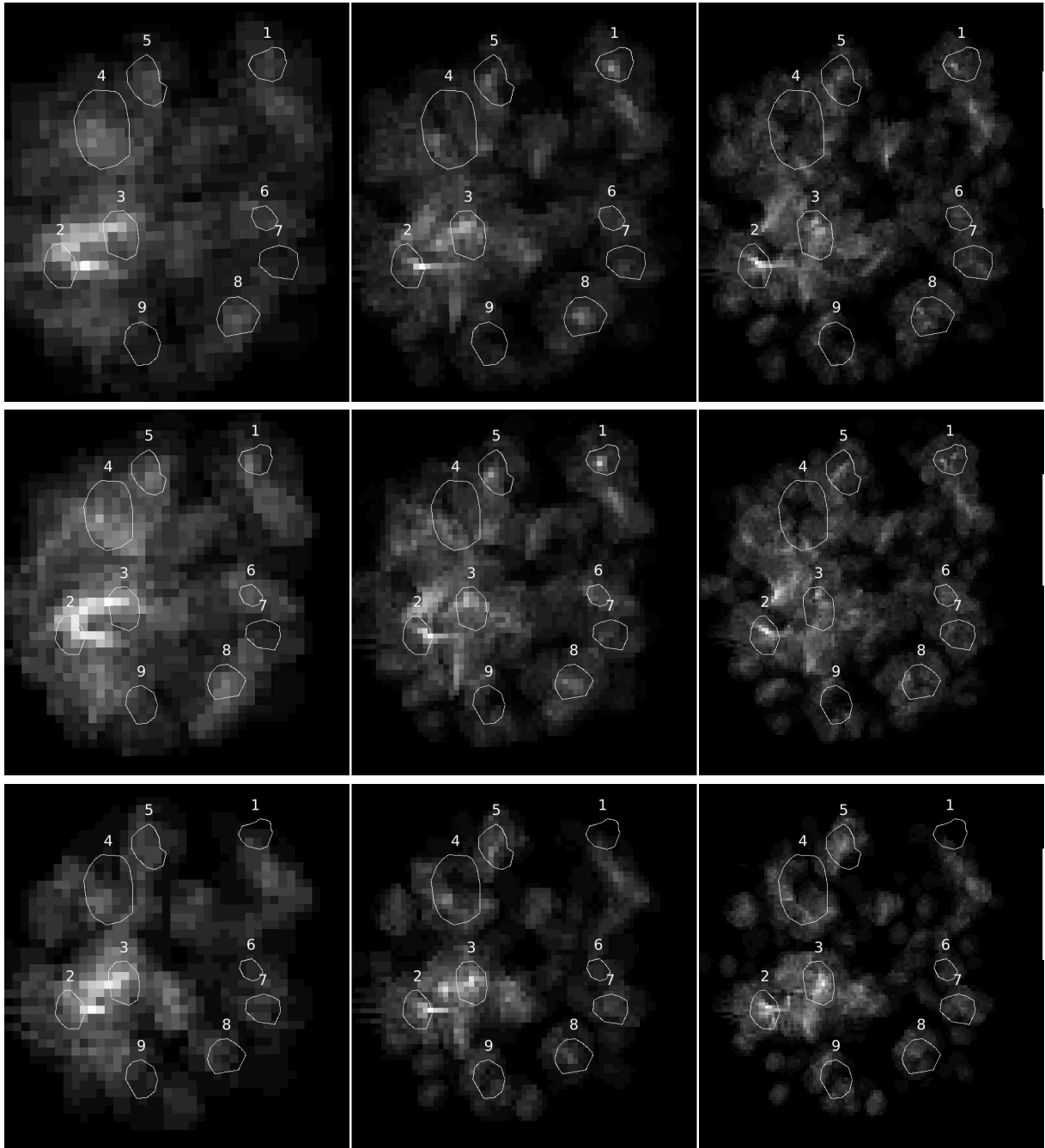


Figure 3.12: Approximate contours of the nine LMC SGS as described by Meaburn (1980) in line density maps at window size 400 (left), 250 (middle) and 150 px (right) in H α (top), SII (center), and OIII (bottom).

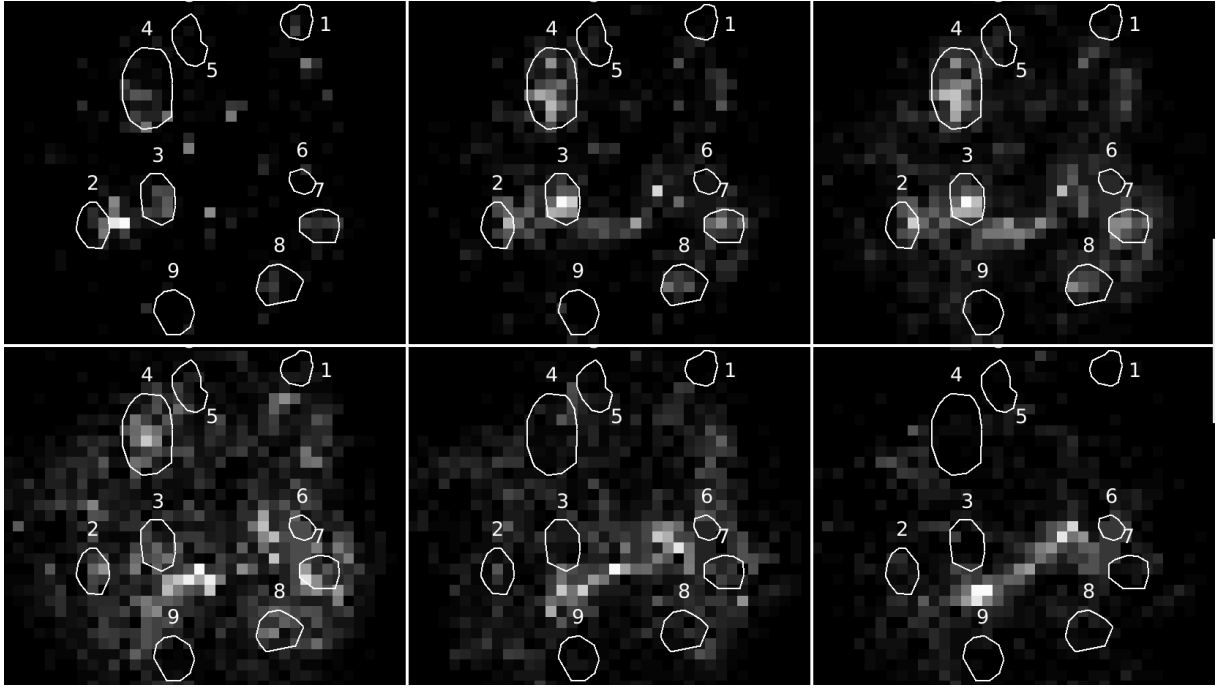


Figure 3.13: Approximate contours of the nine LMC SGS as described by Meaburn (1980) in star formation rate maps based on Harris and Zaritsky (2009). Top: 7, 15, 20 Myr; bottom: 30, 50, 100 Myr ago.

a maximum at window size 150 but is too small for larger scales. All these shells show star formation in the last 50 Myr but the SFR was comparably small in SGS 1, 6, and 5. In the latter, a stronger peak of star formation was shifted closer to SGS 4.

SMC SGS 1 is the only SGS in the SMC and can also be added to this group. It contains an increased line density due to its round shell. Ramachandran et al. (2019) analyzed the star formation history of the region with regard to the energy input into the ISM. They concluded that the shell was probably produced by stars formed in a star formation peak in the past ~ 50 Myr.

Others have distinct maxima that are off-center and partially reach out of the shell. This is mainly the case for SGS 3, where the maximum is always in the northern half and reaches out into the northeast at larger scales, and SGS 4, where the maximum is in the southeastern half and at window size 150 many local maxima appear at the edge. This means that the overall structure of SGS 4 was shaped from its inside out and more recently formed stars have caused smaller structures in the south. This is also visible in the star formation maps. In SGS 3, however, most structure seems to come from within the shell and the elongated maximum at 400 px was caused by long lines from filaments northeast of the shell.

SGS 9 is only weakly visible in the line density maps and mostly at smaller scales around its edge. The SFH shows only weak star formation in recent times there, which might have caused the bubbles, similarly to SGS 4. Stars have not formed in its center for the last 100 Myr which may be related to its location at the edge of the galaxy.

SGS 2 seems to be a special case; it is close to the region with the highest line density at larger scales: In $|\psi_2|$ maps, the region east of 30 Dor shows very high values due to its strong filaments (see Fig. 2.4). Combined with their bowed shape this causes long lines leading to an increased line density south of 30 Dor. The maximum is roughly located west of SGS 2; the exact location depends on the window size. Close to this maximum there is also the region of highest star formation in recent times (≤ 7 Myr).

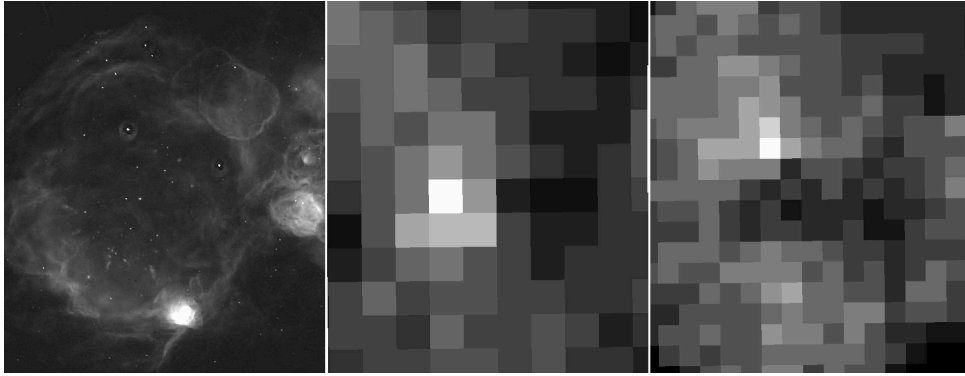


Figure 3.14: SMC SGS 1 (Meaburn, 1980) in $H\alpha$ (left) and the corresponding line densities at window size 250 (middle) and 150 px (right). $m = 0.4$ for all lines.

Conclusion

As they are large structures formed by several generations of star formation, one would expect SGS to cause an increase in line density within their shell. It is indeed possible that the SGS in general are correlated to increased line density as most contain at least a region with a local maximum, but their low number makes it difficult to make a more confident statement. Since both line density and SGS correlate to the gas emission (in “empty” regions, there are neither lines nor SGS), an uncritical analysis may produce false positives.

Additionally, almost all SGS show an increase in SFR at some point in their history, as would be expected. Only LMC SGS 9 is an exception to both rules. This may be related to its location at the edge of the galaxy where the surrounding medium may be different.

The relation between line density and SFR could be taken further and a correlation proposed. For window size 250, there are indeed similarities between the line density and the SFR 7-20 Myr ago. There are some differences such as the high SFR in SGS 4 without a comparably strong counterpart. The local conditions and exact shape of filaments created by star formation can strongly affect the line density. Not all regions with high energy input were able to create nicely detectable filaments.

3.3.2 Line density and SMC X-ray emission

For the SMC, diffuse X-ray emission was compared to the line density at large scales. A SMC $H\alpha$ image along with X-ray data is shown in Fig. 3.15. Regions of increased line density and increased energy input as in Collischon (2017) are marked.

In Collischon (2017) I calculated the energy input by massive stars into the ISM in recent times based on the star formation history of Harris and Zaritsky (2004). Areas with high input do not coincide with regions of diffuse X-ray emission as one might expect; this X-ray emission is rather shifted to the northwest.

The regions with high energy input are shown in Fig. 3.15 as yellow contours. The shifted X-ray emission is visible on the western and northwestern side of the SMC. Comparing to the line density at large scales (red contours in the same image), there is some overlap between line density and X-rays in the area in question. No such correlation appears when comparing to the SII or OIII line density.

In the rest of the SMC, the correlation is not clear: In the brighter regions in $H\alpha$, the structure is too irregular to cause long lines and a high line density. SMC SGS 1 on the eastern end has a high line density, but rather low X-ray luminosity (it is not included in the SFH data). DEM S 157 (Davies et al., 1976) and its surroundings in the east next to the SGS have both high energy input and line density and are visible in the X-ray image. It is positioned at the southeastern yellow square in Fig. 3.15.

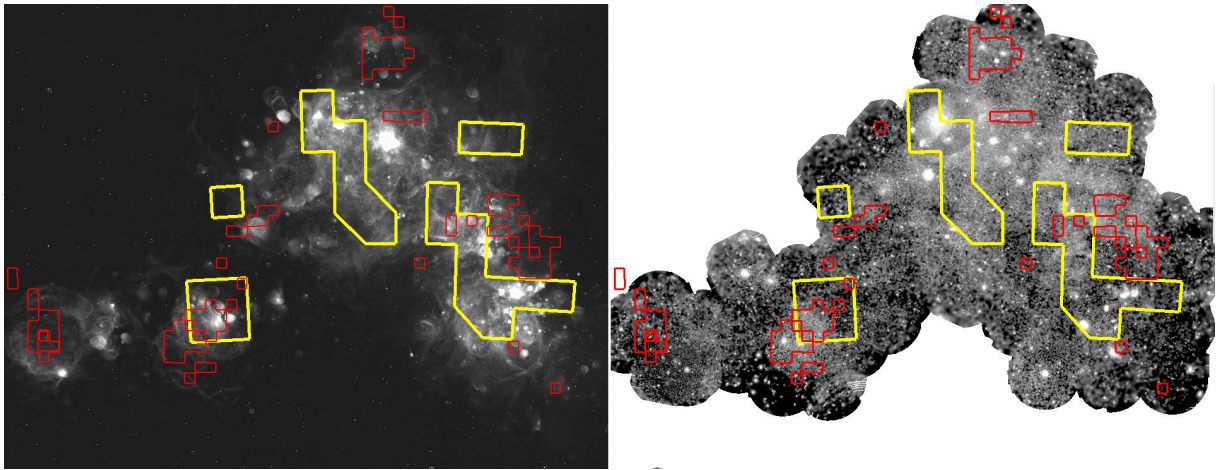


Figure 3.15: SMC in $H\alpha$ (left) and soft X-ray (right). Red contours: areas with increased line density at window size 250 px ($m = 0.4$); yellow contours: areas with increased energy input into the SMC in recent times as in Collischon (2017).

Chapter 4

Summary and Outlook

I have introduced an automatic bubble detection method using Minkowski tensors. Minkowski tensors are additive shape indicators of convex bodies and can be extended to bodies consisting of a finite union of convex bodies. They can be applied to a grayscale image by choosing several thresholds to get a discrete shape, calculating them in a marching square, and then smoothing to create Minkowski maps for any window size. The irreducible Minkowski tensor ψ_2 responds to elongated structures such as filaments.

With maps of ψ_2 at one window size, lines are drawn perpendicular to the filaments. All lines from the borders of a bubble meet in the center, so areas with high line density are identified as bubble candidates. In general, line densities at a given window size show the regions where structures at that scale originate. A candidate is accepted if $|\psi_2|$ does not rise for increased window size, because contributions from all sides of the bubble cancel out. The method successfully finds a large amount of bubbles in the LMC in $H\alpha$, SII, and OIII. Several parameters need to be adjusted manually, but it is possible to get surprisingly accurate results without a time-consuming optimization. Image noise disturbs the detection, but should not be completely excluded by higher thresholds as a loss of structure deteriorates the detection more than the noise.

Methods of spatial statistics were used to compare the LMC bubble distribution to that of massive present-day stars of Bonanos et al. (2009). It was found that the bubbles correlate with the massive stars. The detected sample is thus a good representation of the actual distribution of bubbles. Line densities at window sizes 70 and 250 px (corresponding to $11.7'/170$ pc and $41.7'/600$ pc) representing structures at the two sizes were also compared to the stellar distribution. The OIII structures show a strong correlation due to the more localized distribution of the doubly ionized oxygen around massive stars. The SII line densities correlate at neither scale with the stars. SII emission is more extended and possibly stems from older stars than those observed today. $H\alpha$ lines correlate to the stars at 70 px, but not at 250 px, meaning that only the large structures here are older.

A possible correlation was found between the large scale line densities and the LMC SGS. All SGS show a local maximum in line density in $H\alpha$ and SII, and most in OIII, but due to their low number, a more definite statement cannot be made. A correlation between line density and recent star formation in general is possible. The SMC line density was also compared to the X-ray emission and while no general statement can be made, there is some overlap between diffuse emission and line density increase.

The bubble detection parameter optimization is still in need of improvement. The methods used here could, for example, be used as a preselection presented to a neural network making final decisions between bubbles and non-bubbles and enabling an automatic parameter adjustment.

While it was useful that the analysis methods presented here do not rely on large training data sets, they would certainly profit from application to more image data. Especially the usefulness of line density maps could be verified and the correlations to SGS and star formation tested.

Bibliography

- Anderson, L. D., Bania, T. M., Jackson, J. M., Clemens, D. P., Heyer, M., Simon, R., Shah, R. Y., and Rathborne, J. M. (2009). The Molecular Properties of Galactic H II Regions. *ApJS*, 181(1):255–271.
- Asplund, M., Grevesse, N., Sauval, A. J., and Scott, P. (2009). The Chemical Composition of the Sun. *ARA&A*, 47:481–522.
- Baddeley, A., Diggle, P. J., Hardegen, A., Lawrence, T., Milne, R. K., and Nair, G. (2014). On tests of spatial pattern based on simulation envelopes. *Ecological Monographs*, 84(3):477–489.
- Baddeley, A., Rubak, E., and Turner, R. (2015). *Spatial Point Patterns: Methodology and Applications with R*. Chapman and Hall/CRC, London.
- Besag, J. (1977). Discussion on dr ripley’s paper. *Journal of the Royal Statistical Society: Series B (Methodological)*, 39(2):193–195.
- Bonanos, A. Z., Massa, D. L., Sewilo, M., Lennon, D. J., Panagia, N., Smith, L. J., Meixner, M., Babler, B. L., Bracker, S., Meade, M. R., Gordon, K. D., Hora, J. L., Indebetouw, R., and Whitney, B. A. (2009). Spitzer SAGE Infrared Photometry of Massive Stars in the Large Magellanic Cloud. *AJ*, 138(4):1003–1021.
- Castor, J., McCray, R., and Weaver, R. (1975). Interstellar bubbles. *ApJ*, 200:L107–L110.
- Chiu, S., Stoyan, D., Kendall, W., and Mecke, J. (2013). *Stochastic Geometry and Its Applications*. Wiley Series in Probability and Statistics. Wiley.
- Choi, Y., Nidever, D. L., Olsen, K., Blum, R. D., Besla, G., Zaritsky, D., van der Marel, R. P., Bell, E. F., Gallart, C., Cioni, M.-R. L., Johnson, L. C., Vivas, A. K., Saha, A., de Boer, T. J. L., Noël, N. E. D., Monachesi, A., Massana, P., Conn, B. C., Martinez-Delgado, D., Muñoz, R. R., and Stringfellow, G. S. (2018). SMASHing the LMC: A Tidally Induced Warp in the Outer LMC and a Large-scale Reddening Map. *ApJ*, 866(2):90.
- Chu, Y.-H. (2008). Bubbles and Superbubbles: Observations and Theory. In Bresolin, F., Crowther, P. A., and Puls, J., editors, *Massive Stars as Cosmic Engines*, volume 250 of *IAU Symposium*, pages 341–354.
- Collischon, C. (2017). Heating of the interstellar medium in the Small Magellanic Cloud by massive stars. Bachelor’s Thesis, Friedrich-Alexander Universität Erlangen-Nürnberg.
- Cox, D. P. (2005). The Three-Phase Interstellar Medium Revisited. *ARA&A*, 43(1):337–385.
- Davies, R. D., Elliott, K. H., and Meaburn, J. (1976). The nebular complexes of the Large and Small Magellanic Clouds. *MmRAS*, 81:89.
- de Grijs, R. and Bono, G. (2015). Clustering of Local Group Distances: Publication Bias or Correlated Measurements? III. The Small Magellanic Cloud. *AJ*, 149(6):179.
- Fesen, R. A., Blair, W. P., and Kirshner, R. P. (1985). Optical emission-line properties of evolved galactic supernova remnants. *ApJ*, 292:29–48.

- Filipovic, M. D., Haynes, R. F., White, G. L., and Jones, P. A. (1998). A radio continuum study of the Magellanic Clouds. VII. Discrete radio sources in the Magellanic Clouds. *A&AS*, 130:421–440.
- Franco, J., Tenorio-Tagle, G., and Bodenheimer, P. (1990). On the Formation and Expansion of H II Regions. *ApJ*, 349:126.
- Göring, D., Klatt, M. A., Stegmann, C., and Mecke, K. (2013). Morphometric analysis in gamma-ray astronomy using Minkowski functionals. Source detection via structure quantification. *A&A*, 555:A38.
- Hadwiger, H. (1957). *Vorlesungen Über Inhalt, Oberfläche und Isoperimetrie*. Springer Berlin Heidelberg.
- Harris, J. and Zaritsky, D. (2004). The Star Formation History of the Small Magellanic Cloud. *AJ*, 127:1531–1544.
- Harris, J. and Zaritsky, D. (2009). The Star Formation History of the Large Magellanic Cloud. *AJ*, 138(5):1243–1260.
- Hikage, C. and Matsubara, T. (2012). Limits on second-order non-Gaussianity from Minkowski functionals of WMAP 7-year data. *MNRAS*, 425(3):2187–2196.
- Hollenbach, D. J. and Tielens, A. G. G. M. (1997). Dense Photodissociation Regions (PDRs). *ARA&A*, 35:179–216.
- Illian, J., Penttinen, P., Stoyan, H., and Stoyan, D. (2008). *Statistical Analysis and Modelling of Spatial Point Patterns*. Statistics in Practice. Wiley.
- Kapfer, S., Wagner, J., and Schaller, F. (2019). papaya2. <https://morphometry.org/software/papaya2/>.
- Kerscher, M., Mecke, K., Schmalzing, J., Beisbart, C., Buchert, T., and Wagner, H. (2001a). Morphological fluctuations of large-scale structure: The PSCz survey. *A&A*, 373:1–11.
- Kerscher, M., Mecke, K., Schuecker, P., Böhringer, H., Guzzo, L., Collins, C. A., Schindler, S., De Grandi, S., and Cruddace, R. (2001b). Non-Gaussian morphology on large scales: Minkowski functionals of the REFLEX cluster catalogue. *A&A*, 377:1–16.
- Klatt, M. A. and Mecke, K. (2019). Detecting structured sources in noisy images via Minkowski maps. *EPL (Europhysics Letters)*, 128:60001.
- Lotwick, H. W. and Silverman, B. W. (1982). Methods for analysing spatial processes of several types of points. *Journal of the Royal Statistical Society: Series B (Methodological)*, 44(3):406–413.
- Mac Low, M.-M. and McCray, R. (1988). Superbubbles in Disk Galaxies. *ApJ*, 324:776.
- Mantz, H., Jacobs, K., and Mecke, K. (2008). Utilizing minkowski functionals for image analysis: a marching square algorithm. *Journal of Statistical Mechanics: Theory and Experiment*, 2008(12):P12015.
- Mathewson, D. S., Ford, V. L., Tuohy, I. R., Mills, B. Y., Turtle, A. J., and Helfand, D. J. (1985). Supernova remnants in the Magellanic Clouds. III. *ApJS*, 58:197–200.
- McKee, C. F. and Ostriker, J. P. (1977). A theory of the interstellar medium - Three components regulated by supernova explosions in an inhomogeneous substrate. *ApJ*, 218:148–169.
- Meaburn, J. (1980). The giant and supergiant shells of the Magellanic Clouds. *MNRAS*, 192:365–375.

- Nadyozhin, D. K. and Razinkova, T. L. (2005). Similarity Theory of Stellar Models and the Structure of Very Massive Stars. *Astronomy Letters*, 31:695–705.
- Oey, M. S. (2007). Towards resolving the evolution of multi-supernova superbubbles. In Elmegreen, B. G. and Palous, J., editors, *Triggered Star Formation in a Turbulent ISM*, volume 237 of *IAU Symposium*, pages 106–113.
- Osterbrock, D. E. (1988). The Physics of Gaseous Nebulae. *PASP*, 100:412.
- Osterbrock, D. E. and Ferland, G. J. (2006). *Astrophysics of gaseous nebulae and active galactic nuclei*.
- Pietrzyński, G., Graczyk, D., Gallenne, A., Gieren, W., Thompson, I. B., Pilecki, B., Karczmarek, P., Górski, M., Suchomska, K., Taormina, M., Zgirski, B., Wielgórski, P., Kołaczkowski, Z., Konorski, P., Villanova, S., Nardetto, N., Kervella, P., Bresolin, F., Kudritzki, R. P., Storm, J., Smolec, R., and Narloch, W. (2019). A distance to the Large Magellanic Cloud that is precise to one per cent. *Nature*, 567(7747):200–203.
- Ramachandran, V., Hamann, W. R., Oskinova, L. M., Gallagher, J. S., Hainich, R., Shenar, T., Sand er, A. A. C., Todt, H., and Fulmer, L. (2019). Testing massive star evolution, star formation history, and feedback at low metallicity. Spectroscopic analysis of OB stars in the SMC Wing. *A&A*, 625:A104.
- Reynolds, R. J. (1985). Detection of the forbidden O III lambda 5007 emission line in the Galactic background. *ApJ*, 298:L27–L30.
- Ripley, B. D. (1976). The second-order analysis of stationary point processes. *Journal of Applied Probability*, 13(2):255–266.
- Ripley, B. D. (1981). *Spatial Statistics*. Wiley Series in Probability and Statistics. Wiley.
- Russell, S. C. and Dopita, M. A. (1992). Abundances of the heavy elements in the Magellanic Clouds. III - Interpretation of results. *ApJ*, 384:508–522.
- Schaller, F. (2019). Morphometer. <https://morphometry.org/software/morphometer/>.
- Schröder-Turk, G., Kapfer, S., Breidenbach, B., Beisbart, C., and Mecke, K. (2010). Tensorial minkowski functionals and anisotropy measures for planar patterns. *Journal of Microscopy*, 238(1):57–74.
- Schröder-Turk, G. E., Mickel, W., Kapfer, S. C., Klatt, M. A., Schaller, F. M., Hoffmann, M. J. F., Kleppmann, N., Armstrong, P., Inayat, A., Hug, D., Reichelsdorfer, M., Peukert, W., Schwieger, W., and Mecke, K. (2011). Minkowski tensor shape analysis of cellular, granular and porous structures. *Advanced Materials*, 23(22-23):2535–2553.
- Schröder-Turk, G. E., Mickel, W., Kapfer, S. C., Schaller, F. M., Breidenbach, B., Hug, D., and Mecke, K. (2013). Minkowski tensors of anisotropic spatial structure. *New Journal of Physics*, 15(8):083028.
- Smith, C., Leiton, R., and Pizarro, S. (2000). *The UM/CTIO Magellanic Cloud Emission Line Survey (MCELS)*, volume 221 of *Astronomical Society of the Pacific Conference Series*, page 83.
- Stupar, M., Parker, Q. A., and Frew, D. J. (2018). Confirmation of G6.31+0.54 as a part of a Galactic supernova remnant. *MNRAS*, 479:4432–4439.
- Vink, J. S., de Koter, A., and Lamers, H. J. G. L. M. (2001). Mass-loss predictions for O and B stars as a function of metallicity. *A&A*, 369:574–588.

Weaver, R., McCray, R., Castor, J., Shapiro, P., and Moore, R. (1977). Interstellar bubbles. II - Structure and evolution. *ApJ*, 218:377–395.

Westerlund, B. E. (1997). *The Magellanic Clouds*.

Appendix A

Detected bubble tables

A.1 LMC

Table A.1: Combined bubbles detected in the LMC SII image. Size refers to the size of the surrounding square and is mostly slightly larger than the bubble itself.

Nr	RA	DEC	Size	Nr	RA	DEC	Size	Nr	RA	DEC	Size
0	5:28:02.0	-65:50:12.9	368.0"	46	5:10:26.7	-68:30:20.7	350.0"	92	5:48:28.3	-70:02:57.6	400.0"
1	5:00:17.6	-66:05:40.6	313.3"	47	4:55:46.9	-68:39:38.8	433.3"	93	5:28:48.9	-70:19:08.9	500.0"
2	4:58:16.3	-66:22:16.5	240.0"	48	5:02:15.9	-69:04:21.7	300.0"	94	5:17:47.3	-71:15:41.2	500.0"
3	5:22:43.1	-66:39:20.3	240.0"	49	5:31:29.7	-69:18:55.6	350.0"	95	5:37:11.7	-66:39:27.8	700.0"
4	5:23:00.4	-66:41:18.2	240.0"	50	4:58:06.9	-69:17:01.9	350.0"	96	5:14:17.1	-67:16:55.0	700.0"
5	5:20:35.0	-66:46:47.8	260.0"	51	4:52:20.2	-69:20:57.0	300.0"	97	5:27:00.0	-67:19:07.9	600.0"
6	5:05:20.7	-66:55:36.9	310.0"	52	5:21:46.7	-69:59:53.7	300.0"	98	5:25:53.2	-67:29:49.7	1028.5"
7	5:12:56.4	-67:02:57.0	240.0"	53	5:30:46.5	-70:07:34.8	350.0"	99	5:55:56.2	-68:14:21.3	700.0"
8	4:48:28.7	-67:00:19.5	313.3"	54	4:59:26.7	-70:11:46.5	300.0"	100	5:26:16.4	-69:12:09.2	700.0"
9	5:17:01.8	-67:20:38.9	270.0"	55	5:01:48.7	-70:39:33.0	537.5"	101	5:14:13.5	-69:21:10.5	880.0"
10	4:53:39.0	-67:23:41.2	240.0"	56	5:35:58.7	-70:38:31.6	300.0"	102	5:32:46.3	-69:38:33.6	600.0"
11	5:20:44.5	-68:00:48.9	240.0"	57	5:06:30.8	-70:44:34.1	350.0"	103	5:43:03.6	-69:40:51.7	600.0"
12	5:24:16.5	-68:01:12.1	270.0"	58	5:04:31.5	-70:44:38.7	350.0"	104	5:47:16.6	-69:42:35.8	600.0"
13	5:22:53.4	-68:04:20.2	335.0"	59	5:28:18.1	-71:04:43.6	350.0"	105	4:53:48.3	-70:01:30.1	800.0"
14	4:43:09.1	-67:56:04.1	240.0"	60	5:07:44.6	-71:10:33.7	350.0"	106	4:59:46.6	-70:12:17.5	800.0"
15	5:06:14.6	-68:16:20.6	240.0"	61	5:25:16.6	-71:28:22.9	300.0"	107	4:50:46.9	-70:51:38.0	600.0"
16	5:07:17.3	-68:26:00.2	313.3"	62	5:26:20.7	-71:36:02.0	350.0"	108	5:22:41.5	-71:36:59.9	700.0"
17	5:03:20.4	-68:27:26.5	260.0"	63	5:06:17.1	-65:43:13.9	600.0"	109	5:35:59.6	-66:19:30.3	933.3"
18	4:55:38.3	-68:26:11.7	313.3"	64	4:58:55.6	-66:12:24.3	600.0"	110	5:43:09.1	-67:08:50.1	800.0"
19	4:49:13.9	-68:24:31.4	313.3"	65	5:32:25.7	-66:28:02.2	700.0"	111	5:27:16.6	-67:26:14.5	800.0"
20	5:09:28.7	-68:46:25.8	240.0"	66	5:37:35.0	-66:28:41.1	400.0"	112	4:50:15.8	-67:41:03.5	900.0"
21	5:27:50.5	-69:12:30.7	240.0"	67	5:42:27.1	-66:39:38.8	400.0"	113	4:53:14.7	-68:04:30.6	933.3"
22	5:29:25.0	-69:13:28.9	240.0"	68	5:25:33.2	-67:01:50.8	640.0"	114	4:54:30.2	-68:24:03.0	800.0"
23	4:48:59.9	-69:10:20.1	270.0"	69	5:12:55.9	-67:02:50.2	600.0"	115	4:58:04.8	-68:27:48.0	800.0"
24	5:26:38.2	-69:19:45.4	240.0"	70	4:53:19.8	-66:57:04.6	400.0"	116	5:27:50.9	-68:34:56.7	1100.0"
25	5:47:21.4	-69:42:19.4	260.0"	71	4:55:34.8	-67:08:41.5	680.0"	117	5:24:17.9	-68:38:47.5	800.0"
26	4:54:14.4	-70:02:00.0	260.0"	72	5:33:02.4	-67:23:06.7	400.0"	118	5:26:27.6	-68:59:00.1	933.3"
27	5:40:52.7	-70:03:02.8	313.3"	73	5:36:02.9	-67:34:28.6	400.0"	119	5:15:28.1	-69:00:49.7	900.0"
28	4:54:24.7	-70:03:22.1	240.0"	74	5:23:10.5	-67:52:55.7	400.0"	120	5:17:30.8	-69:05:13.7	800.0"
29	5:22:43.4	-70:09:13.3	270.0"	75	5:05:55.4	-68:01:34.6	400.0"	121	5:32:23.8	-69:05:11.4	1000.0"
30	5:48:28.1	-70:02:47.7	240.0"	76	5:05:04.0	-68:02:27.6	700.0"	122	4:50:42.4	-69:26:12.7	800.0"
31	5:39:23.4	-70:12:50.7	270.0"	77	5:09:41.0	-68:28:27.6	400.0"	123	5:43:56.8	-69:56:06.7	800.0"
32	5:04:27.4	-70:28:57.6	313.3"	78	5:26:50.4	-68:50:52.3	600.0"	124	5:08:30.1	-70:55:14.0	800.0"
33	5:06:40.2	-70:33:11.6	240.0"	79	5:09:49.3	-68:55:32.4	700.0"	125	5:31:25.2	-71:03:19.0	800.0"
34	5:34:26.8	-70:33:33.9	313.3"	80	5:29:28.1	-69:08:47.9	400.0"	126	5:21:52.6	-71:20:49.9	933.3"
35	5:38:22.6	-70:42:22.9	335.0"	81	5:13:24.7	-69:12:10.1	500.0"	127	5:20:47.5	-71:22:00.7	800.0"
36	5:41:44.6	-71:20:23.2	356.0"	82	5:28:56.5	-69:12:55.8	400.0"	128	5:27:42.8	-71:27:08.5	800.0"
37	5:34:32.8	-66:16:22.2	525.0"	83	5:19:21.6	-69:14:42.6	400.0"	129	5:04:25.4	-67:17:35.7	1100.0"
38	5:00:14.5	-66:16:16.3	433.3"	84	5:32:02.7	-69:13:05.3	400.0"	130	5:32:01.4	-67:40:18.4	1100.0"
39	5:15:45.8	-66:42:22.5	300.0"	85	5:08:37.8	-69:28:47.0	400.0"	131	5:28:32.9	-67:41:17.4	1100.0"
40	4:52:40.0	-67:18:05.9	433.3"	86	5:40:20.4	-69:24:51.0	400.0"	132	4:59:57.2	-67:56:31.5	1000.0"
41	5:04:57.9	-67:35:29.1	525.0"	87	5:21:11.5	-69:33:07.0	400.0"	133	5:20:27.9	-69:18:49.8	1000.0"
42	5:43:27.8	-67:51:04.5	716.6"	88	4:59:08.7	-69:32:55.0	400.0"	134	5:30:18.4	-71:01:29.8	1133.0"
43	5:43:13.6	-67:52:08.0	300.0"	89	5:14:07.1	-69:37:33.8	400.0"	135	5:20:57.1	-65:28:57.5	1200.0"
44	5:21:35.9	-68:10:55.2	300.0"	90	5:44:09.7	-69:47:12.3	700.0"	136	5:16:06.4	-69:31:41.2	1400.0"
45	5:25:09.7	-68:29:09.6	300.0"	91	5:19:23.4	-69:58:16.6	500.0"	137	5:28:10.7	-70:40:16.6	1400.0"

Table A.2: Combined bubbles detected in the LMC H α image. Size refers to the size of the surrounding square and is mostly slightly larger than the bubble itself.

Nr	RA	DEC	Size	Nr	RA	DEC	Size	Nr	RA	DEC	Size
0	5:00:17.6	-66:05:40.6	313.3"	57	5:09:52.5	-68:54:47.5	557.1"	114	5:37:42.6	-66:42:18.7	666.6"
1	4:58:18.3	-66:21:52.4	270.0"	58	5:10:32.8	-69:26:07.8	350.0"	115	5:06:52.0	-66:56:07.6	600.0"
2	5:32:35.7	-66:28:43.7	240.0"	59	5:42:35.2	-69:46:18.0	300.0"	116	5:25:45.2	-67:01:52.7	600.0"
3	5:20:36.1	-66:46:46.0	270.0"	60	5:19:28.3	-69:58:31.4	350.0"	117	5:24:37.1	-67:08:44.1	700.0"
4	5:20:21.3	-66:54:01.5	368.0"	61	5:43:22.5	-69:51:54.2	350.0"	118	4:55:41.6	-67:08:55.1	750.0"
5	5:05:19.2	-66:55:31.5	313.3"	62	4:59:26.7	-70:11:46.5	300.0"	119	5:43:26.2	-67:51:20.5	1000.0"
6	4:51:28.9	-67:06:14.9	270.0"	63	5:28:42.3	-70:19:50.3	300.0"	120	5:05:08.6	-68:02:21.4	800.0"
7	5:17:01.8	-67:20:33.9	240.0"	64	5:01:45.3	-70:39:12.1	620.0"	121	5:07:11.1	-68:26:15.5	600.0"
8	4:52:41.7	-67:18:11.2	402.8"	65	5:27:33.7	-71:25:40.4	350.0"	122	5:56:08.7	-68:15:41.4	733.3"
9	5:32:10.5	-67:29:14.7	240.0"	66	5:03:32.2	-66:00:16.8	400.0"	123	5:24:26.7	-68:31:16.2	600.0"
10	5:04:59.6	-67:34:52.1	385.0"	67	5:35:36.2	-66:03:03.2	400.0"	124	5:27:59.7	-68:37:10.7	966.6"
11	5:17:57.1	-67:55:29.0	270.0"	68	5:34:21.0	-66:08:34.3	400.0"	125	5:31:58.7	-68:40:24.0	600.0"
12	5:24:18.3	-68:01:06.9	240.0"	69	4:58:52.3	-66:12:22.8	400.0"	126	5:14:11.0	-69:32:09.2	700.0"
13	5:22:50.7	-68:04:03.0	385.0"	70	5:37:04.3	-66:21:24.8	400.0"	127	4:53:57.1	-70:00:55.3	900.0"
14	5:06:49.9	-68:10:29.4	240.0"	71	5:45:40.8	-66:20:44.0	500.0"	128	5:28:57.1	-70:17:57.0	700.0"
15	5:49:33.6	-68:12:40.0	240.0"	72	5:37:33.8	-66:27:11.5	400.0"	129	5:50:00.1	-70:07:46.0	733.3"
16	5:03:19.8	-68:27:24.6	270.0"	73	5:35:09.1	-66:35:15.7	400.0"	130	5:21:38.0	-71:19:07.9	700.0"
17	5:10:24.9	-68:30:20.4	385.0"	74	5:02:12.5	-66:40:48.0	400.0"	131	5:22:17.1	-71:24:02.1	1000.0"
18	4:55:38.3	-68:26:11.7	313.3"	75	5:03:31.7	-66:43:46.6	400.0"	132	5:26:33.8	-71:35:05.9	840.0"
19	4:49:15.0	-68:24:33.8	270.0"	76	5:42:27.1	-66:39:38.8	400.0"	133	5:20:43.5	-65:29:25.9	1100.0
20	5:25:40.0	-69:04:35.4	240.0"	77	5:02:55.9	-67:00:34.8	400.0"	134	5:39:57.8	-66:08:47.8	900.0"
21	5:02:24.5	-69:04:31.4	313.3"	78	5:26:11.9	-67:09:57.6	400.0"	135	4:58:52.8	-66:13:53.1	800.0"
22	5:27:46.7	-69:12:31.5	240.0"	79	5:26:56.3	-67:18:18.7	400.0"	136	5:31:50.1	-66:18:59.3	800.0"
23	4:49:01.6	-69:10:26.3	240.0"	80	5:32:00.3	-67:23:47.7	500.0"	137	5:35:49.6	-66:19:27.9	800.0"
24	4:49:25.5	-69:12:21.8	240.0"	81	5:36:51.1	-67:27:37.2	600.0"	138	4:53:36.6	-66:42:11.5	800.0"
25	4:52:19.0	-69:21:26.4	313.3"	82	4:52:42.3	-68:01:58.2	400.0"	139	5:04:22.5	-67:16:31.4	1000.0
26	5:42:58.3	-69:40:52.0	385.0"	83	4:53:23.7	-68:03:22.0	400.0"	140	5:46:48.3	-67:10:32.1	800.0"
27	5:47:18.3	-69:42:24.7	240.0"	84	5:06:46.7	-68:09:38.6	500.0"	141	5:25:52.6	-67:29:31.2	1000.0"
28	5:43:18.0	-69:45:58.5	313.3"	85	5:09:40.4	-68:29:57.5	400.0"	142	5:28:20.9	-67:40:46.9	1000.0"
29	5:41:39.3	-70:00:22.8	313.3"	86	4:54:44.3	-68:23:20.2	600.0"	143	4:50:08.6	-67:40:38.9	1000.0"
30	5:01:57.3	-70:05:35.6	270.0"	87	5:06:24.5	-68:28:43.9	400.0"	144	5:09:51.5	-67:54:08.7	1000.0"
31	5:40:57.5	-70:03:17.2	313.3"	88	5:27:31.3	-68:32:43.3	400.0"	145	4:59:46.6	-67:56:27.1	800.0"
32	5:30:48.8	-70:07:32.5	313.3"	89	5:50:38.0	-68:24:48.8	400.0"	146	4:53:09.7	-68:03:04.1	900.0"
33	5:22:43.4	-70:09:23.3	270.0"	90	5:27:02.3	-68:42:19.7	400.0"	147	4:58:04.8	-68:27:48.0	800.0"
34	5:39:25.3	-70:12:44.9	240.0"	91	4:55:45.6	-68:39:44.9	400.0"	148	5:08:30.3	-68:45:14.2	800.0"
35	5:38:22.5	-70:42:18.0	347.5"	92	5:29:42.6	-69:04:14.0	400.0"	149	4:55:39.9	-69:14:49.3	800.0"
36	5:04:30.9	-70:44:41.0	385.0"	93	5:29:22.5	-69:08:49.3	400.0"	150	5:18:59.7	-69:42:59.4	1000.0"
37	5:08:00.8	-70:52:43.3	270.0"	94	5:13:24.1	-69:11:56.7	533.3"	151	5:18:39.5	-69:52:12.7	800.0"
38	5:07:42.2	-71:11:05.7	385.0"	95	5:13:47.9	-69:18:32.3	400.0"	152	5:42:28.9	-69:50:52.3	800.0"
39	5:17:49.9	-71:15:41.2	385.0"	96	4:50:00.7	-69:12:08.4	550.0"	153	4:59:45.6	-70:12:43.9	800.0"
40	5:42:42.5	-71:17:16.0	270.0"	97	5:31:32.4	-69:18:44.8	400.0"	154	5:06:17.0	-70:52:45.5	800.0"
41	5:41:46.7	-71:20:42.3	356.0"	98	4:58:08.9	-69:16:57.7	400.0"	155	5:30:56.2	-71:02:51.8	1050.0"
42	5:09:56.9	-71:28:00.9	270.0"	99	4:57:29.5	-69:16:40.5	400.0"	156	5:27:30.2	-71:27:10.9	800.0"
43	5:24:37.6	-71:38:56.7	313.3"	100	5:40:13.8	-69:24:49.3	500.0"	157	5:22:40.6	-71:36:10.1	1000.0"
44	5:06:16.0	-65:42:07.1	433.3"	101	5:49:33.1	-69:19:58.3	400.0"	158	5:26:12.4	-67:11:27.5	1000.0"
45	5:27:58.6	-65:50:07.7	400.0"	102	4:51:41.5	-69:35:05.9	600.0"	159	5:32:08.4	-67:40:16.1	1100.0"
46	5:17:56.9	-66:01:52.0	525.0"	103	5:40:03.8	-69:45:46.2	600.0"	160	5:06:29.6	-68:08:04.1	1000.0"
47	5:31:42.0	-66:22:12.0	300.0"	104	5:44:03.7	-69:49:01.1	400.0"	161	5:24:59.2	-68:30:21.3	1000.0"
48	5:15:13.7	-66:28:41.4	300.0"	105	5:49:05.3	-70:04:04.1	400.0"	162	5:42:21.7	-69:31:11.5	1000.0"
49	5:15:45.8	-66:42:22.5	300.0"	106	4:53:23.9	-70:36:44.6	600.0"	163	5:29:57.0	-71:00:01.7	1000.0"
50	5:12:54.7	-67:02:40.1	433.3"	107	4:47:32.9	-70:34:09.0	400.0"	164	5:21:51.2	-67:55:23.9	1200.0"
51	4:53:12.5	-67:03:21.6	350.0"	108	5:06:38.0	-70:44:20.7	400.0"	165	5:14:14.0	-69:20:24.5	1200.0"
52	4:48:27.2	-67:00:08.5	300.0"	109	5:07:54.0	-71:02:06.3	400.0"	166	5:07:19.7	-71:12:38.3	1200.0"
53	5:18:53.4	-67:19:09.0	350.0"	110	5:36:31.2	-66:01:49.0	600.0"	167	5:44:24.5	-66:21:53.9	1400.0"
54	5:31:43.7	-67:35:33.8	350.0"	111	5:00:06.7	-66:17:06.2	600.0"	168	5:49:31.6	-70:07:08.0	1400.0"
55	4:52:22.0	-68:24:57.7	350.0"	112	5:38:16.7	-66:18:25.3	700.0"	169	5:28:10.7	-70:40:16.6	1400.0"
56	5:38:45.6	-68:37:36.8	300.0"	113	5:32:32.9	-66:26:44.7	900.0"				

Table A.3: Combined bubbles detected in the LMC OIII image. Size refers to the size of the surrounding square and is mostly slightly larger than the bubble itself.

Nr	RA	DEC	Size	Nr	RA	DEC	Size
0	5:28:00.1	-65:49:52.4	385.0"	50	4:54:37.1	-69:10:07.1	300.0"
1	5:17:59.0	-66:01:54.5	270.0"	51	5:26:02.7	-69:15:41.7	300.0"
2	5:35:40.9	-66:03:05.2	468.0"	52	5:13:50.2	-69:18:52.5	525.0"
3	5:00:17.5	-66:05:50.6	313.3"	53	4:52:16.8	-69:21:25.2	350.0"
4	5:00:13.0	-66:16:02.2	313.3"	54	4:47:33.3	-69:19:42.7	300.0"
5	5:37:27.0	-66:18:39.1	270.0"	55	4:54:11.6	-70:01:05.1	300.0"
6	5:25:00.7	-66:26:21.7	240.0"	56	5:32:39.7	-66:28:17.3	500.0"
7	4:58:17.3	-66:21:46.9	313.3"	57	4:56:56.6	-66:25:57.7	400.0"
8	5:32:17.1	-66:25:30.1	240.0"	58	4:55:29.6	-67:08:56.3	700.0"
9	5:32:35.7	-66:28:43.7	240.0"	59	5:25:30.2	-67:32:01.9	600.0"
10	4:57:51.7	-66:27:57.7	335.0"	60	5:26:42.9	-67:38:21.7	400.0"
11	5:20:37.8	-66:46:45.9	270.0"	61	5:43:28.3	-67:51:14.2	733.3"
12	5:20:26.2	-66:54:07.9	313.3"	62	5:05:02.4	-68:03:02.2	700.0"
13	5:10:32.4	-67:09:40.7	270.0"	63	5:50:39.5	-68:25:48.2	400.0"
14	4:53:40.6	-67:03:32.9	270.0"	64	4:55:51.6	-68:39:17.7	400.0"
15	5:16:58.4	-67:20:13.8	240.0"	65	5:18:30.8	-69:15:13.6	400.0"
16	4:52:42.2	-67:18:12.2	385.0"	66	5:19:50.8	-69:26:41.4	400.0"
17	5:04:57.7	-67:34:16.5	240.0"	67	5:42:56.2	-69:41:05.7	400.0"
18	5:36:11.6	-67:34:25.0	240.0"	68	5:29:43.3	-70:59:20.1	500.0"
19	5:33:16.3	-67:42:53.4	313.3"	69	5:22:45.2	-71:36:17.7	800.0"
20	5:23:19.0	-67:56:21.4	313.3"	70	5:20:39.8	-65:29:04.7	1000.0"
21	5:22:53.5	-68:04:32.7	270.0"	71	5:34:21.6	-66:14:34.1	760.0"
22	5:05:22.0	-68:06:05.5	313.3"	72	5:04:04.2	-67:16:18.8	800.0"
23	5:21:39.5	-68:11:04.9	240.0"	73	5:46:50.2	-67:10:00.6	700.0"
24	5:56:04.1	-68:14:12.0	385.0"	74	5:22:16.7	-67:58:31.5	700.0"
25	5:10:22.1	-68:30:30.0	270.0"	75	5:06:47.5	-68:27:07.7	840.0"
26	5:22:28.1	-68:39:20.7	240.0"	76	5:29:16.8	-68:28:38.7	600.0"
27	5:26:38.2	-69:19:45.4	240.0"	77	5:24:32.1	-68:31:00.4	700.0"
28	4:49:56.3	-69:12:35.8	385.0"	78	5:40:12.7	-69:24:44.7	600.0"
29	5:13:54.6	-69:23:02.9	240.0"	79	5:32:47.5	-69:30:32.7	700.0"
30	5:40:02.4	-69:45:48.6	385.0"	80	5:19:04.2	-69:43:55.8	800.0"
31	5:43:18.5	-69:46:07.5	385.0"	81	4:53:57.5	-70:00:51.3	800.0"
32	5:40:50.3	-70:02:40.6	313.3"	82	5:26:30.1	-71:33:20.8	600.0"
33	5:00:00.5	-70:08:22.5	313.3"	83	4:56:08.8	-66:19:32.4	800.0"
34	5:34:25.0	-70:33:51.1	313.3"	84	5:25:58.5	-67:11:00.1	900.0"
35	4:53:27.1	-70:36:32.1	310.0"	85	5:14:05.4	-67:20:03.9	800.0"
36	5:06:32.6	-70:43:09.5	313.3"	86	5:35:22.1	-67:33:45.2	800.0"
37	5:38:27.8	-70:41:49.9	313.3"	87	4:59:56.7	-67:57:11.3	900.0"
38	5:04:30.6	-70:44:28.4	313.3"	88	5:27:50.3	-68:51:10.0	900.0"
39	5:40:18.0	-71:11:03.2	270.0"	89	5:09:45.8	-68:54:59.2	900.0"
40	5:17:50.4	-71:15:52.9	313.3"	90	5:42:51.8	-69:40:37.9	800.0"
41	5:41:42.1	-71:20:23.8	373.3"	91	5:49:55.4	-70:08:32.7	800.0"
42	5:06:13.6	-65:42:14.7	525.0"	92	5:31:25.2	-71:03:19.0	800.0"
43	4:58:49.3	-66:12:01.4	350.0"	93	5:24:50.3	-66:25:03.5	1000.0"
44	5:37:11.9	-66:21:16.3	583.3"	94	5:28:08.2	-70:39:07.2	1000.0"
45	5:36:48.3	-67:26:43.3	350.0"	95	5:26:42.3	-71:32:28.8	1200.0"
46	5:10:30.3	-67:54:45.6	300.0"	96	5:13:35.9	-69:22:01.2	1200.0"
47	4:53:17.2	-68:03:04.3	620.0"	97	5:49:25.3	-70:06:52.1	1200.0"
48	4:57:27.3	-68:24:58.5	620.0"	98	5:28:10.7	-70:40:16.6	1400.0"
49	5:09:58.8	-68:55:01.5	300.0"	99	5:29:52.0	-71:01:52.9	1400.0"

A.2 SMC

Table A.4: Combined bubbles detected in the SMC H α image (non-optimized). Size refers to the size of the surrounding square and is mostly slightly larger than the bubble itself.

Nr	RA	DEC	Size	Nr	RA	DEC	Size	Nr	RA	DEC	Size
0	1:08:37.6	-70:40:16.2	188.0"	51	0:37:16.3	-73:00:09.6	144.0"	102	0:47:32.6	-73:05:22.3	180.0"
1	1:24:15.2	-70:40:45.8	162.0"	52	1:21:21.0	-73:02:15.3	188.0"	103	1:14:45.8	-73:06:48.1	180.0"
2	0:57:56.5	-70:52:37.3	162.0"	53	0:46:33.4	-73:06:34.4	188.0"	104	1:14:14.6	-73:12:32.9	180.0"
3	1:13:18.2	-70:53:15.2	188.0"	54	0:49:04.9	-73:08:36.1	177.0"	105	1:11:56.6	-73:13:29.7	180.0"
4	1:05:29.1	-70:56:24.4	144.0"	55	1:06:43.9	-73:10:44.4	188.0"	106	0:45:02.7	-73:13:09.8	180.0"
5	1:27:52.4	-70:51:36.1	188.0"	56	1:09:17.7	-73:12:06.2	144.0"	107	0:45:09.4	-73:14:59.8	180.0"
6	0:57:23.6	-71:10:22.8	162.0"	57	0:44:57.8	-73:10:47.2	162.0"	108	1:14:03.4	-73:15:48.2	180.0"
7	0:50:53.4	-71:09:52.9	193.7"	58	0:38:39.7	-73:08:46.3	220.8"	109	0:47:48.8	-73:17:38.9	180.0"
8	0:39:42.0	-71:06:38.1	188.0"	59	1:08:58.7	-73:12:45.3	144.0"	110	0:48:16.0	-73:18:32.8	180.0"
9	0:44:36.0	-71:10:29.6	188.0"	60	1:24:16.2	-73:09:44.6	144.0"	111	1:19:08.7	-73:17:29.0	180.0"
10	1:09:19.3	-71:24:22.7	162.0"	61	1:17:06.8	-73:12:41.1	162.0"	112	0:50:37.2	-73:20:23.8	180.0"
11	1:01:37.1	-71:33:23.4	188.0"	62	0:48:13.1	-73:14:37.9	144.0"	113	1:27:57.8	-73:16:20.2	180.0"
12	1:01:00.5	-71:35:43.4	162.0"	63	0:48:29.5	-73:16:25.5	168.0"	114	0:46:17.4	-73:23:54.2	180.0"
13	1:00:26.4	-71:37:19.8	162.0"	64	1:14:15.8	-73:15:51.7	209.3"	115	1:23:26.0	-73:22:45.2	426.7"
14	1:01:47.8	-71:39:48.0	162.0"	65	0:54:15.9	-73:17:35.4	144.0"	116	1:24:20.2	-73:22:28.6	180.0"
15	1:05:09.3	-71:44:29.7	231.0"	66	0:48:04.6	-73:17:28.8	177.0"	117	1:20:01.7	-73:31:49.2	180.0"
16	0:58:32.9	-71:44:57.5	177.6"	67	1:30:18.9	-73:10:41.7	188.0"	118	0:40:59.1	-73:37:35.4	180.0"
17	1:01:33.2	-71:47:59.3	168.0"	68	0:35:47.2	-73:13:51.8	186.0"	119	0:50:54.1	-73:46:27.7	180.0"
18	1:00:16.8	-71:48:30.6	188.0"	69	1:13:57.7	-73:17:43.8	299.0"	120	0:35:43.2	-73:53:14.9	180.0"
19	1:27:44.1	-71:42:25.8	231.0"	70	1:12:37.2	-73:17:48.1	162.0"	121	0:45:00.0	-74:01:02.4	180.0"
20	1:08:43.5	-71:50:29.4	162.0"	71	1:13:35.2	-73:18:29.1	184.8"	122	0:41:36.6	-74:11:05.1	180.0"
21	1:01:38.6	-71:51:23.1	188.0"	72	1:09:45.7	-73:19:03.7	188.0"	123	1:13:25.0	-74:17:14.9	180.0"
22	1:02:50.9	-71:53:35.9	144.0"	73	1:14:44.7	-73:18:31.7	144.0"	124	1:05:29.7	-70:56:21.3	300.0"
23	1:03:09.0	-71:53:55.9	162.0"	74	0:48:15.0	-73:20:02.7	188.0"	125	0:52:07.0	-71:51:18.5	360.0"
24	0:57:21.2	-71:55:12.6	144.0"	75	1:24:05.5	-73:18:03.7	144.0"	126	1:15:12.3	-72:19:47.3	240.0"
25	1:08:37.8	-71:58:48.0	172.8"	76	0:43:08.2	-73:20:53.0	162.0"	127	1:24:18.9	-73:09:43.4	240.0"
26	1:08:44.2	-72:00:08.5	144.0"	77	1:33:32.1	-73:14:07.9	144.0"	128	1:25:25.2	-73:23:42.0	240.0"
27	1:03:49.0	-72:03:59.2	186.0"	78	0:45:23.7	-73:23:02.1	184.8"	129	1:29:57.2	-73:36:41.8	300.0"
28	1:06:21.0	-72:05:41.4	144.0"	79	1:04:02.1	-73:28:14.5	188.0"	130	0:38:21.8	-73:58:10.4	300.0"
29	1:11:37.9	-72:10:13.5	172.8"	80	0:46:39.2	-73:32:07.7	250.5"	131	1:08:33.3	-71:56:10.3	600.1"
30	1:12:18.0	-72:15:44.4	177.0"	81	0:57:07.6	-73:34:10.9	188.0"	132	1:09:27.7	-72:01:46.0	420.0"
31	0:55:40.6	-72:17:32.9	162.0"	82	1:29:44.6	-73:34:23.5	162.0"	133	1:11:30.7	-72:10:16.7	480.0"
32	0:56:20.0	-72:17:53.9	162.0"	83	0:43:40.3	-73:44:29.7	162.0"	134	1:19:37.2	-73:05:46.8	360.0"
33	1:15:19.4	-72:20:27.3	144.0"	84	0:42:30.4	-73:44:43.9	168.0"	135	1:11:33.9	-73:14:49.6	360.0"
34	0:59:17.4	-72:24:37.3	162.0"	85	0:53:46.6	-73:52:42.0	162.0"	136	0:40:56.1	-73:36:31.2	420.0"
35	1:11:24.5	-72:23:01.9	334.0"	86	0:31:44.7	-73:47:53.6	188.0"	137	0:58:17.8	-71:28:15.4	480.0"
36	0:50:07.4	-72:32:43.9	188.0"	87	1:12:14.0	-73:54:51.9	213.6"	138	1:08:12.0	-72:00:43.8	540.1"
37	0:46:34.0	-72:35:56.6	162.0"	88	0:38:21.7	-73:58:13.4	144.0"	139	1:07:12.1	-72:03:10.7	480.0"
38	1:08:10.2	-72:38:33.4	188.0"	89	0:44:10.4	-74:16:16.8	188.0"	140	1:03:32.3	-72:03:45.4	600.1"
39	0:58:21.7	-72:39:48.2	162.0"	90	0:55:01.8	-74:18:53.4	208.0"	141	0:50:08.7	-72:34:04.2	600.1"
40	0:58:00.3	-72:39:35.5	162.0"	91	0:53:13.2	-74:39:55.8	213.6"	142	0:50:35.5	-72:47:51.7	480.0"
41	0:58:24.3	-72:40:27.3	144.0"	92	1:34:36.9	-74:41:02.2	162.0"	143	0:44:31.0	-73:05:06.1	480.0"
42	1:03:59.0	-72:41:16.9	162.0"	93	0:35:50.5	-74:52:48.2	162.0"	144	1:16:54.8	-73:08:53.3	480.0"
43	1:20:19.2	-72:45:25.4	188.0"	94	0:33:30.5	-71:16:44.1	315.0"	145	1:14:05.1	-73:14:29.6	480.0"
44	0:49:46.2	-72:48:54.8	144.0"	95	0:59:47.7	-71:44:49.1	288.0"	146	1:19:11.7	-73:20:10.5	480.0"
45	0:51:02.5	-72:50:35.5	162.0"	96	1:05:09.1	-71:59:55.3	180.0"	147	1:07:06.8	-71:56:11.3	600.1"
46	1:13:26.4	-72:49:48.8	144.0"	97	1:11:25.1	-72:08:55.9	180.0"	148	0:50:37.9	-72:53:28.4	600.1"
47	1:06:59.1	-72:51:13.9	144.0"	98	1:11:05.4	-72:11:00.2	180.0"	149	1:09:13.4	-73:11:52.9	720.1"
48	0:48:38.3	-72:53:14.6	162.0"	99	1:11:17.4	-72:21:55.3	210.0"	150	1:11:33.0	-73:15:28.9	600.1"
49	1:10:02.8	-72:57:51.4	177.0"	100	0:50:26.0	-72:35:19.4	180.0"	151	1:25:21.1	-73:18:06.1	600.1"
50	0:42:15.5	-72:59:42.2	188.0"	101	1:01:03.0	-72:41:58.1	180.0"	152	1:25:17.6	-73:25:13.9	640.1"

Table A.5: Combined bubbles detected in the SMC H α image (more noise, lower thresholds), part 1 (Continued in Tab. A.6). Size refers to the size of the surrounding square and is mostly slightly larger than the bubble itself.

Nr	RA	DEC	Size	Nr	RA	DEC	Size	Nr	RA	DEC	Size
0	1:09:35.3	-70:38:59.5	144.0 ^a	48	1:12:17.1	-72:15:53.6	177.0 ^a	96	1:04:02.3	-73:28:28.0	177.0 ^a
1	1:08:38.0	-70:40:19.1	162.0 ^a	49	0:56:20.0	-72:17:59.9	162.0 ^a	97	1:23:33.7	-73:23:32.8	264.0 ^a
2	0:56:58.3	-70:42:11.1	162.0 ^a	50	0:39:03.5	-72:17:19.1	188.0 ^a	98	0:46:38.7	-73:31:59.3	246.9 ^a
3	1:24:16.7	-70:40:40.1	188.0 ^a	51	1:15:19.4	-72:20:27.3	144.0 ^a	99	0:57:10.0	-73:34:11.0	188.0 ^a
4	0:53:59.7	-70:48:42.2	162.0 ^a	52	0:59:17.4	-72:24:37.3	162.0 ^a	100	0:46:38.6	-73:32:42.2	144.0 ^a
5	1:03:18.0	-70:51:32.8	165.6 ^a	53	1:11:25.4	-72:23:24.7	264.0 ^a	101	1:17:36.2	-73:32:28.0	168.0 ^a
6	0:37:11.7	-70:47:01.7	144.0 ^a	54	1:24:03.7	-72:19:54.0	188.0 ^a	102	1:20:19.9	-73:32:48.9	144.0 ^a
7	0:57:58.9	-70:52:28.5	188.0 ^a	55	0:50:03.1	-72:33:13.6	253.5 ^a	103	1:10:14.3	-73:37:30.6	162.0 ^a
8	1:13:44.4	-70:52:31.5	186.0 ^a	56	0:46:33.1	-72:36:03.4	188.0 ^a	104	1:29:23.9	-73:34:03.5	183.0 ^a
9	1:13:17.0	-70:53:01.6	231.0 ^a	57	1:08:12.0	-72:38:39.1	144.0 ^a	105	1:21:50.6	-73:37:36.0	188.0 ^a
10	1:05:32.9	-70:56:37.2	220.8 ^a	58	0:58:00.3	-72:39:35.5	162.0 ^a	106	0:42:00.7	-73:41:14.1	144.0 ^a
11	1:27:53.3	-70:51:40.6	231.0 ^a	59	0:58:24.4	-72:40:19.3	168.0 ^a	107	1:19:14.3	-73:42:22.7	162.0 ^a
12	1:05:55.2	-71:01:42.1	162.0 ^a	60	1:04:05.8	-72:41:19.4	144.0 ^a	108	0:43:37.4	-73:44:31.9	144.0 ^a
13	1:14:24.3	-71:02:46.0	162.0 ^a	61	1:20:20.0	-72:45:25.6	231.0 ^a	109	0:40:02.2	-73:46:01.4	188.0 ^a
14	1:31:44.7	-70:56:40.7	162.0 ^a	62	0:51:01.2	-72:50:35.2	162.0 ^a	110	0:56:19.4	-73:49:52.2	188.0 ^a
15	0:57:22.4	-71:10:25.7	144.0 ^a	63	1:13:26.4	-72:49:48.8	144.0 ^a	111	1:33:41.3	-73:42:52.5	177.0 ^a
16	0:50:50.6	-71:09:53.3	246.9 ^a	64	1:06:59.1	-72:51:13.9	144.0 ^a	112	0:53:43.7	-73:52:35.7	186.0 ^a
17	0:39:42.8	-71:06:38.4	188.0 ^a	65	1:26:40.3	-72:45:20.6	162.0 ^a	113	0:31:44.7	-73:47:53.6	188.0 ^a
18	1:19:00.6	-71:07:22.6	188.0 ^a	66	1:08:21.6	-72:53:26.3	144.0 ^a	114	0:29:30.2	-73:47:17.2	162.0 ^a
19	0:44:34.5	-71:10:25.1	231.0 ^a	67	0:36:15.5	-72:51:19.3	188.0 ^a	115	1:12:13.9	-73:55:10.1	264.0 ^a
20	0:58:18.2	-71:14:47.9	168.0 ^a	68	1:15:14.6	-72:56:39.0	188.0 ^a	116	0:35:48.1	-73:53:09.4	231.0 ^a
21	0:33:23.6	-71:16:35.3	280.8 ^a	69	1:10:05.5	-72:57:46.4	231.0 ^a	117	0:38:20.4	-73:58:06.9	258.0 ^a
22	1:09:19.3	-71:24:22.7	162.0 ^a	70	1:08:12.6	-73:01:05.5	186.0 ^a	118	0:38:29.1	-74:00:00.6	188.0 ^a
23	1:01:34.2	-71:33:43.6	188.0 ^a	71	1:11:15.4	-73:01:19.5	144.0 ^a	119	1:18:04.0	-74:09:36.9	188.0 ^a
24	1:00:25.1	-71:37:18.8	188.0 ^a	72	0:42:15.5	-72:59:42.2	188.0 ^a	120	0:41:39.6	-74:11:02.0	188.0 ^a
25	1:01:47.8	-71:39:48.0	162.0 ^a	73	0:37:16.3	-73:00:09.6	144.0 ^a	121	0:31:07.5	-74:10:31.9	186.0 ^a
26	0:41:03.2	-71:37:31.1	162.0 ^a	74	0:53:44.0	-73:05:55.6	144.0 ^a	122	0:44:09.6	-74:16:22.1	231.0 ^a
27	1:05:15.6	-71:41:45.6	162.0 ^a	75	0:45:29.0	-73:05:14.9	194.0 ^a	123	1:13:25.7	-74:16:59.2	184.8 ^a
28	1:05:09.5	-71:44:40.8	280.8 ^a	76	0:46:29.5	-73:06:30.3	196.8 ^a	124	0:55:03.9	-74:19:03.8	286.3 ^a
29	0:58:32.0	-71:44:55.5	188.0 ^a	77	0:49:01.5	-73:08:26.4	231.0 ^a	125	0:53:48.7	-74:20:25.5	168.0 ^a
30	1:01:33.2	-71:48:03.3	144.0 ^a	78	1:06:43.9	-73:10:40.4	188.0 ^a	126	0:25:24.7	-74:24:47.3	188.0 ^a
31	1:00:16.8	-71:48:30.6	188.0 ^a	79	0:38:42.1	-73:08:40.0	231.0 ^a	127	1:14:15.6	-74:38:18.5	188.0 ^a
32	0:46:25.9	-71:47:15.4	188.0 ^a	80	1:24:12.6	-73:09:55.2	186.0 ^a	128	1:31:30.8	-74:37:17.6	171.0 ^a
33	1:27:41.9	-71:42:39.1	231.0 ^a	81	1:17:06.9	-73:12:47.1	162.0 ^a	129	1:13:10.9	-74:47:13.7	144.0 ^a
34	1:08:46.9	-71:50:05.4	184.8 ^a	82	0:49:58.9	-73:16:37.9	162.0 ^a	130	1:34:38.5	-74:40:55.2	177.0 ^a
35	1:21:32.1	-71:46:55.3	162.0 ^a	83	1:14:24.6	-73:15:56.7	176.0 ^a	131	1:35:07.2	-74:55:58.8	162.0 ^a
36	1:01:37.8	-71:51:23.1	188.0 ^a	84	0:54:16.0	-73:17:32.4	162.0 ^a	132	1:36:22.1	-74:55:26.6	162.0 ^a
37	1:19:49.4	-71:48:33.9	188.0 ^a	85	0:48:03.2	-73:17:17.0	208.0 ^a	133	0:50:21.0	-70:40:34.7	180.0 ^a
38	0:52:07.4	-71:51:39.4	280.8 ^a	86	0:37:18.0	-73:13:25.7	280.8 ^a	134	0:53:36.8	-70:48:04.4	180.0 ^a
39	1:03:09.0	-71:53:58.9	144.0 ^a	87	1:30:19.8	-73:10:41.2	188.0 ^a	135	1:03:03.8	-70:51:07.3	180.0 ^a
40	1:08:23.6	-71:55:23.2	278.4 ^a	88	0:35:52.1	-73:13:52.5	234.0 ^a	136	1:01:19.0	-70:51:12.0	180.0 ^a
41	1:08:32.0	-71:59:03.7	183.4 ^a	89	1:13:59.7	-73:18:03.3	168.0 ^a	137	0:52:34.8	-70:51:15.5	180.0 ^a
42	1:08:44.2	-72:00:08.5	144.0 ^a	90	1:09:46.5	-73:18:59.6	188.0 ^a	138	0:57:56.3	-70:54:34.2	180.0 ^a
43	0:27:36.2	-71:53:27.4	177.6 ^a	91	0:48:13.6	-73:20:03.9	186.0 ^a	139	0:50:19.1	-70:54:15.9	180.0 ^a
44	1:06:20.6	-72:05:39.5	188.0 ^a	92	1:27:56.5	-73:16:23.9	162.0 ^a	140	1:03:02.5	-70:58:30.9	180.0 ^a
45	0:49:50.7	-72:07:53.5	144.0 ^a	93	0:43:09.2	-73:20:48.3	188.0 ^a	141	0:50:39.7	-71:07:31.6	180.0 ^a
46	1:11:33.1	-72:10:01.3	225.8 ^a	94	0:45:25.6	-73:22:59.0	186.0 ^a	142	0:50:30.5	-71:11:09.8	180.0 ^a
47	1:13:18.4	-72:12:08.4	162.0 ^a	95	1:24:14.5	-73:22:25.0	186.0 ^a	143	0:41:17.1	-71:13:18.0	180.0 ^a

Table A.6: Combined bubbles detected in the SMC H α image (more noise, lower thresholds), part 2 (Continuation of in Tab. A.5). Size refers to the size of the surrounding square and is mostly slightly larger than the bubble itself.

Nr	RA	DEC	Size	Nr	RA	DEC	Size	Nr	RA	DEC	Size
144	0:50:13.5	-71:30:02.6	180.0"	192	0:45:43.9	-73:06:56.0	180.0"	240	0:57:06.0	-73:32:24.8	180.0"
145	1:01:01.8	-71:35:46.3	180.0"	193	1:27:30.1	-73:03:50.5	210.0"	241	1:34:25.8	-73:22:45.9	180.0"
146	0:56:20.4	-71:36:51.1	180.0"	194	1:18:02.6	-73:07:37.6	180.0"	242	1:24:24.3	-73:29:16.8	180.0"
147	0:59:37.8	-71:44:21.5	288.0"	195	0:45:50.7	-73:08:45.9	180.0"	243	0:40:06.7	-73:34:25.7	210.0"
148	1:13:25.0	-71:47:13.8	180.0"	196	1:08:58.6	-73:11:49.3	200.0"	244	0:41:02.2	-73:36:32.2	260.0"
149	1:05:22.1	-71:51:17.9	180.0"	197	1:09:14.9	-73:12:00.6	180.0"	245	0:40:33.0	-73:38:02.6	180.0"
150	1:02:22.5	-71:52:25.4	180.0"	198	1:12:06.9	-73:12:15.4	180.0"	246	1:29:02.1	-73:34:30.7	180.0"
151	1:08:00.0	-71:53:57.5	180.0"	199	1:15:35.7	-73:11:44.0	210.0"	247	1:29:51.7	-73:35:11.1	180.0"
152	1:09:04.7	-71:54:22.9	180.0"	200	1:08:34.0	-73:13:19.3	180.0"	248	1:15:04.4	-73:40:59.1	180.0"
153	1:07:36.2	-71:58:07.2	190.0"	201	1:14:20.7	-73:13:07.5	210.0"	249	1:29:29.4	-73:36:01.2	180.0"
154	1:07:16.2	-71:59:16.1	180.0"	202	0:46:26.1	-73:12:55.3	180.0"	250	1:29:57.5	-73:36:50.7	180.0"
155	1:08:02.3	-71:59:09.3	220.0"	203	1:11:44.0	-73:14:08.5	288.0"	251	1:19:51.9	-73:42:09.7	210.0"
156	1:07:51.8	-72:00:16.9	210.0"	204	0:45:35.3	-73:12:54.4	200.0"	252	0:50:52.3	-73:45:51.4	210.0"
157	1:07:20.9	-72:00:45.4	210.0"	205	1:09:54.9	-73:14:05.8	180.0"	253	1:18:30.5	-73:44:10.5	180.0"
158	1:06:58.1	-72:00:36.6	180.0"	206	1:14:54.4	-73:14:03.1	187.5"	254	0:42:34.2	-73:44:43.1	180.0"
159	1:08:23.9	-72:01:10.9	200.0"	207	0:47:53.5	-73:14:51.7	180.0"	255	1:30:11.4	-73:40:39.0	180.0"
160	0:55:28.9	-72:01:10.8	180.0"	208	1:14:22.0	-73:14:43.3	180.0"	256	1:13:40.7	-73:50:15.1	180.0"
161	1:07:56.9	-72:01:34.2	180.0"	209	0:41:47.8	-73:13:35.4	180.0"	257	0:44:17.7	-73:50:25.9	210.0"
162	1:03:36.4	-72:02:15.1	180.0"	210	1:24:21.3	-73:11:24.9	180.0"	258	1:14:03.4	-73:51:39.7	180.0"
163	1:25:10.7	-72:03:37.4	195.0"	211	1:15:10.9	-73:15:00.3	180.0"	259	0:44:57.3	-73:54:25.0	180.0"
164	1:11:11.7	-72:08:22.7	180.0"	212	1:13:58.5	-73:15:46.4	210.0"	260	0:44:49.9	-73:56:11.2	180.0"
165	1:11:05.8	-72:10:36.1	210.0"	213	1:09:42.7	-73:17:02.1	200.0"	261	1:02:34.9	-73:59:31.8	180.0"
166	1:11:19.7	-72:21:23.8	200.0"	214	1:21:10.8	-73:14:35.1	210.0"	262	0:45:01.6	-73:59:14.6	180.0"
167	1:02:58.6	-72:25:17.6	180.0"	215	1:32:51.5	-73:08:59.5	180.0"	263	1:33:30.5	-73:51:59.3	180.0"
168	1:05:36.5	-72:30:28.9	180.0"	216	1:19:06.7	-73:15:41.4	180.0"	264	0:27:21.8	-74:12:44.0	180.0"
169	1:05:15.6	-72:31:43.1	180.0"	217	1:12:35.8	-73:17:45.4	180.0"	265	0:30:34.1	-74:18:48.5	180.0"
170	0:50:26.3	-72:35:11.5	190.0"	218	1:14:26.6	-73:18:34.5	180.0"	266	0:55:00.6	-70:43:22.4	240.0"
171	0:52:36.6	-72:36:40.1	180.0"	219	1:18:45.5	-73:16:36.8	180.0"	267	1:08:28.3	-71:53:41.0	240.0"
172	0:50:41.5	-72:36:22.2	180.0"	220	1:13:37.9	-73:18:23.6	288.0"	268	1:07:01.2	-71:58:24.1	240.0"
173	1:09:08.5	-72:39:00.0	180.0"	221	1:14:47.3	-73:17:30.9	210.0"	269	0:52:01.2	-72:16:52.3	240.0"
174	1:10:54.7	-72:40:13.3	210.0"	222	0:48:15.9	-73:18:44.8	180.0"	270	1:15:34.4	-72:17:52.7	240.0"
175	1:01:02.9	-72:41:46.1	180.0"	223	1:21:38.8	-73:16:57.8	180.0"	271	0:50:18.7	-72:53:49.1	240.0"
176	1:12:21.4	-72:42:09.7	180.0"	224	0:50:37.1	-73:20:35.7	180.0"	272	0:37:18.0	-72:59:52.2	240.0"
177	1:12:37.0	-72:43:50.2	200.0"	225	1:14:05.5	-73:20:00.1	180.0"	273	1:19:34.2	-73:05:57.9	360.0"
178	1:12:18.1	-72:45:10.7	180.0"	226	1:23:52.4	-73:18:39.5	180.0"	274	0:45:18.7	-73:15:32.3	240.0"
179	0:49:39.9	-72:48:05.6	195.0"	227	0:47:31.3	-73:22:35.4	180.0"	275	1:13:01.9	-73:26:28.2	240.0"
180	0:50:26.8	-72:48:56.3	180.0"	228	1:23:42.7	-73:19:44.0	210.0"	276	1:12:24.1	-73:26:36.8	240.0"
181	1:14:03.1	-72:49:48.5	210.0"	229	1:07:35.3	-73:24:52.3	180.0"	277	0:44:55.8	-74:00:49.3	240.0"
182	1:10:58.2	-72:51:28.3	180.0"	230	1:15:19.8	-73:23:28.8	180.0"	278	1:09:26.2	-72:02:07.3	440.0"
183	0:49:14.8	-72:51:30.9	180.0"	231	1:02:13.0	-73:25:32.6	180.0"	279	1:07:50.2	-72:01:17.2	480.0"
184	0:50:00.6	-72:52:03.7	180.0"	232	1:23:27.1	-73:22:07.7	195.0"	280	1:03:34.0	-72:03:33.3	480.0"
185	0:50:40.9	-72:54:17.0	210.0"	233	1:20:47.6	-73:24:12.9	180.0"	281	0:50:43.9	-72:47:17.2	480.0"
186	1:23:43.1	-72:57:16.5	210.0"	234	1:24:52.5	-73:23:26.6	180.0"	282	0:37:20.6	-72:58:59.1	480.0"
187	1:21:26.8	-73:00:34.7	180.0"	235	1:21:38.0	-73:25:12.0	180.0"	283	1:08:14.6	-71:57:49.3	840.1"
188	0:45:21.5	-73:04:01.8	180.0"	236	1:25:18.4	-73:23:51.1	180.0"	284	1:08:16.6	-72:02:13.1	840.1"
189	1:21:21.2	-73:02:13.3	210.0"	237	1:12:38.2	-73:28:33.8	180.0"	285	0:37:05.9	-72:59:41.1	840.1"
190	0:47:32.6	-73:05:22.3	180.0"	238	1:25:59.5	-73:24:56.6	180.0"	286	1:09:20.1	-73:11:23.7	840.1"
191	0:46:08.8	-73:06:50.3	180.0"	239	1:20:42.3	-73:27:57.7	180.0"				

Table A.7: Combined bubbles detected in the SMC SII image (non-optimized). Size refers to the size of the surrounding square and is mostly slightly larger than the bubble itself.

Nr	RA	DEC	Size	Nr	RA	DEC	Size
0	1:01:01.8	-71:35:52.3	144.0"	50	0:48:52.2	-72:05:23.4	180.0"
1	1:00:24.2	-71:37:16.8	186.0"	51	0:59:03.6	-72:08:22.1	180.0"
2	1:01:47.8	-71:39:51.0	144.0"	52	1:11:35.1	-72:10:20.8	210.0"
3	0:58:34.2	-71:45:03.6	144.0"	53	1:11:02.7	-72:10:48.8	180.0"
4	1:01:33.2	-71:48:00.3	162.0"	54	1:12:19.3	-72:15:44.1	210.0"
5	1:00:18.1	-71:48:30.6	188.0"	55	1:03:13.9	-72:22:04.7	180.0"
6	1:02:53.5	-71:53:47.8	144.0"	56	1:11:17.9	-72:22:00.2	200.0"
7	1:03:31.9	-72:01:39.4	156.0"	57	1:02:55.9	-72:25:17.7	180.0"
8	1:08:01.0	-72:02:15.5	144.0"	58	0:50:27.9	-72:26:43.3	180.0"
9	1:06:21.0	-72:05:41.4	144.0"	59	0:52:52.1	-72:37:54.3	180.0"
10	1:03:21.3	-72:09:38.1	188.0"	60	1:02:37.7	-72:46:06.9	180.0"
11	1:06:34.5	-72:14:15.9	144.0"	61	0:50:13.4	-72:53:30.1	180.0"
12	1:03:07.8	-72:32:56.2	162.0"	62	0:45:56.8	-72:54:22.0	180.0"
13	0:50:03.5	-72:33:06.9	201.0"	63	0:52:57.7	-72:57:55.7	180.0"
14	0:58:00.2	-72:39:47.5	162.0"	64	0:37:44.4	-72:59:39.0	180.0"
15	1:03:55.2	-72:41:56.2	168.0"	65	0:47:27.1	-73:05:21.0	180.0"
16	1:09:52.2	-72:45:02.6	168.0"	66	0:45:14.8	-73:14:00.4	210.0"
17	0:42:15.5	-72:59:42.2	188.0"	67	1:14:00.6	-73:16:22.9	220.0"
18	0:37:16.9	-73:00:01.8	188.0"	68	0:46:50.4	-73:17:25.6	180.0"
19	0:49:05.4	-73:08:52.7	186.0"	69	1:14:36.4	-73:18:39.9	180.0"
20	0:47:37.9	-73:09:34.3	201.0"	70	0:55:47.0	-73:21:01.6	180.0"
21	1:09:17.6	-73:11:54.2	144.0"	71	0:46:46.1	-73:22:07.0	210.0"
22	1:08:57.2	-73:12:31.6	188.0"	72	1:17:27.0	-73:21:39.2	180.0"
23	0:48:17.1	-73:14:59.8	162.0"	73	1:23:23.2	-73:22:21.4	315.0"
24	1:14:15.7	-73:15:54.0	198.0"	74	1:26:05.0	-73:21:10.8	210.0"
25	0:49:43.3	-73:17:08.0	144.0"	75	1:29:04.7	-73:30:15.6	180.0"
26	0:48:02.5	-73:17:56.9	162.0"	76	0:41:09.2	-73:36:14.5	180.0"
27	1:14:02.0	-73:17:30.7	144.0"	77	1:28:56.1	-73:34:21.7	180.0"
28	1:13:25.3	-73:18:07.8	188.0"	78	0:50:51.5	-73:46:07.3	200.0"
29	1:09:48.8	-73:18:53.2	188.0"	79	0:45:05.8	-74:01:03.9	180.0"
30	0:48:24.2	-73:19:52.6	186.0"	80	1:00:21.2	-71:30:59.0	240.0"
31	0:48:15.0	-73:20:02.7	144.0"	81	0:52:00.5	-71:51:21.6	240.0"
32	0:43:06.8	-73:20:52.6	162.0"	82	1:08:32.9	-71:54:31.3	440.0"
33	1:24:15.3	-73:18:59.7	144.0"	83	1:08:59.7	-71:54:47.7	240.0"
34	0:45:23.6	-73:22:55.4	162.0"	84	1:07:52.7	-72:00:58.8	240.0"
35	1:23:40.4	-73:24:10.1	144.0"	85	1:17:04.6	-73:07:38.1	240.0"
36	1:25:25.9	-73:23:28.1	198.0"	86	0:53:03.2	-73:11:38.9	240.0"
37	0:49:24.8	-73:29:05.3	144.0"	87	1:27:07.4	-73:05:41.4	240.0"
38	0:57:10.9	-73:34:11.1	188.0"	88	1:17:10.2	-73:13:19.2	240.0"
39	0:40:06.4	-73:34:22.6	186.0"	89	1:24:50.5	-73:23:03.4	240.0"
40	1:29:18.7	-73:33:18.6	214.0"	90	0:49:29.1	-73:29:06.1	240.0"
41	1:29:21.5	-73:34:12.5	156.0"	91	0:46:01.8	-73:29:14.9	240.0"
42	0:31:43.4	-73:47:46.9	188.0"	92	1:24:50.3	-73:25:46.3	240.0"
43	0:59:38.0	-71:44:46.7	180.0"	93	1:29:51.9	-73:36:08.4	240.0"
44	1:01:36.1	-71:51:21.2	180.0"	94	0:40:58.0	-73:36:04.7	360.0"
45	0:52:14.6	-71:51:34.2	315.0"	95	0:47:30.1	-73:08:52.0	480.0"
46	1:08:33.0	-71:58:28.4	180.0"	96	1:13:34.7	-73:18:13.6	480.0"
47	1:08:35.8	-72:00:47.9	180.0"	97	1:08:13.3	-72:00:37.6	660.1"
48	1:03:39.2	-72:03:24.5	288.0"	98	1:25:41.1	-73:23:58.8	600.1"
49	0:52:13.2	-72:04:11.8	180.0"	99	1:25:22.6	-73:22:54.9	840.1"

Table A.8: Combined bubbles detected in the SMC SII image (less noise). Size refers to the size of the surrounding square and is mostly slightly larger than the bubble itself.

Nr	RA	DEC	Size	Nr	RA	DEC	Size
0	1:01:04.4	-71:36:04.3	144.0"	31	1:17:06.7	-73:12:32.2	180.0"
1	1:00:25.1	-71:37:13.8	162.0"	32	0:45:09.5	-73:13:13.6	220.0"
2	1:01:33.2	-71:48:00.3	162.0"	33	1:14:01.8	-73:15:54.6	195.0"
3	0:57:21.2	-71:55:12.6	144.0"	34	0:50:47.3	-73:17:13.3	180.0"
4	1:08:01.0	-72:02:15.5	144.0"	35	0:49:43.4	-73:17:02.0	180.0"
5	0:59:08.9	-72:08:04.1	144.0"	36	1:13:32.6	-73:18:11.1	315.0"
6	0:56:03.3	-72:16:10.7	162.0"	37	1:25:50.6	-73:22:48.0	180.0"
7	0:56:47.8	-72:24:43.8	162.0"	38	1:23:37.4	-73:23:59.4	180.0"
8	0:56:23.1	-72:28:57.3	144.0"	39	0:40:08.7	-73:34:29.5	180.0"
9	0:50:05.1	-72:32:49.5	168.0"	40	1:29:12.7	-73:32:24.4	180.0"
10	0:58:00.3	-72:39:38.5	144.0"	41	0:59:39.3	-71:44:28.7	240.0"
11	0:42:16.0	-72:59:39.4	162.0"	42	0:58:30.3	-71:44:45.5	240.0"
12	0:37:16.9	-73:00:01.8	188.0"	43	1:00:21.5	-71:48:40.6	240.0"
13	0:45:33.8	-73:10:44.8	162.0"	44	0:52:00.5	-71:51:21.6	240.0"
14	0:42:10.2	-73:13:24.7	144.0"	45	1:08:34.2	-71:54:43.1	420.0"
15	0:48:02.6	-73:17:47.9	144.0"	46	1:07:52.7	-72:00:58.8	240.0"
16	1:13:59.4	-73:17:43.4	144.0"	47	1:03:44.4	-72:03:32.5	240.0"
17	0:48:31.9	-73:19:54.2	144.0"	48	1:11:36.3	-72:10:11.5	240.0"
18	0:43:08.2	-73:20:54.0	188.0"	49	0:53:34.0	-72:33:17.4	240.0"
19	0:45:25.0	-73:22:55.8	162.0"	50	1:13:53.9	-73:17:50.8	240.0"
20	0:48:12.2	-73:24:05.4	162.0"	51	1:24:54.3	-73:22:43.6	240.0"
21	1:23:28.2	-73:22:16.8	258.0"	52	1:11:26.3	-72:22:26.5	420.0"
22	0:57:10.0	-73:34:10.0	162.0"	53	1:24:19.2	-73:09:55.3	360.0"
23	1:29:23.0	-73:33:48.7	217.7"	54	0:40:57.4	-73:36:34.6	360.0"
24	0:31:45.8	-73:48:03.3	162.0"	55	0:52:12.5	-71:50:29.4	540.1"
25	1:08:33.2	-71:58:46.3	180.0"	56	1:03:34.1	-72:04:09.2	480.0"
26	1:11:05.4	-72:11:00.2	180.0"	57	1:25:46.4	-73:23:44.3	630.1"
27	1:04:25.0	-72:15:35.5	180.0"	58	1:08:14.1	-72:00:25.5	720.1"
28	0:49:18.6	-72:22:41.9	180.0"	59	0:49:55.0	-72:33:19.6	600.1"
29	0:50:51.3	-72:43:24.2	180.0"	60	1:14:37.3	-73:13:09.1	720.1"
30	1:08:57.1	-73:12:21.6	210.0"				

Table A.9: Combined bubbles detected in the SMC OIII image (non-optimized). Size refers to the size of the surrounding square and is mostly slightly larger than the bubble itself.

Nr	RA	DEC	Size	Nr	RA	DEC	Size	Nr	RA	DEC	Size
0	0:50:53.1	-71:09:20.5	238.5 ^a	44	1:09:24.7	-73:12:21.4	380.8 ^a	88	1:06:33.3	-72:32:58.5	180.0 ^a
1	1:09:20.5	-71:24:22.5	162.0 ^a	45	1:24:11.2	-73:09:28.7	188.0 ^a	89	0:51:02.8	-72:34:01.7	180.0 ^a
2	1:01:11.7	-71:32:32.2	168.0 ^a	46	0:51:47.3	-73:14:04.6	144.0 ^a	90	0:50:51.7	-72:53:12.8	180.0 ^a
3	1:01:34.5	-71:33:00.6	162.0 ^a	47	0:45:40.3	-73:12:58.7	162.0 ^a	91	0:49:51.4	-72:54:02.1	180.0 ^a
4	0:59:41.4	-71:44:34.7	188.0 ^a	48	1:17:06.3	-73:12:38.3	188.0 ^a	92	0:37:22.4	-72:59:42.0	180.0 ^a
5	1:27:41.3	-71:42:57.4	162.0 ^a	49	0:48:22.1	-73:14:48.4	195.4 ^a	93	0:45:43.8	-73:03:43.6	180.0 ^a
6	1:01:36.1	-71:51:30.2	162.0 ^a	50	0:48:33.5	-73:16:08.1	162.0 ^a	94	0:49:30.0	-73:11:35.2	180.0 ^a
7	1:02:22.4	-71:52:05.4	168.0 ^a	51	0:54:18.8	-73:17:14.7	162.0 ^a	95	1:16:09.7	-73:11:01.1	180.0 ^a
8	1:03:09.0	-71:53:46.9	144.0 ^a	52	0:45:20.4	-73:15:38.8	188.0 ^a	96	0:46:23.2	-73:13:06.6	180.0 ^a
9	1:02:51.0	-71:53:47.9	144.0 ^a	53	0:48:03.3	-73:17:01.8	246.9 ^a	97	0:48:57.7	-73:14:29.1	180.0 ^a
10	0:57:21.2	-71:55:03.6	162.0 ^a	54	0:48:05.7	-73:18:34.9	164.6 ^a	98	0:49:53.9	-73:16:58.0	210.0 ^a
11	1:08:31.6	-72:00:54.6	168.0 ^a	55	1:13:49.5	-73:18:12.2	291.0 ^a	99	1:13:25.0	-73:16:33.7	180.0 ^a
12	1:11:28.4	-72:10:04.2	231.0 ^a	56	0:55:02.7	-73:19:39.9	144.0 ^a	100	0:48:23.5	-73:17:46.4	180.0 ^a
13	1:04:23.6	-72:15:32.6	162.0 ^a	57	1:14:54.9	-73:19:02.1	162.0 ^a	101	0:35:50.8	-73:14:19.0	180.0 ^a
14	0:52:01.5	-72:16:53.9	231.0 ^a	58	1:13:56.5	-73:19:17.3	162.0 ^a	102	1:13:31.0	-73:18:50.5	180.0 ^a
15	0:55:59.7	-72:20:19.5	144.0 ^a	59	0:50:40.9	-73:20:24.4	156.0 ^a	103	0:46:44.9	-73:31:49.6	180.0 ^a
16	1:11:25.7	-72:22:45.3	295.5 ^a	60	0:48:27.4	-73:19:58.1	220.8 ^a	104	0:41:15.1	-73:36:04.5	180.0 ^a
17	0:59:18.7	-72:24:40.3	144.0 ^a	61	0:48:13.7	-73:19:59.4	162.0 ^a	105	0:40:52.2	-73:36:08.8	180.0 ^a
18	1:24:07.4	-72:20:18.8	177.6 ^a	62	1:15:02.4	-73:19:39.1	144.0 ^a	106	0:48:17.4	-74:54:50.1	180.0 ^a
19	0:55:17.1	-72:27:04.1	144.0 ^a	63	0:46:45.5	-73:22:03.8	162.0 ^a	107	0:36:00.0	-74:53:37.2	180.0 ^a
20	0:56:07.4	-72:27:29.1	162.0 ^a	64	0:47:31.2	-73:22:39.4	188.0 ^a	108	0:58:31.4	-71:30:57.8	240.0 ^a
21	1:09:49.5	-72:30:34.3	144.0 ^a	65	0:45:28.1	-73:23:03.7	188.0 ^a	109	0:53:25.8	-72:23:04.1	240.0 ^a
22	0:52:57.0	-72:32:27.7	162.0 ^a	66	0:46:19.7	-73:24:00.8	188.0 ^a	110	1:05:45.2	-72:30:28.0	462.9 ^a
23	1:03:02.5	-72:33:11.5	144.0 ^a	67	1:16:11.9	-73:25:08.4	144.0 ^a	111	0:50:22.6	-72:52:08.7	540.1 ^a
24	0:49:27.0	-72:35:35.3	162.0 ^a	68	1:23:29.6	-73:22:25.0	196.8 ^a	112	0:51:00.9	-72:51:14.2	240.0 ^a
25	0:58:23.7	-72:40:03.3	177.0 ^a	69	0:49:27.5	-73:29:17.8	144.0 ^a	113	0:53:14.2	-72:53:57.7	240.0 ^a
26	0:57:58.5	-72:39:36.5	188.0 ^a	70	0:57:08.6	-73:34:11.0	188.0 ^a	114	0:46:32.5	-73:06:32.2	240.0 ^a
27	1:00:55.6	-72:42:02.8	177.0 ^a	71	0:46:48.8	-73:32:51.9	274.7 ^a	115	0:47:50.3	-73:09:36.6	360.0 ^a
28	0:53:59.3	-72:44:14.7	188.0 ^a	72	0:48:04.1	-73:35:40.6	162.0 ^a	116	1:24:51.3	-73:14:54.5	240.0 ^a
29	1:20:19.9	-72:45:36.1	162.0 ^a	73	0:40:08.8	-73:34:23.5	144.0 ^a	117	1:25:25.2	-73:23:42.0	240.0 ^a
30	0:50:29.2	-72:51:08.8	188.0 ^a	74	0:42:28.4	-73:44:44.3	162.0 ^a	118	1:24:56.0	-73:23:55.2	240.0 ^a
31	0:51:01.5	-72:53:32.4	188.0 ^a	75	0:31:44.4	-73:48:01.5	188.0 ^a	119	0:40:00.6	-73:34:08.5	300.0 ^a
32	0:53:18.3	-72:54:04.2	144.0 ^a	76	1:12:12.3	-73:55:20.5	162.0 ^a	120	0:53:10.0	-74:39:35.1	240.0 ^a
33	0:50:20.0	-72:53:58.3	162.0 ^a	77	0:48:31.5	-74:56:13.3	259.0 ^a	121	1:08:15.0	-72:00:55.3	600.1 ^a
34	0:55:06.7	-72:55:51.7	144.0 ^a	78	0:48:18.9	-74:56:56.4	144.0 ^a	122	1:06:55.4	-72:33:39.7	480.0 ^a
35	0:56:40.3	-72:56:52.8	165.6 ^a	79	1:27:50.0	-75:03:52.2	188.0 ^a	123	1:05:20.2	-72:34:00.7	360.0 ^a
36	1:10:05.8	-72:57:52.9	188.0 ^a	80	1:09:04.1	-71:53:10.9	180.0 ^a	124	0:50:38.2	-72:35:24.6	585.1 ^a
37	0:47:34.3	-73:05:28.7	188.0 ^a	81	1:08:43.6	-71:59:02.6	180.0 ^a	125	0:58:58.3	-72:11:08.8	600.1 ^a
38	0:45:30.0	-73:05:22.2	144.0 ^a	82	1:03:37.6	-72:04:02.0	430.0 ^a	126	0:51:04.6	-72:54:33.0	480.0 ^a
39	0:46:12.5	-73:05:42.1	162.0 ^a	83	1:03:05.9	-72:06:17.1	180.0 ^a	127	1:24:45.5	-73:09:55.6	660.1 ^a
40	0:46:33.8	-73:06:38.5	144.0 ^a	84	0:52:56.6	-72:12:54.1	180.0 ^a	128	1:25:42.4	-73:23:52.2	720.1 ^a
41	0:49:02.0	-73:08:54.9	197.3 ^a	85	1:10:48.4	-72:22:04.4	180.0 ^a	129	1:10:50.4	-72:44:17.4	780.1 ^a
42	0:48:35.5	-73:09:26.6	151.2 ^a	86	0:53:42.8	-72:23:30.2	180.0 ^a	130	0:45:51.6	-73:04:15.7	720.1 ^a
43	0:38:42.2	-73:09:01.7	177.6 ^a	87	0:52:28.4	-72:30:38.8	180.0 ^a				

Table A.10: Combined bubbles detected in the SMC OIII image (more noise). Size refers to the size of the surrounding square and is mostly slightly larger than the bubble itself.

Nr	RA	DEC	Size	Nr	RA	DEC	Size	Nr	RA	DEC	Size
0	1:08:30.6	-70:39:56.4	162.0 ^a	49	1:30:20.5	-73:10:42.2	178.3 ^a	98	1:11:01.2	-72:21:25.7	180.0 ^a
1	1:13:17.2	-70:52:53.5	188.0 ^a	50	0:48:08.2	-73:18:32.4	172.8 ^a	99	0:50:57.0	-72:33:36.7	210.0 ^a
2	0:50:50.6	-71:09:08.2	256.0 ^a	51	0:35:47.2	-73:14:13.4	156.0 ^a	100	0:50:13.9	-72:47:41.9	180.0 ^a
3	1:18:58.5	-71:07:35.4	186.0 ^a	52	1:09:49.2	-73:18:46.1	162.0 ^a	101	0:50:44.9	-72:52:31.1	225.0 ^a
4	0:33:24.1	-71:15:57.0	314.0 ^a	53	0:55:02.7	-73:19:27.9	144.0 ^a	102	0:53:15.6	-72:53:57.8	180.0 ^a
5	1:09:19.3	-71:24:22.7	162.0 ^a	54	1:13:51.3	-73:18:29.1	271.6 ^a	103	0:49:48.8	-72:53:41.6	200.0 ^a
6	1:01:11.8	-71:32:40.2	144.0 ^a	55	0:48:25.3	-73:20:00.9	214.0 ^a	104	0:56:40.5	-72:56:52.8	180.0 ^a
7	1:01:35.3	-71:33:10.7	196.8 ^a	56	0:48:15.0	-73:20:02.7	144.0 ^a	105	0:49:55.8	-72:55:51.0	180.0 ^a
8	1:01:01.8	-71:36:04.3	144.0 ^a	57	0:50:42.6	-73:20:42.7	144.0 ^a	106	0:46:23.1	-73:06:11.8	180.0 ^a
9	0:59:40.6	-71:44:43.7	162.0 ^a	58	1:15:00.6	-73:19:39.6	168.0 ^a	107	0:48:36.5	-73:09:45.5	210.0 ^a
10	1:05:12.6	-71:44:51.3	184.8 ^a	59	0:46:44.1	-73:22:03.5	162.0 ^a	108	0:48:02.7	-73:09:41.3	180.0 ^a
11	1:01:36.1	-71:51:24.2	162.0 ^a	60	0:47:31.2	-73:22:41.4	144.0 ^a	109	0:48:46.7	-73:14:14.9	180.0 ^a
12	0:57:21.2	-71:54:57.6	162.0 ^a	61	0:45:30.8	-73:23:01.8	186.0 ^a	110	0:49:48.1	-73:16:41.9	210.0 ^a
13	1:11:29.3	-72:10:05.0	188.0 ^a	62	0:46:20.1	-73:24:03.9	162.0 ^a	111	1:13:22.9	-73:17:22.3	180.0 ^a
14	1:04:25.4	-72:15:41.4	188.0 ^a	63	1:23:28.5	-73:22:25.2	186.0 ^a	112	0:49:17.6	-73:18:09.2	180.0 ^a
15	0:52:02.0	-72:16:58.5	188.0 ^a	64	1:18:44.3	-73:25:44.8	144.0 ^a	113	1:14:30.2	-73:17:53.5	180.0 ^a
16	1:11:25.4	-72:22:43.7	334.0 ^a	65	0:49:27.6	-73:29:05.8	144.0 ^a	114	1:13:27.1	-73:19:09.5	180.0 ^a
17	0:59:18.7	-72:24:40.3	144.0 ^a	66	0:46:43.7	-73:32:10.0	228.0 ^a	115	0:51:29.3	-73:22:20.2	180.0 ^a
18	1:24:04.6	-72:20:19.2	186.0 ^a	67	0:57:08.6	-73:34:11.0	188.0 ^a	116	1:14:09.2	-73:26:11.8	180.0 ^a
19	0:56:10.1	-72:27:32.3	144.0 ^a	68	0:46:46.7	-73:33:08.1	144.0 ^a	117	1:25:21.4	-73:23:57.3	255.0 ^a
20	1:03:02.5	-72:33:11.5	144.0 ^a	69	0:48:10.0	-73:35:26.8	144.0 ^a	118	0:41:20.7	-73:36:06.3	180.0 ^a
21	1:05:22.0	-72:33:32.9	220.8 ^a	70	0:40:06.4	-73:34:21.1	177.0 ^a	119	1:29:10.8	-73:34:38.2	180.0 ^a
22	0:49:24.3	-72:35:34.8	162.0 ^a	71	0:42:27.0	-73:44:43.9	162.0 ^a	120	1:12:12.0	-73:54:53.5	180.0 ^a
23	0:58:27.4	-72:39:49.0	177.6 ^a	72	0:31:44.4	-73:48:01.5	188.0 ^a	121	0:55:08.1	-74:19:11.0	180.0 ^a
24	0:58:19.1	-72:39:15.1	144.0 ^a	73	1:12:13.5	-73:55:33.5	252.0 ^a	122	0:53:12.3	-74:39:26.3	210.0 ^a
25	0:58:00.2	-72:39:56.5	186.0 ^a	74	0:38:23.6	-73:58:14.1	168.0 ^a	123	0:48:38.0	-74:51:53.9	180.0 ^a
26	1:00:56.8	-72:42:01.8	177.6 ^a	75	0:55:03.5	-74:18:22.6	156.0 ^a	124	0:32:18.7	-75:01:53.6	180.0 ^a
27	0:53:57.9	-72:44:14.5	188.0 ^a	76	0:48:36.9	-74:53:23.7	144.0 ^a	125	1:03:31.3	-72:04:05.8	480.0 ^a
28	1:20:17.1	-72:45:34.2	188.0 ^a	77	0:48:32.5	-74:55:10.9	144.0 ^a	126	0:56:21.2	-72:18:33.0	240.0 ^a
29	0:50:18.4	-72:54:25.1	162.0 ^a	78	0:49:17.1	-74:57:24.1	162.0 ^a	127	0:53:25.8	-72:23:04.1	240.0 ^a
30	1:10:03.0	-72:58:04.6	220.8 ^a	79	0:48:32.9	-74:56:58.3	299.3 ^a	128	0:47:27.0	-73:22:40.5	240.0 ^a
31	0:37:22.2	-72:59:51.0	162.0 ^a	80	0:35:57.7	-74:53:26.2	188.0 ^a	129	1:00:25.0	-71:33:46.9	360.0 ^a
32	0:47:34.3	-73:05:28.7	188.0 ^a	81	0:49:10.6	-74:57:53.9	144.0 ^a	130	1:08:15.0	-72:00:55.3	600.1 ^a
33	0:45:30.0	-73:05:22.2	144.0 ^a	82	0:48:39.8	-74:58:54.3	162.0 ^a	131	0:58:54.8	-72:10:53.9	560.1 ^a
34	0:49:05.2	-73:08:36.2	169.5 ^a	83	1:27:51.0	-75:03:51.8	188.0 ^a	132	1:05:47.8	-72:29:47.7	480.0 ^a
35	0:44:59.3	-73:10:38.6	144.0 ^a	84	0:33:26.1	-71:18:34.8	180.0 ^a	133	1:06:57.9	-72:33:11.4	480.0 ^a
36	0:38:40.0	-73:08:40.2	244.0 ^a	85	1:00:22.9	-71:34:50.9	180.0 ^a	134	0:50:55.3	-72:36:20.3	565.8 ^a
37	1:09:07.0	-73:12:44.0	144.0 ^a	86	1:27:42.1	-71:42:55.0	190.0 ^a	135	0:50:21.4	-72:52:50.7	600.1 ^a
38	1:24:11.0	-73:09:22.8	188.0 ^a	87	1:02:21.2	-71:52:25.4	180.0 ^a	136	0:47:43.1	-73:09:20.9	480.0 ^a
39	0:51:47.3	-73:14:04.6	144.0 ^a	88	1:09:06.5	-71:52:58.5	180.0 ^a	137	1:09:23.0	-73:12:06.5	504.1 ^a
40	0:45:38.5	-73:12:53.3	188.0 ^a	89	1:08:42.6	-71:59:32.8	180.0 ^a	138	0:41:00.3	-73:36:32.6	420.0 ^a
41	1:17:06.7	-73:12:35.1	162.0 ^a	90	1:07:52.4	-72:00:10.8	180.0 ^a	139	0:48:46.4	-74:52:57.5	400.0 ^a
42	0:48:17.5	-73:14:58.9	168.0 ^a	91	1:08:20.3	-72:01:42.5	180.0 ^a	140	1:27:44.7	-71:41:46.2	480.0 ^a
43	0:48:29.1	-73:16:15.0	195.6 ^a	92	1:03:44.6	-72:04:26.5	180.0 ^a	141	0:46:24.4	-73:08:00.4	480.0 ^a
44	1:14:15.3	-73:15:51.1	186.0 ^a	93	1:03:19.6	-72:09:52.2	180.0 ^a	142	0:49:55.5	-73:15:22.2	480.0 ^a
45	0:54:18.8	-73:17:14.7	162.0 ^a	94	0:52:55.4	-72:12:42.0	200.0 ^a	143	1:25:45.5	-73:23:28.6	720.1 ^a
46	0:45:22.7	-73:15:42.4	162.0 ^a	95	0:54:08.5	-72:13:27.0	180.0 ^a	144	1:10:57.7	-72:43:57.9	720.1 ^a
47	1:14:09.2	-73:16:04.7	144.0 ^a	96	0:51:51.2	-72:18:44.9	180.0 ^a	145	0:45:37.9	-73:04:12.1	720.1 ^a
48	0:47:58.1	-73:17:16.9	162.0 ^a	97	0:56:01.1	-72:20:13.6	180.0 ^a				

Appendix B

banana documentation

Banana is to be used for a variety of MT/MF related functions. By default, it creates Minkmaps for a round window with diameter given by smooth of the (absolute) value of ψ_s for the brightness given by mint. Alternatively (3d true), it takes numt logarithmically spaced values from mint to maxt and saves a fits file with numt layers. Can also calculate the complex average (avg true) or the average of the absolute value (additionally abs_avg true). Phases can be saved instead with arg true. Commands are discussed in detail in the list further below, here is a short overview.

makeBanana true leads to the calculation of various MF/MT for the areas of the image defined in the regions in mask (syntax see below) and the thresholds given by mint, maxt and numt. For every object in the maskfile a separate output table is created.

makePeach true is similar to makeBanana, but varies the window size instead of the brightness threshold at the given mask regions. Saves one table for every object.

makeHist true expects a file containing names of files containing point coordinates given by stars command (syntax see below) and creates a histogram of the input file brightness at the position of the points. Bins are linearly spaced with parameters mint, maxt and numt. File identifier given by histapp appended to each file.

makePointsread true takes a list of files containing points in the same format as for makeHist and creates an image with a gaussian of standard deviation given by smooth at the location of each star.

makePNGs true creates png files with a logarithmic brightness scale of the regions in mask with red given by infile, green by greenfile and blue by bluefile. monochrome true leads to creation of monochrome infile-based pngs. To remove single bright spots image can be eroded/dilated with diameter erd before.

makeHedgehog true creates linedensity maps at given smooth and calls makeBubbles true. Uses parameters lineThresh and lineScale for threshold of bubble detection and scale factor for length of line. smooth value of Minkmap to which image is compared is hardcoded for several relevant smooth values and set to 3-smooth by default. Details see text.

makeBubbles true searches for bubbles for existing linedensity map using lineScale and lineThresh. Also see makeHedgehog.

makePattern [linedensity/minkmap/infile/infile_log] creates a point pattern with intensity given by image according to command (infile_log means using the logarithm of the file in infile) and saves it as a table (can be read by R). Only takes image values larger than lineThresh into account (by default zero). infile can be smoothed with diameter given by smooth and eroded/dilated with diameter erd.

Recommendations:

Set a suitable file identifier (e.g. wavelength) with filePrefix and the correct folders for minkmaps, line densities, pointsread, and PNGs.

Many of these functions require calculating the shift in pixel coordinates introduced by smoothing relative to the original file to convert back and forth between corresponding locations. This is done by saving the header variable CRPIX1 of the original file and comparing it to that of the smoothed file. While it is hard-coded for the example commands file:halphi and similar, it can be manually entered with the command CRPIX1. Especially important if infile is not an unshifted file.

Every command except the file:[name] commands demands either a number or true/false (false = anything except the word "true") as arguments. Give arguments separated by space after command
Syntax:

```

command Name of corresponding variable in source code, description

    in infilename, FITS file to be read
    mask maskfilename, File with names of objectfiles to be included in the originalBanana or
    makePNGs or makePeach call (everything else masked per object)
boxesToExclude boxesToExcludeName, text file containing boxes (format see below) to be set to zero in
infile
filePrefix wavelength, prefix for file to be used in further filenames, usually wavelength
    stars histfile, list with one ds9 region file located in ./objects/ per line containing pixel co-
    ordinates of stars in original image for histogram/other statistics (without .reg-ending,
    added automatically)
    histapp histappendix, name appendix for histogram, enter anything besides histfile
    mint min_thresh, minimal threshold
    maxt max_thresh, maximal threshold
    numt num_thresh number of (logarithmically spaced) thresholds to be considered
outminmap outminmap, saving directory of Minkowski-map FITS file. Settings will be appended
to the name
outlinedens outlinedens, saving directory of line density file
outpointspread outpointspread, saving directory of pointspread fits file
    outPNGs outPNGs, saving directory of PNGs
        s s, rank of Minkowski tensor to be used
    smooth smooth, diameter of circle to be smoothed in marching-squares-map. Set either square-
    size or smooth
squaresize squaresize, set size of squares for brute-force Minkowski-map. Set either squaresize or
smooth. Smooth recommended over squaresize for speed reasons.
    erd erd, set diameter of erosion/dilation smoothing of the infile(s) to be done before origi-
    nalBanana/creating PNGs
    3d threeD, if true: consider all different thresholds, else: consider only maximum. dDfault:
    false
    avg average, if true: average over all calculated thresholds, else: write 3D FITS file. Only
    relevant if 3d is set. Defalut: false
    abs_avg absolute_avg, if true: calculate absolute values of maps first, then average. Only
    relevant if avg is set
    arg Take phase instead of absolute value of tensors. Default: false
CRPIX1 crpix_source, sets the given value as the global reference value. Should be the value
CRPIX1 of the input file from which the maps to be used have been/will be created.
Used to calculate shifts in pixel coordinates.
makeBanana makeBanana, if true: sets make_minkmap to false, such that the IMTs of the whole
(masked) image are calculated, possible to erode/dilate before with erd command. De-
fault: false
makePeach make_peach, if true: sets make_minkmap to false, calculates averaged (over maskfile)
IMTs of given regions depending on smooth diameter. Relies on pre-existing minkmaps,
saves output in ./results/. Default: false
makeHist makepointHist, if true: sets make_minkmap to false, calculates histogram of point
sources given in stars command for given file. Also creates histogram of whole image,
saves output in ./results/. Default: false

```

- makePointsread** `make_pointsread`, if **true**: sets `make_minkmap` to false, calculates spread of point sources given in stars command for given point spread function (11.07.19: Only gauss ATM) and diameter given by `smooth`, `specific width = smooth/2`. Saves as FITS-file, saves output in `outpointsread`. Default: false
- makePattern** `make_patternFromImage`, `linesorminkmap`, Accepts "linedensity", "minkmap", "infile", or "infile_log" as follow-up commands, creates a R-readable table with around 4-5000 points with the number of points proportional to the value at that square, saves in `./results/`. Input given by command, output name either name of input file or wavelength (in case of "infile[_log]"). Infile gets smoothed with given `windowSize` and eroded/dilated with diameter `erd`, with `infile_log` also logarithm taken before smoothing. Default: false
- combineRegions** `combine_regions`, Takes all maskfiles given by combination and combines bubbles from smaller to larger size; set `mask` to name output. Outputs various formats: each combined bubble as objectfile containing its original boxes and maskfile listing them, ds9-readable files for each bubble containing all original boxes, R-readable plain table containing average centers of bubbles, ds9-regionfile containing average centers and sizes of all bubbles
- makePNGs** `makePNGs`, if **true**: sets `make_minkmap` to false, creates PNGs containing single objects either monochrome or with R = `infile`, G = `greenfile`, B = `bluefile` (default: G=SII, B=SII/H α) based on the objects in maskfile, possible to erode/dilate images before with `erd` command, saves output in `outPNGs/`. Default: false
- monochrome** If **true**: make monochrome images based on just `infile` (default), else read `greenfile` and `bluefile`. Default: true
- greenfile** Filename of green layer of PNG. Default: SII
- bluefile** Filename of blue layer of PNG. Default: SII/H α
- makeHedgehog** `make_hedgehog`, if **true**: reads `minkmap` with given `smooth` and standard parameters, writes ds9 region file in `./results/` containing lines at angles of regions with $q_2 > 0.01$, threshold given by `lineScale` sets length scale ($\text{length} = \text{smooth}/2 \cdot |q_2| / \text{lineScale}$), creates fits file in `outlinedens` with number of lines crossing every block. Also makes bubbles (see below). Default: false
- lineThresh** `line_thresh`, threshold of line density for bubble detection/threshold for point pattern generation (only fields above this considered)
- lineScale** `line_scale`, factor by which length of lines is divided
- makeBubbles** `make_bubbles`, if **true**: reads line density Fitsfile with given wavelength, threshold and `smooth` value, then takes every block with line number higher than threshold given by `lineThresh` and $|q_2| > |q_2|$ at about three times larger `smooth` (see switch `smooth`), creates ds9 region file in `./results/` with boxes centered around those blocks and `width=2*smooth`. Writes every box into object file in `./objects/` and names of boxes into `maskfile`. Default: false
- filewithoutWCS** `filewithoutWCS`, to be used for FITS files that were created with gimp and do not contain any coordinate keyword. Simple placeholder settings are added and file is saved with a second `.fits` ending. Useful for the ds9 "lock: frame: WCS" tool when displaying several images in parallel
- readkey** `WCSkeynames.push_back([...])`, read given key in addition to standard WCS keywords from `infile`
- file:halpha** Sets `infilename`, `outminmap`, `outfilename`, `keynames`, `boxesToExcludeName`, `mint`, `maxt`, `numt`, `crpix_source` to correct settings for H α image of LMC
- file:oiii** Sets `infilename`, `outminmap`, `outfilename`, `keynames`, `boxesToExcludeName`, `mint`, `maxt`, `numt`, `crpix_source` to correct settings for OIII image of LMC
- file:sii** Sets `infilename`, `outminmap`, `outfilename`, `keynames`, `boxesToExcludeName`, `mint`, `maxt`, `numt`, `crpix_source` to correct settings for SII image of LMC

file:sii/ha Sets infilename, outminmap, outfilename, outpointsread, outlinedens, outPNGs, keynames, mint, maxt, numt, crpix_source to correct settings for SII/H α image of LMC using division with threshold 0.1

Syntax of files containing objects:

- combination-file: Contains name of one maskfile in every line listing bubbles of one size, starting at lowest size.
- maskfile: Contains name of one object in every line. For every such object an equally named file containing boxes in ./objects/ is expected. Lines beginning with '#' are ignored.
- Files containing boxes to be in-/excluded (objects): One box per line with the following four space- or tab-separated numbers in pixels: RA/x center, DEC/y center, x width, y width (ds9 coordinates in pixels of original images, y axis flipped compared to internal coords)
- histfile: Contains name of one ds9 point-objectlist in every line. For every such line an equally named file containing point-regions in ds9 image coordinates in ./objects/ is expected. Lines beginning with '#' are ignored.
- Files containing point-regions are expected to be of the form *([ra],[dec])* in the image coordinate system of the raw images. ds9 format is preferred.

Example commands:

Typical H α -minkmap:

```
./banana file:halpha s 2 3d true maxt 40 mint 0.1 numt 9 smooth 10 avg true
```

Typical SII-minkmap:

```
./banana file:sii s 2 3d true maxt 40 mint 0.045 numt 10 smooth 100 avg true
```

Typical OIII-minkmap:

```
./banana file:OIII s 2 3d true maxt 40 mint 0.1 numt 9 smooth 10 avg true
```

Typical banana:

```
./banana file:halpha s 2 3d true maxt 20 mint 0.1 numt 17 avg true makeBanana true mask allObjects erd 3
```

Typical peach:

```
./banana file:halpha s 2 3d true maxt 40 mint 0.1 numt 9 avg true makePeach true mask allObjects
```

Typical region-PNGs:

```
./banana file:halpha mask allObjects erd 3 monochrome false greenfile mygreenfile.fits bluefile mybluefile.fits
```

Typical hedgehog:

```
./banana file:halpha makeHedgehog true s 2 smooth 40 3d true avg true lineScale 0.4 lineThresh 20
```

Typical bubbles:

```
./banana file:halpha makeBubbles true smooth 40 lineScale 0.3 lineThresh 21
```

Typical histogram:

```
./banana file:halpha in /data/ccollischon/lmccalc/ha40-ha100.fits stars allObjectLists maxt 1. mint -1. numt 100 makeHist true histapp ha_40-100
```

Typical pointsread:

```
./banana file:halpha makePointsread true smooth 250 stars allObjectLists
```

Typical point pattern:

```
./banana file:halpha makePattern linedensity smooth 40 s 2 avg true lineScale 0.3 lineThresh 12
```

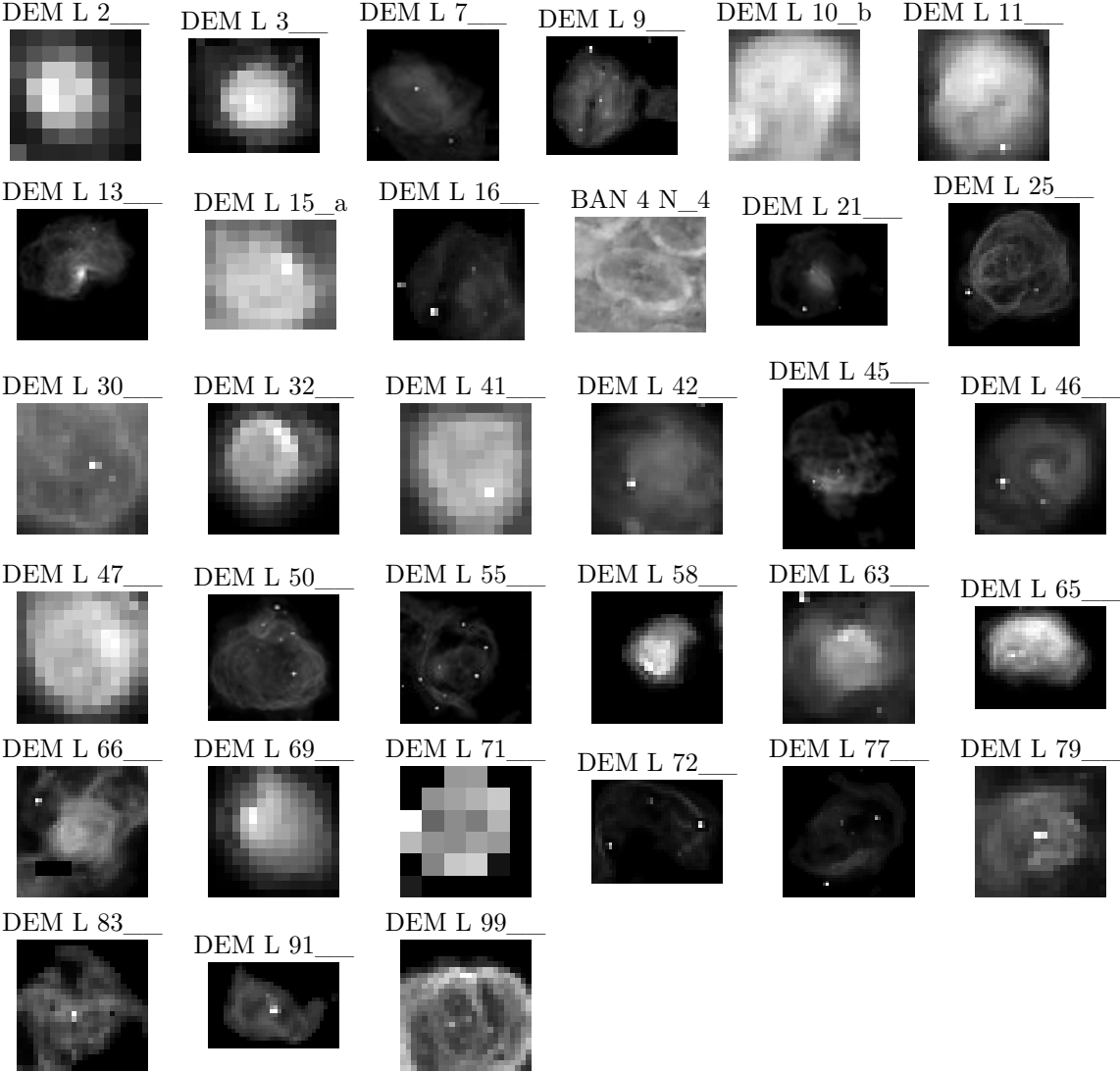
Typical region combination:

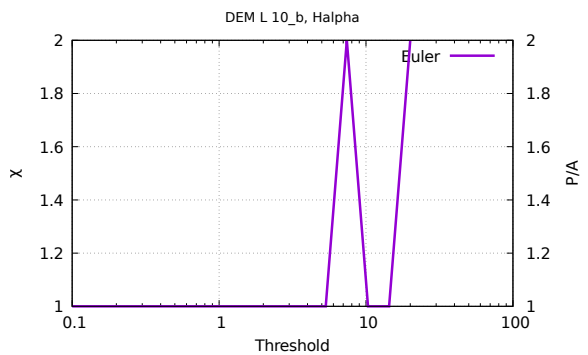
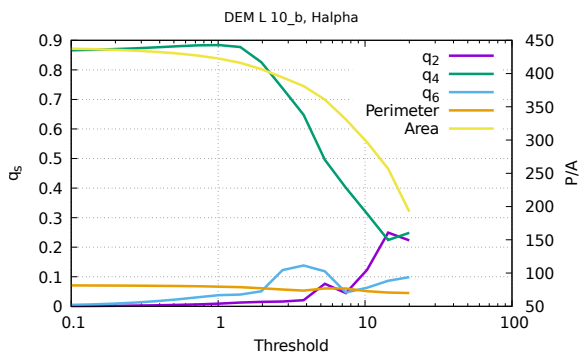
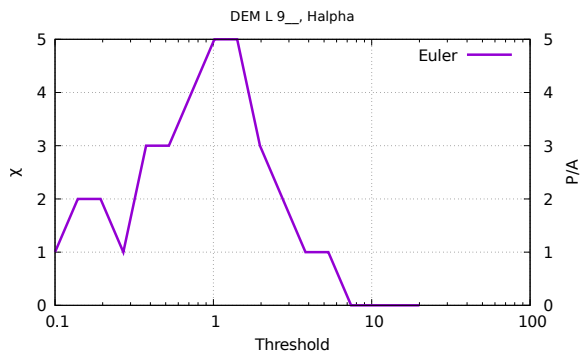
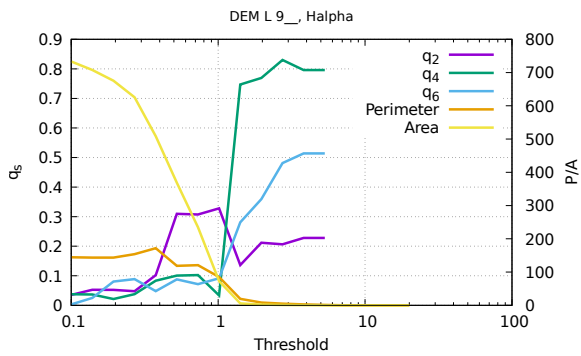
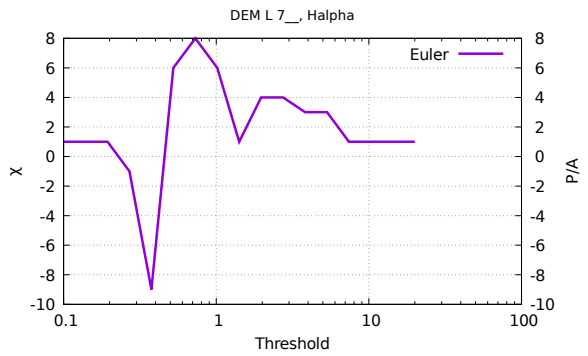
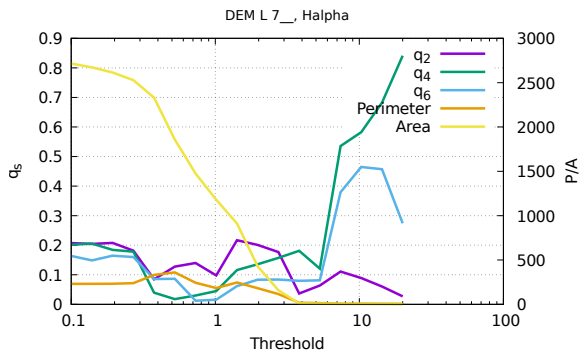
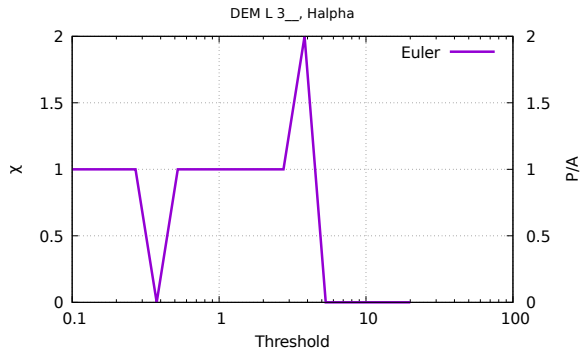
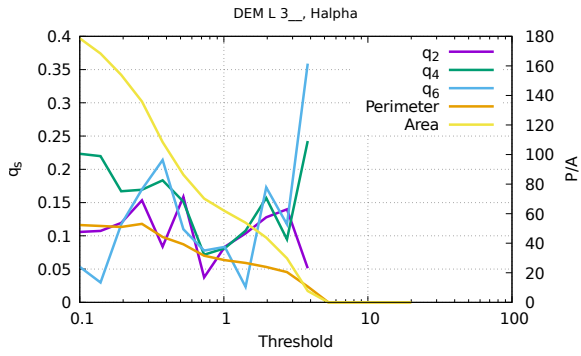
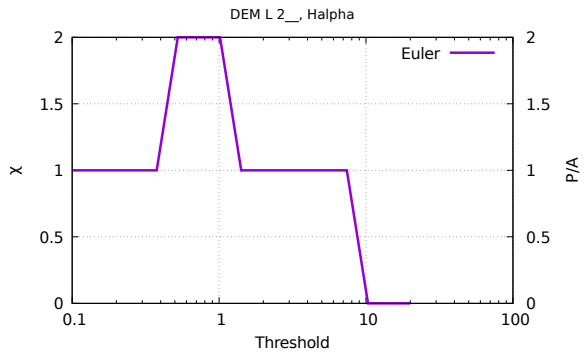
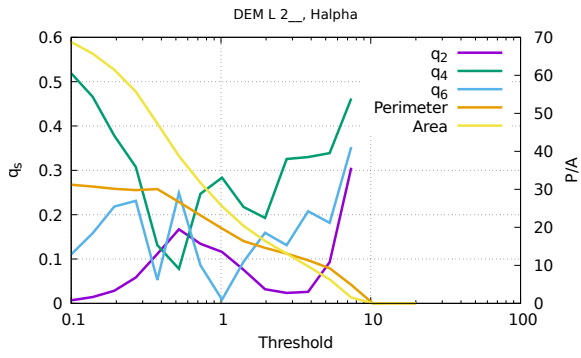
```
./banana file:halpha combineRegions true combination bubbles_sorted_listoflists mask bubbles_sorted_combined_list
```

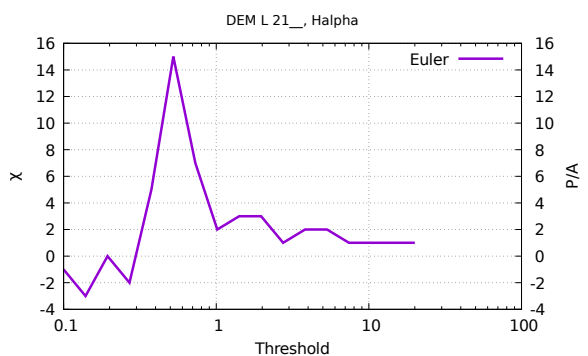
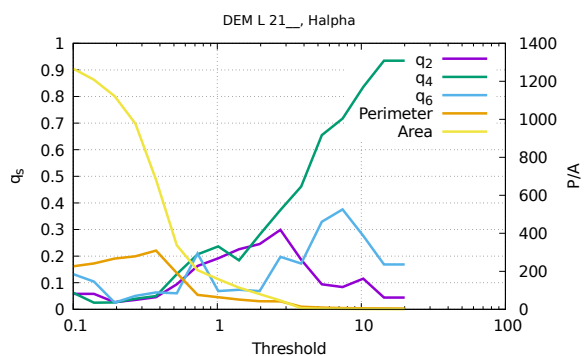
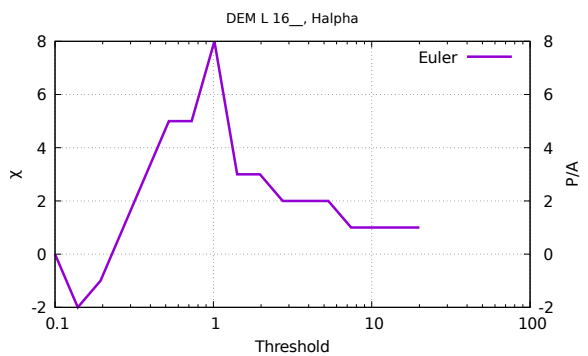
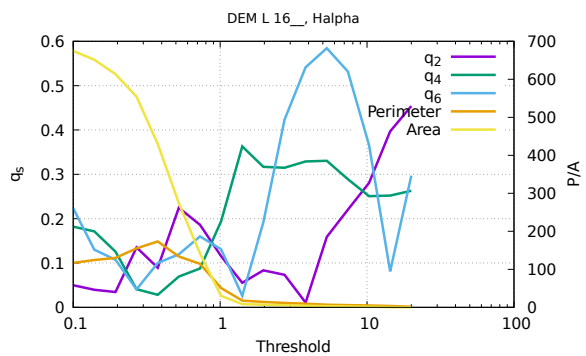
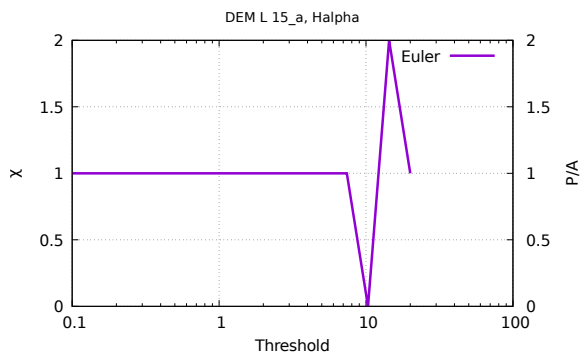
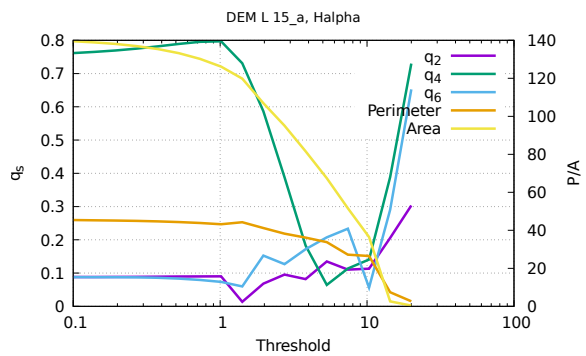
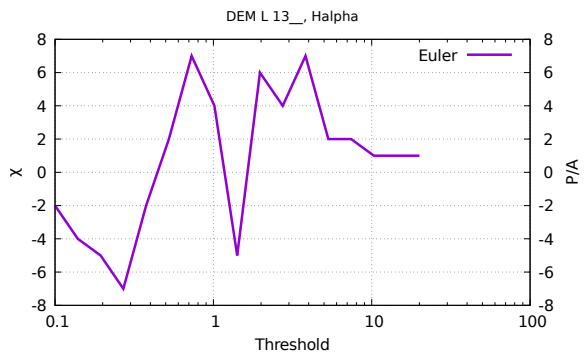
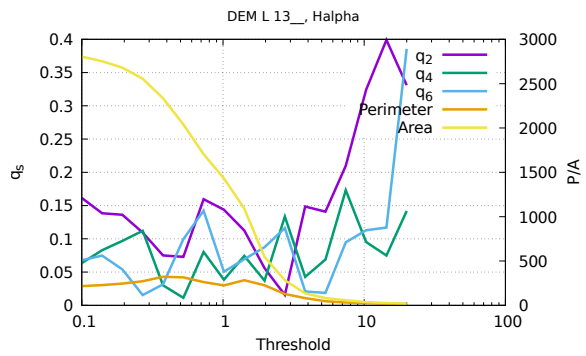
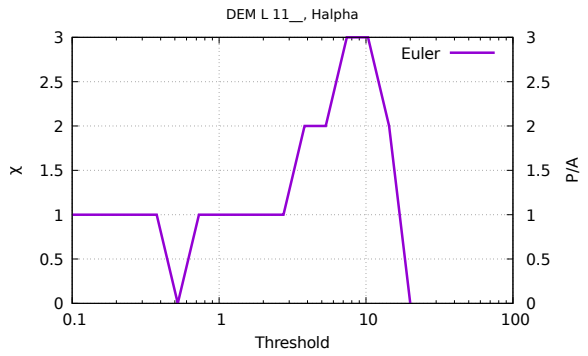
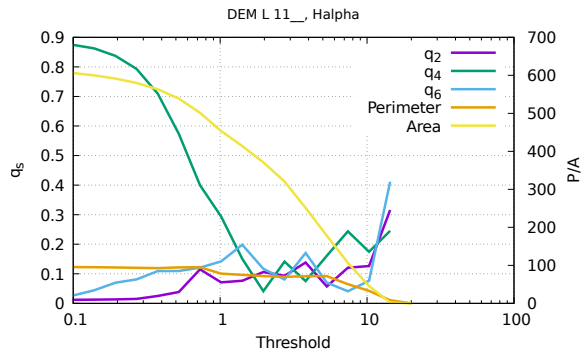
Appendix C

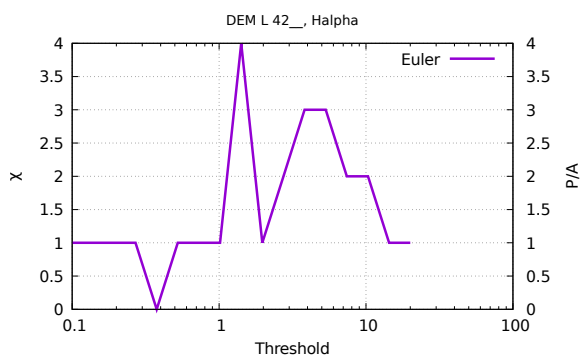
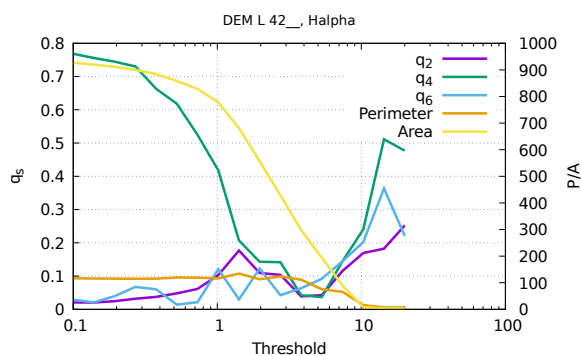
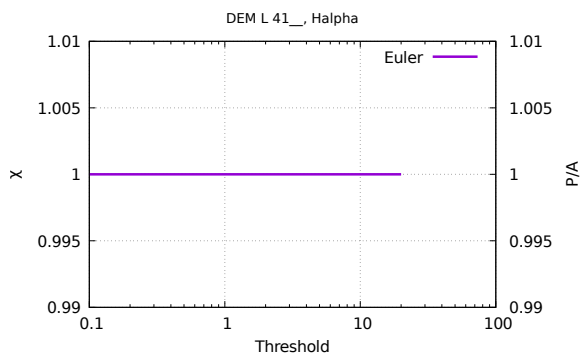
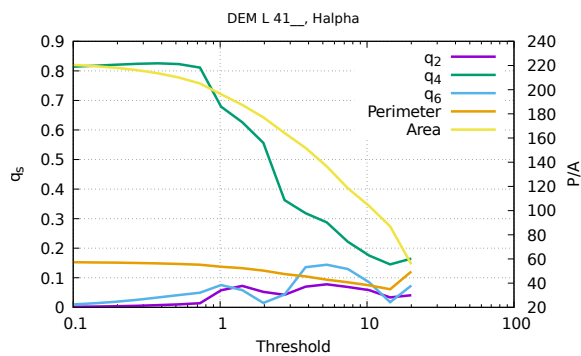
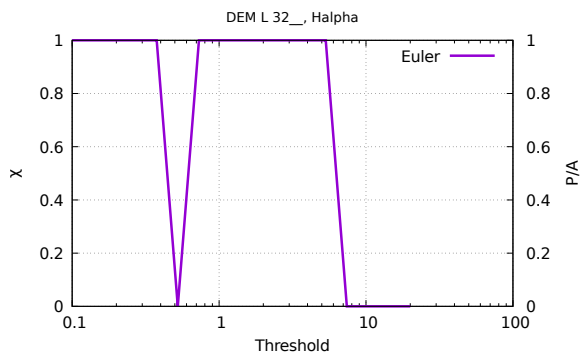
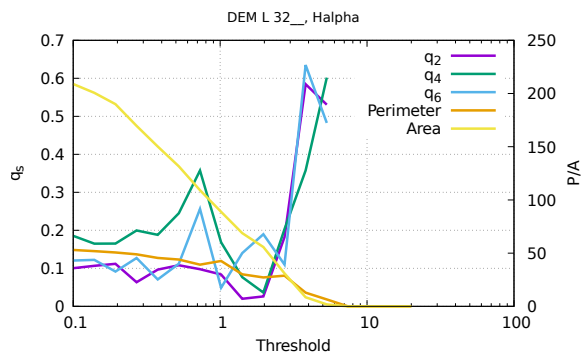
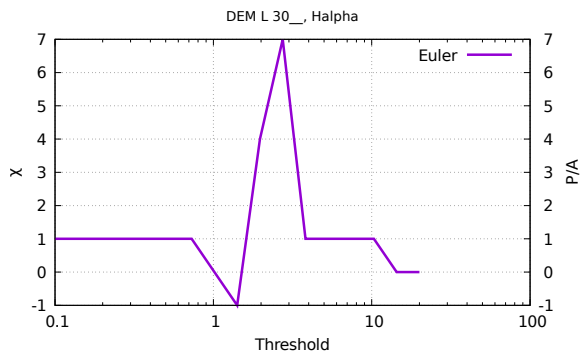
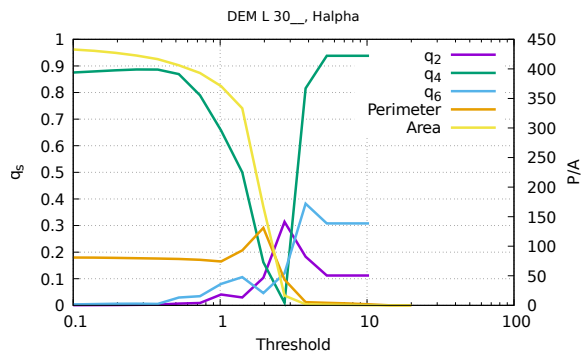
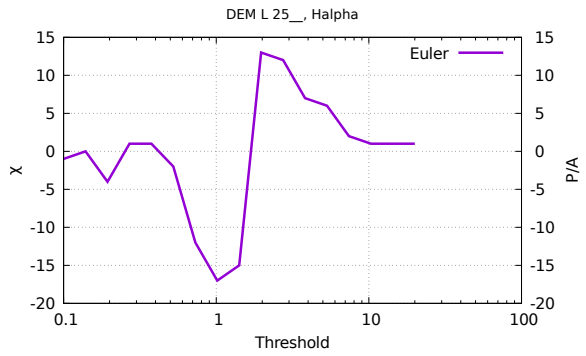
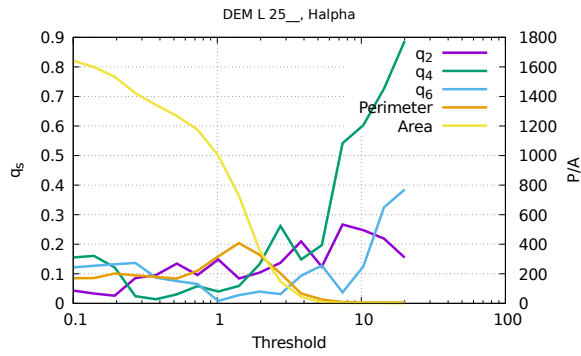
banana graphs and images

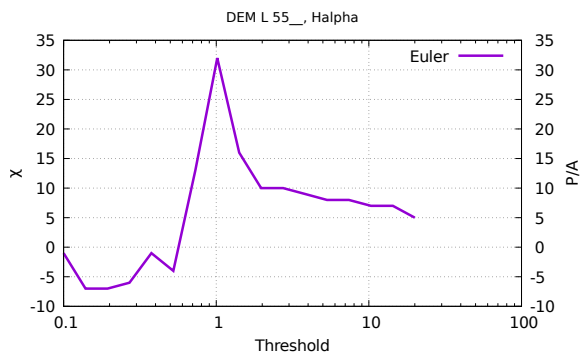
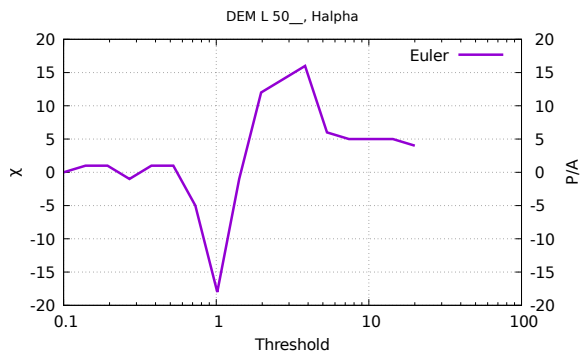
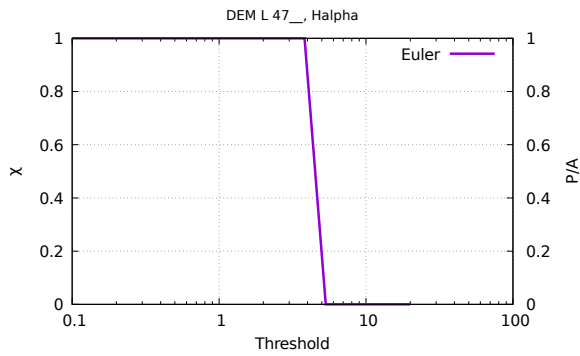
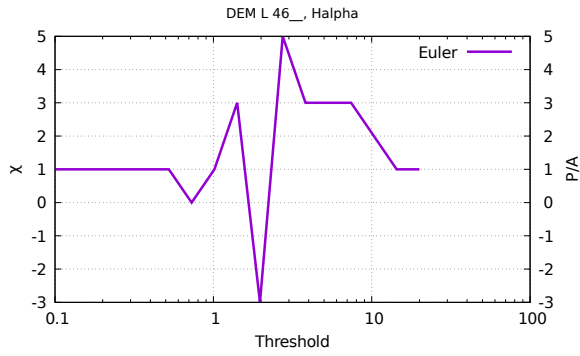
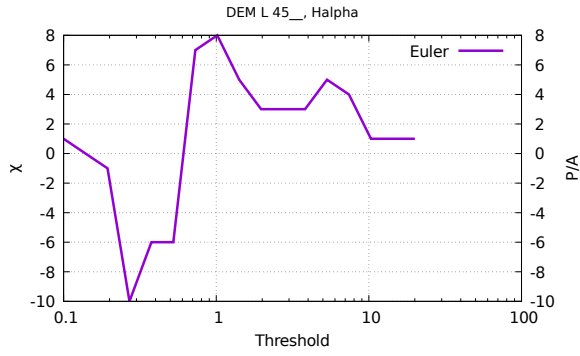
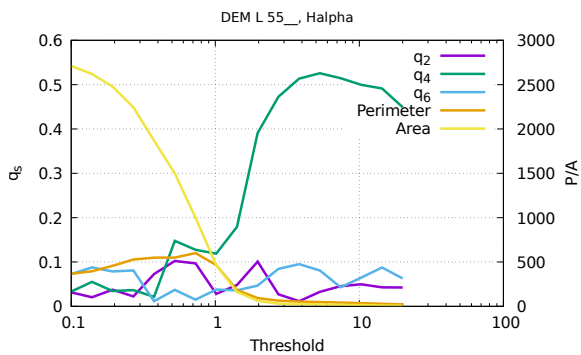
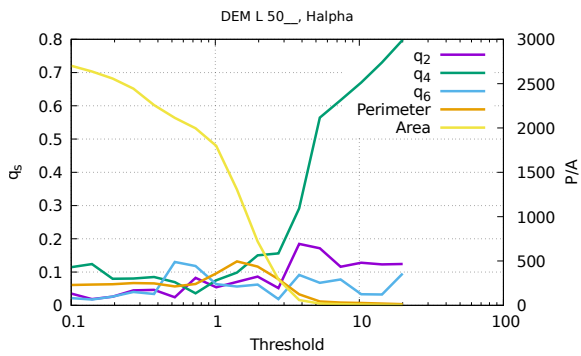
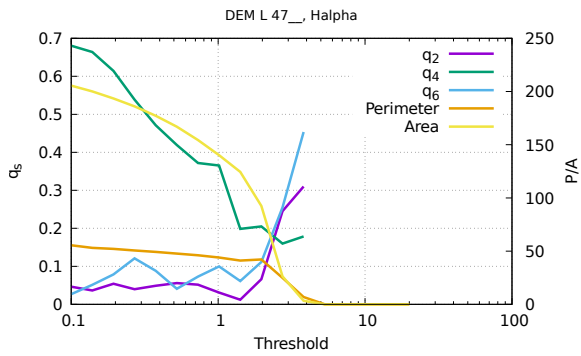
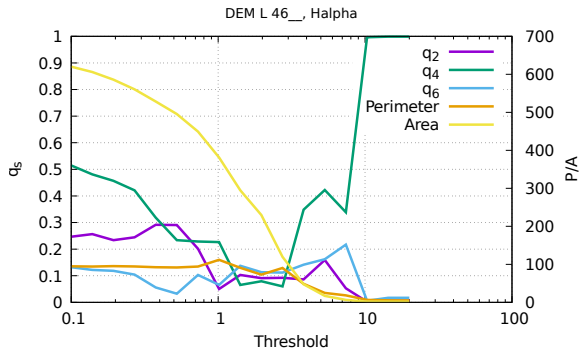
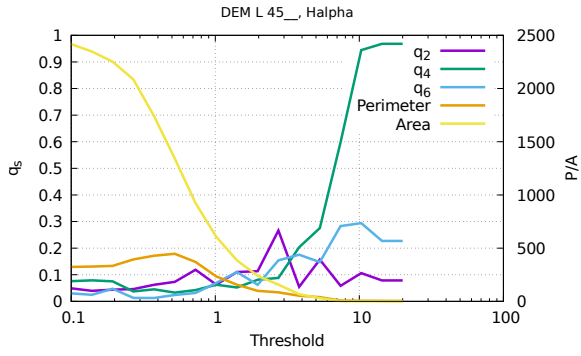
C.1 Bubbles

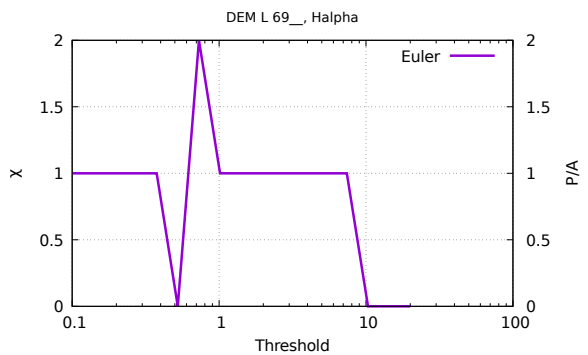
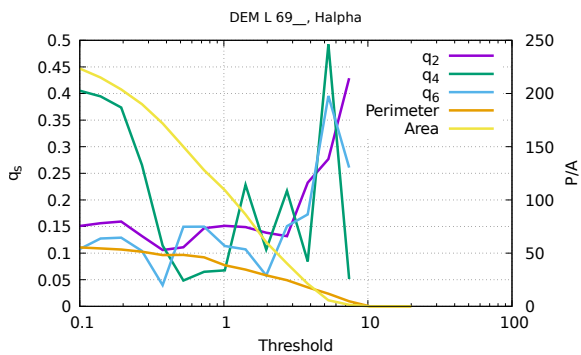
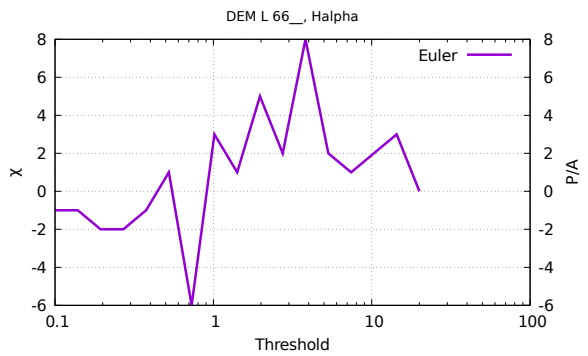
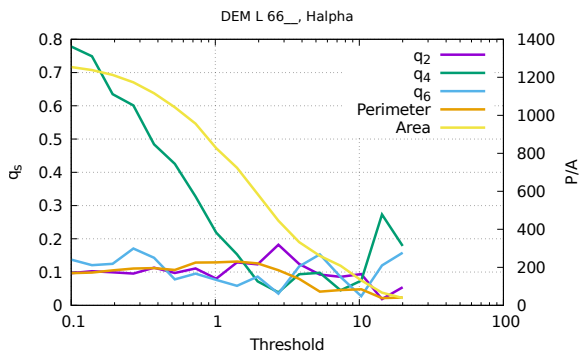
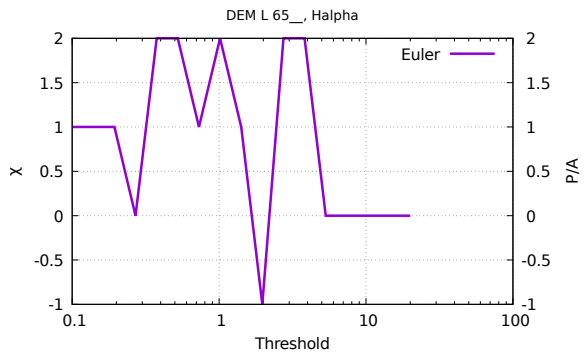
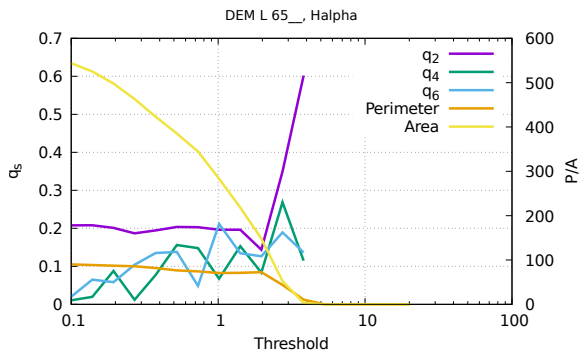
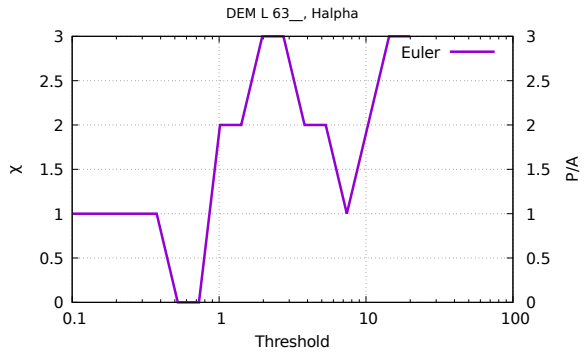
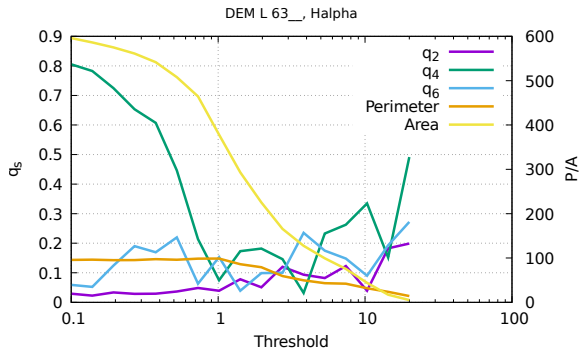
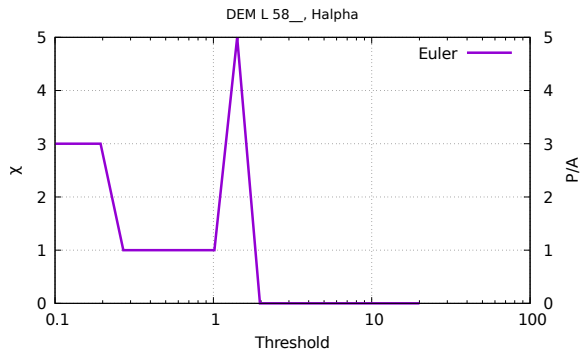
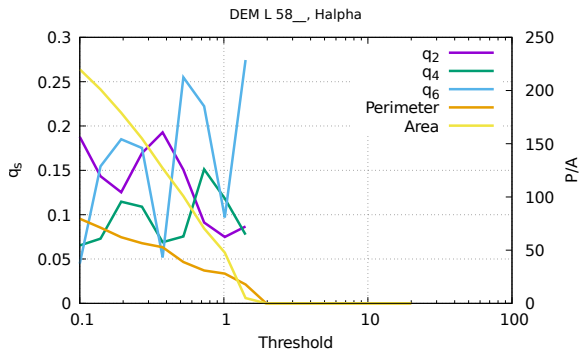


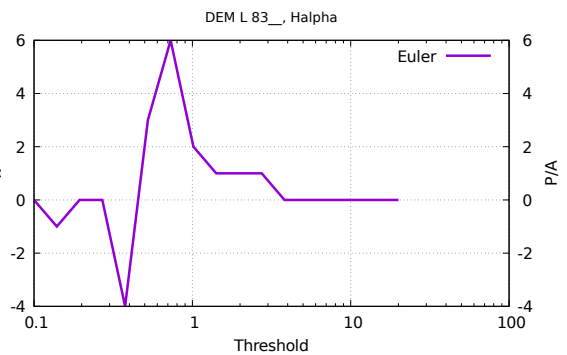
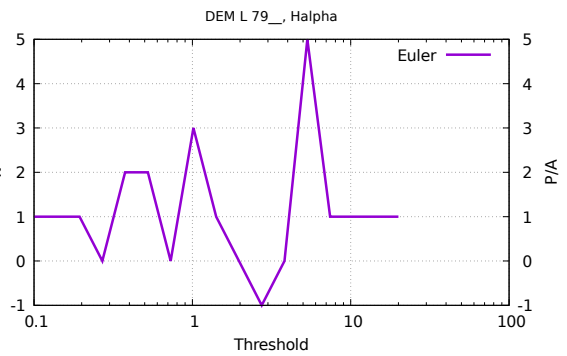
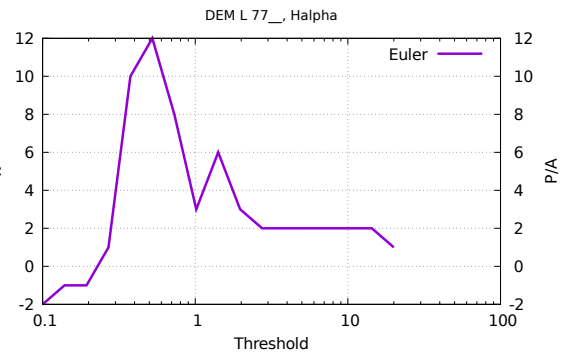
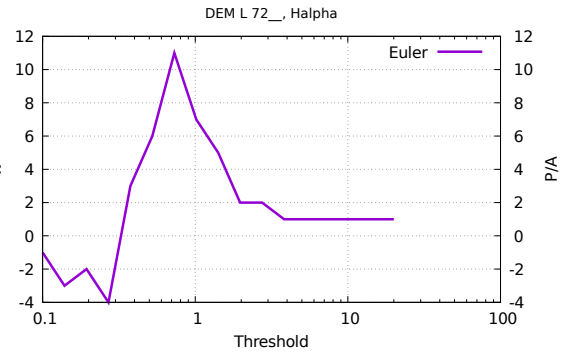
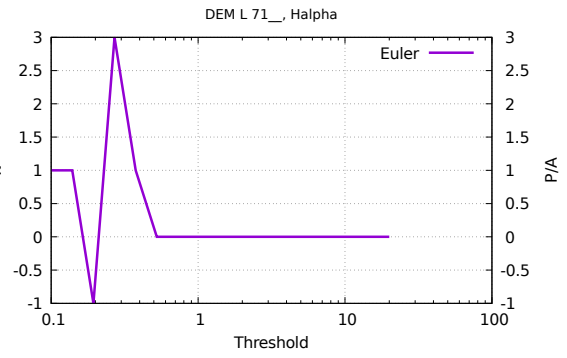
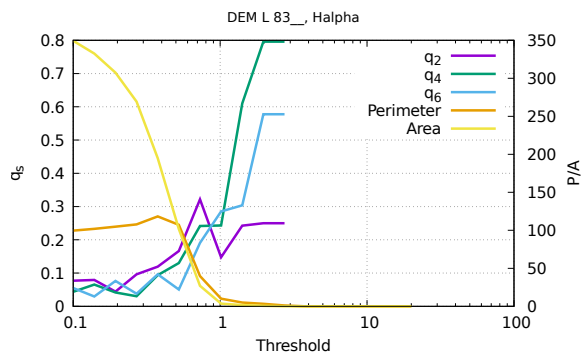
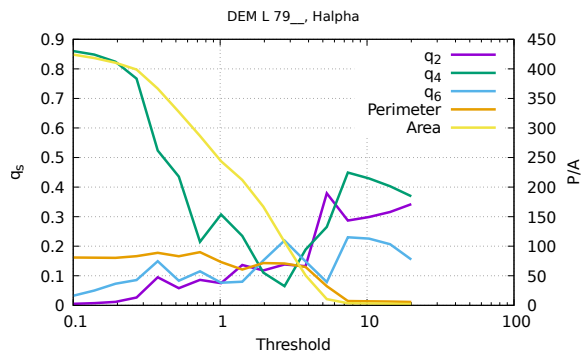
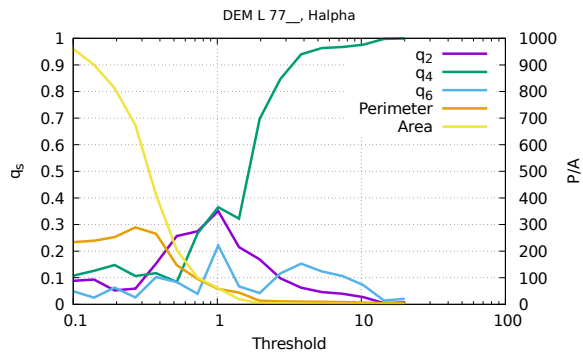
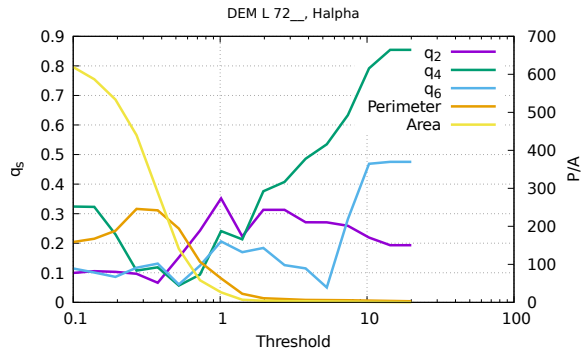
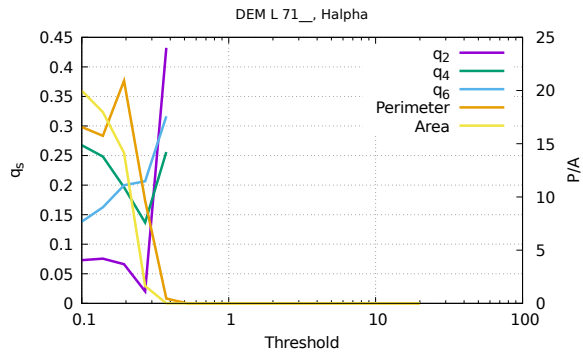


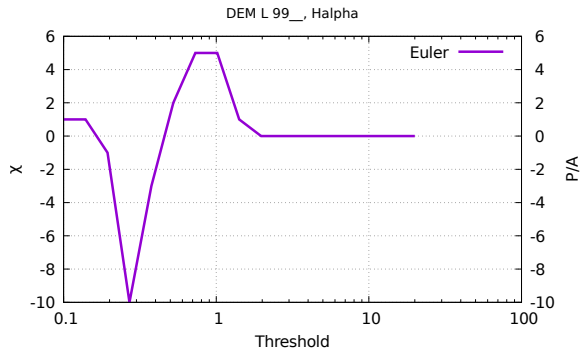
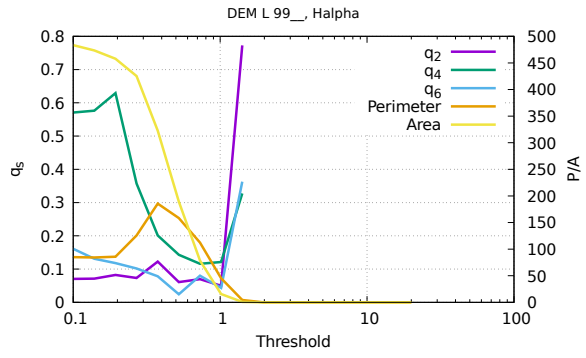
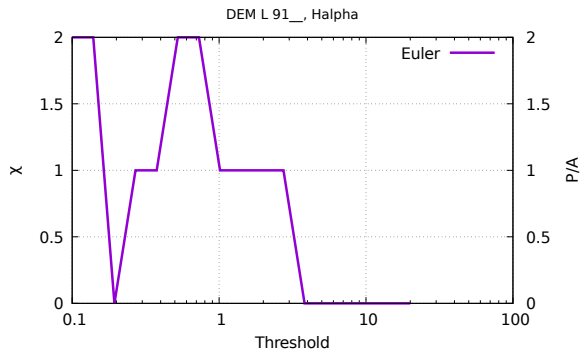
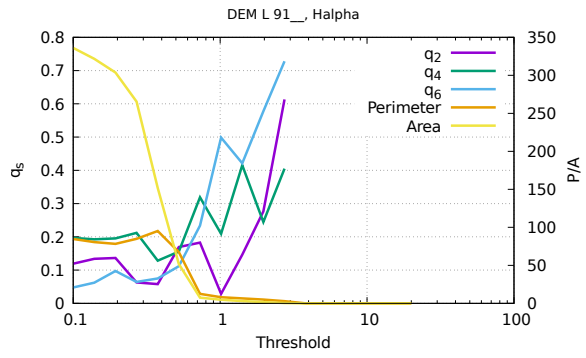






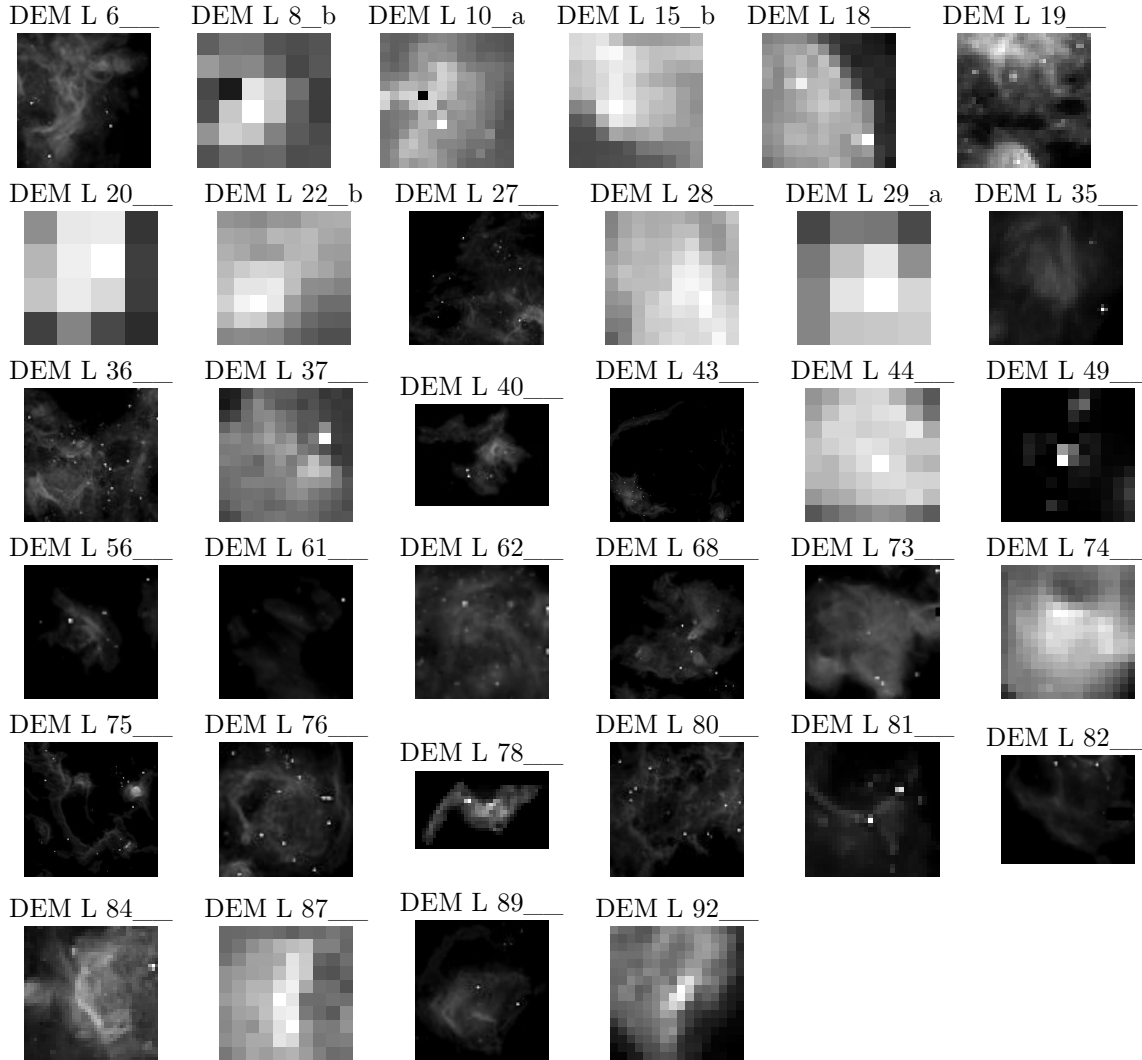


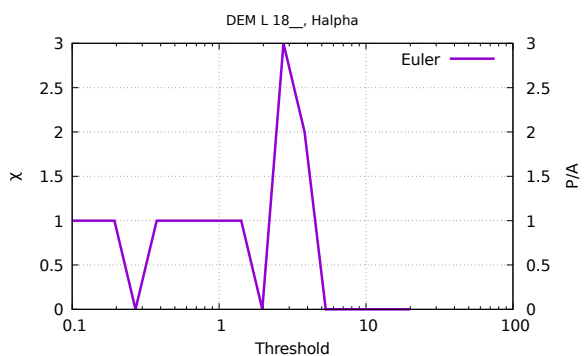
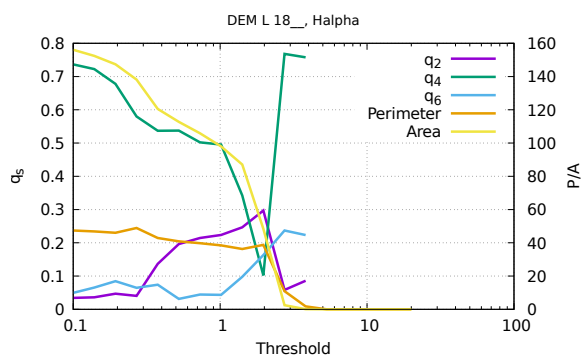
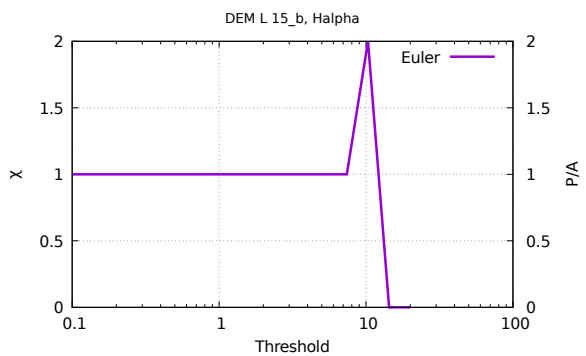
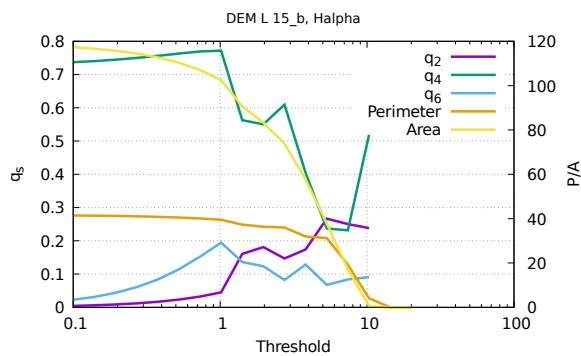
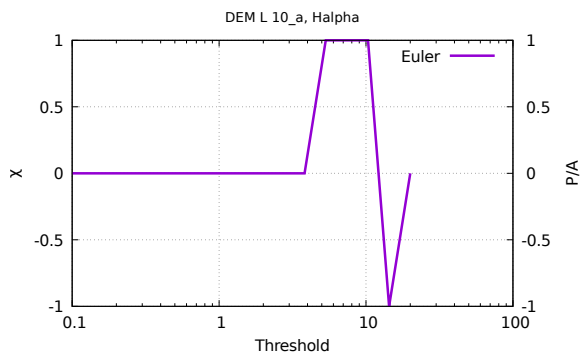
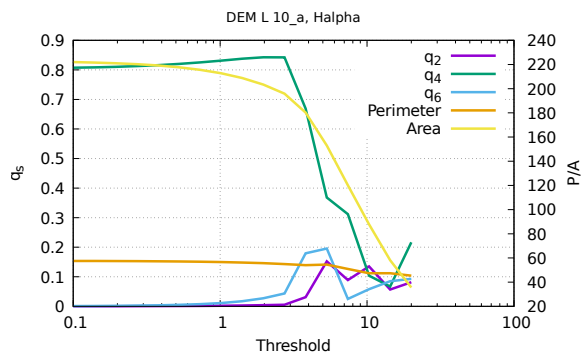
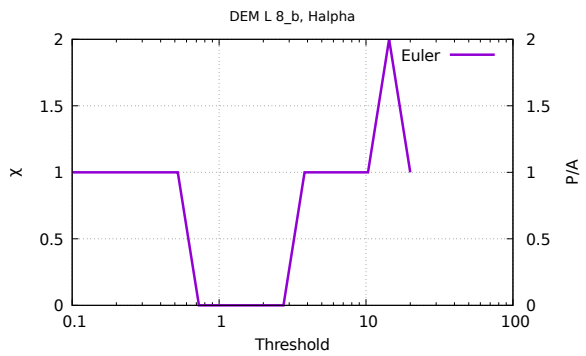
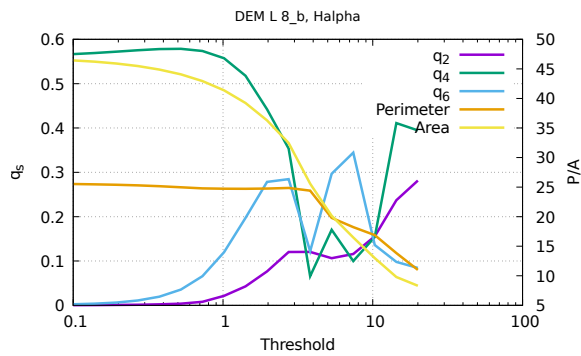
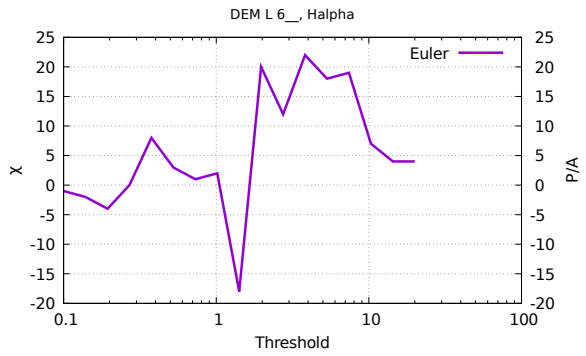
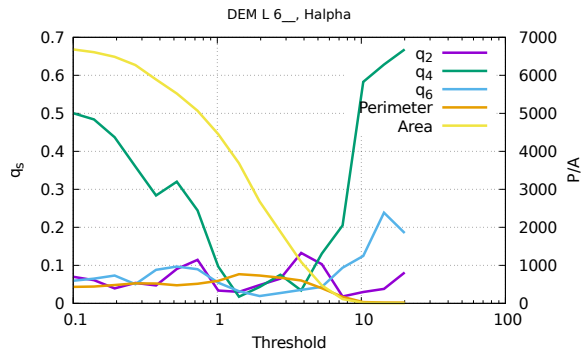


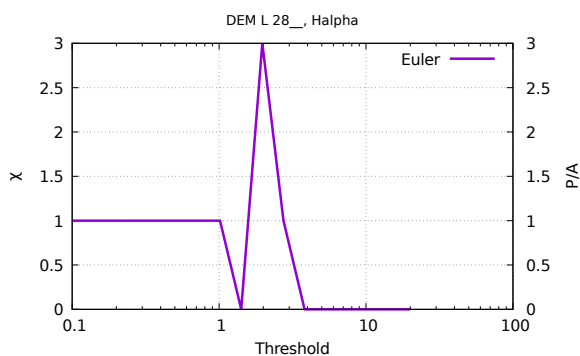
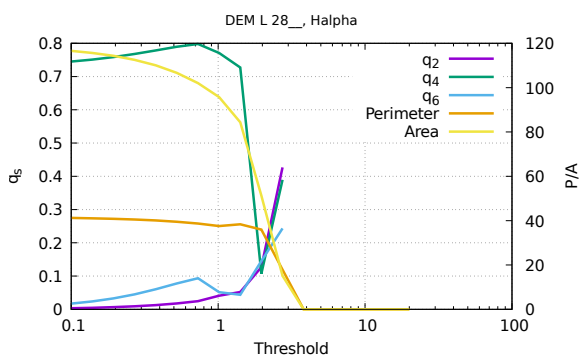
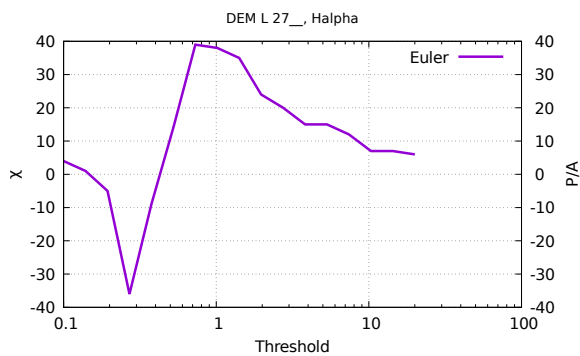
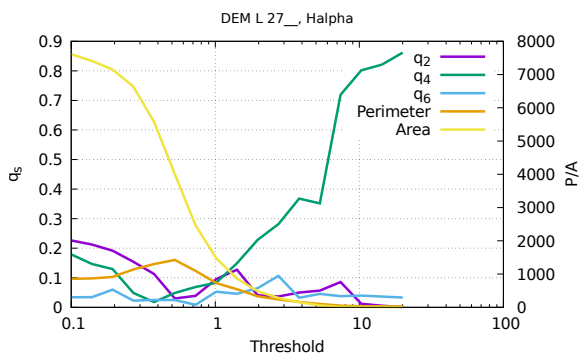
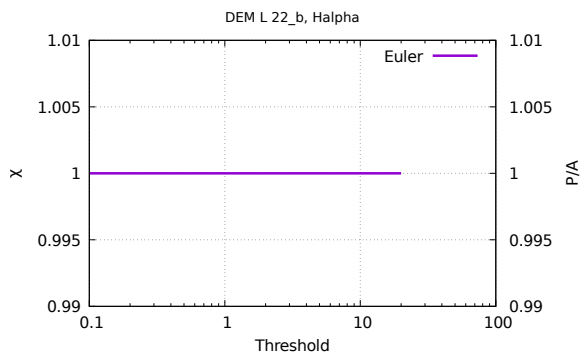
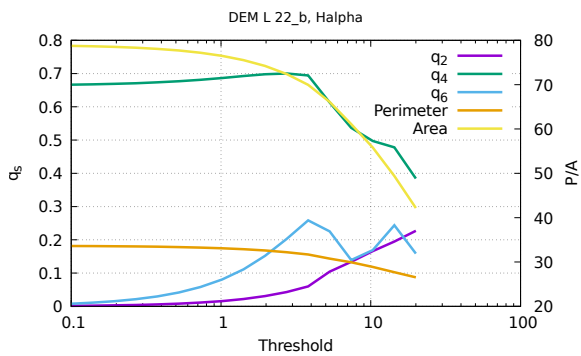
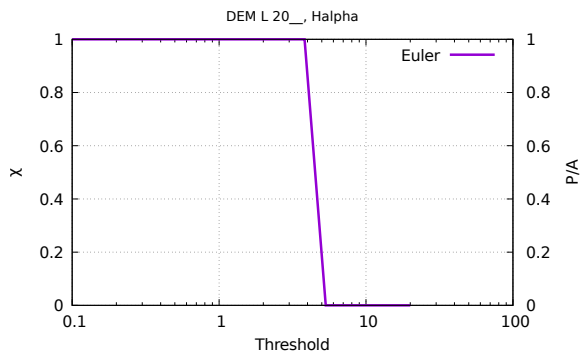
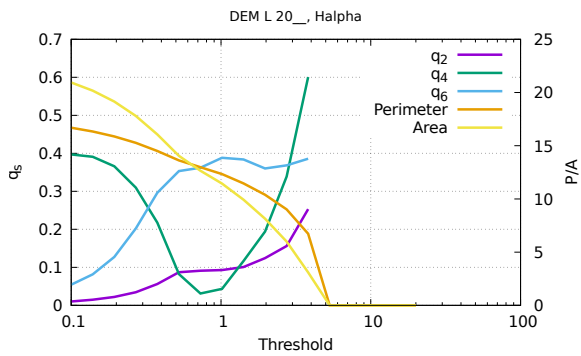
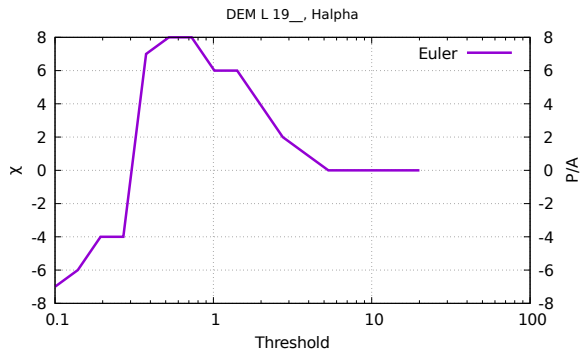
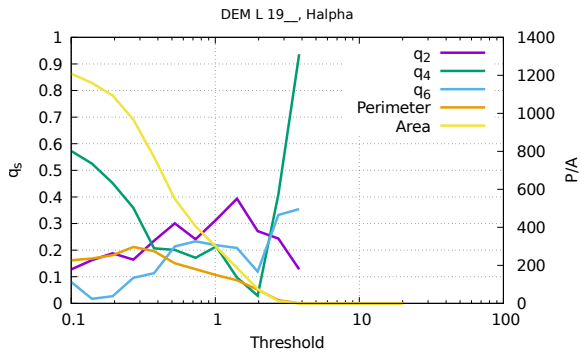


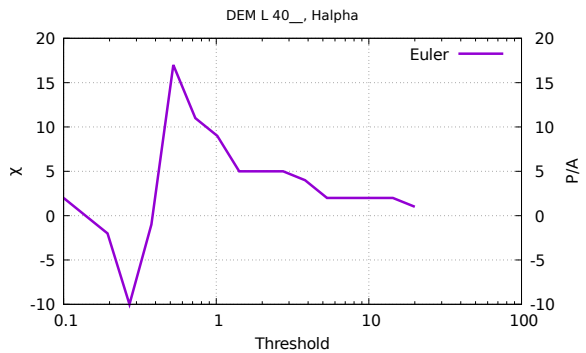
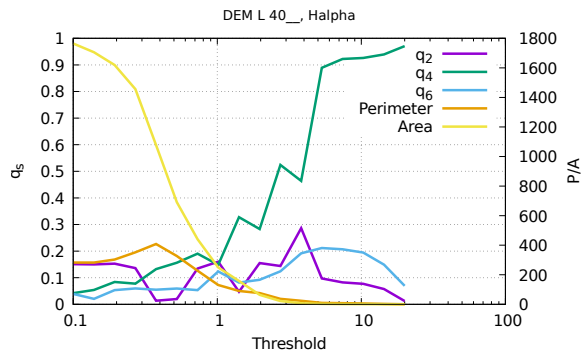
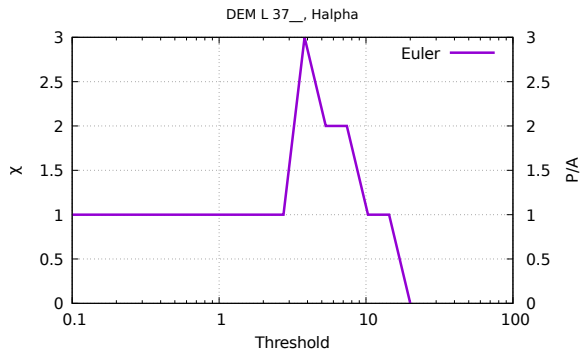
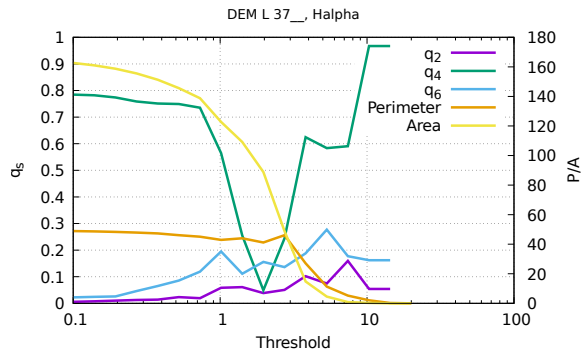
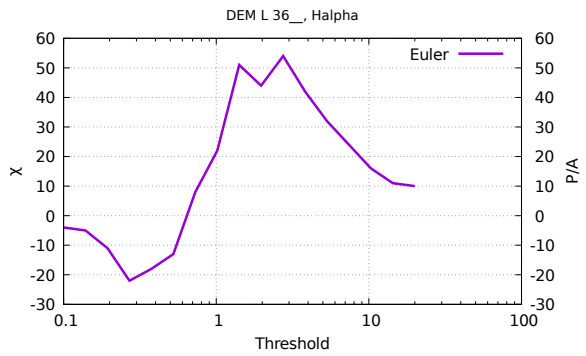
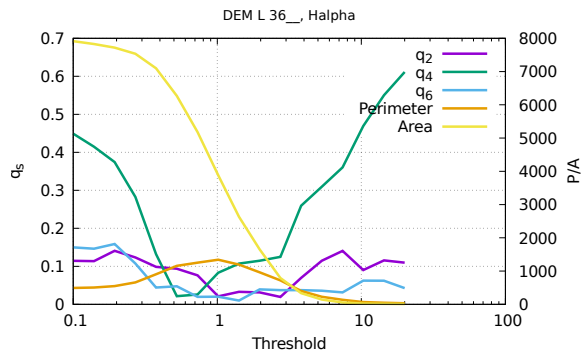
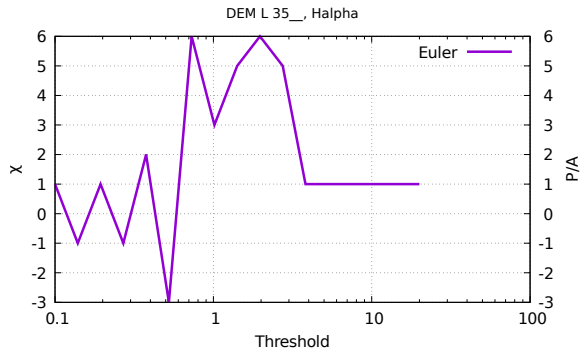
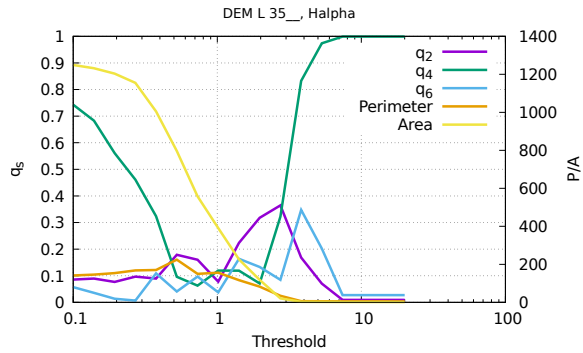
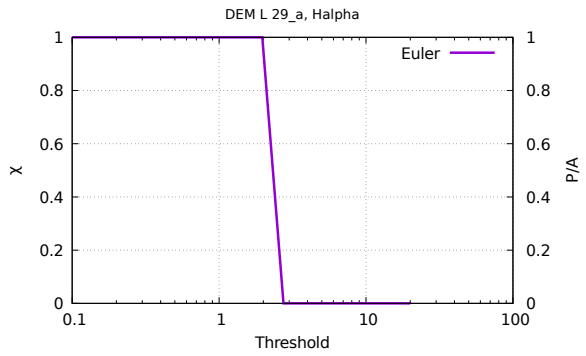
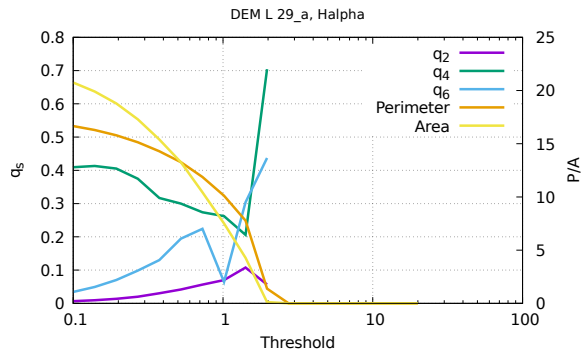
C.2 Non-bubbles

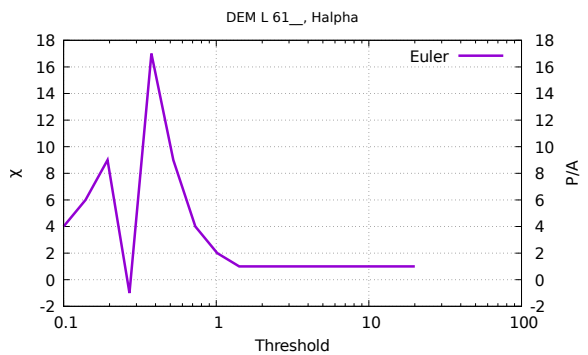
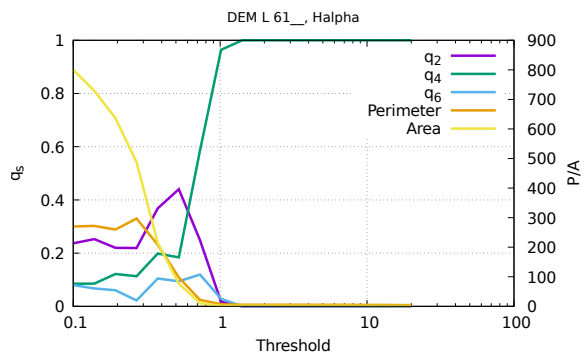
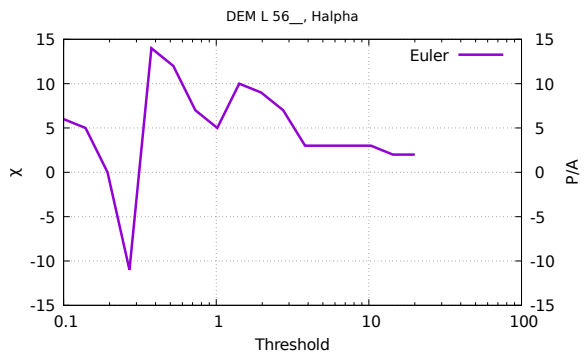
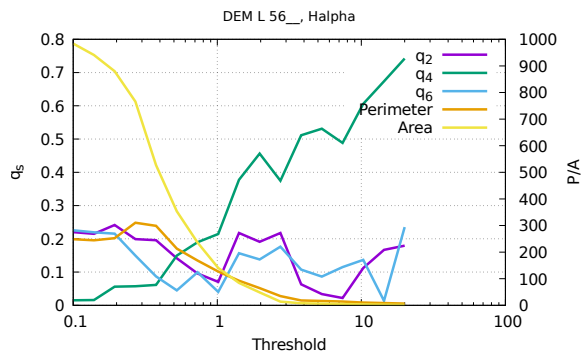
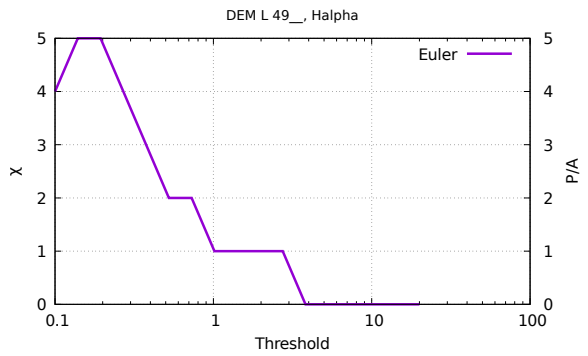
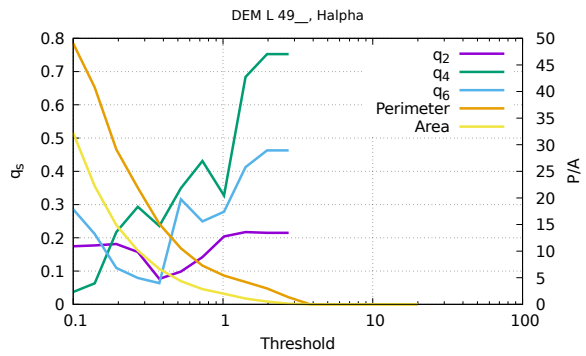
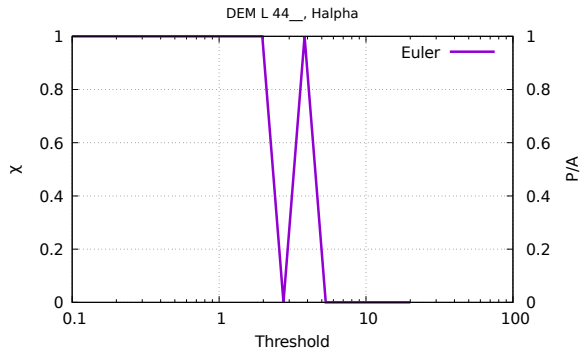
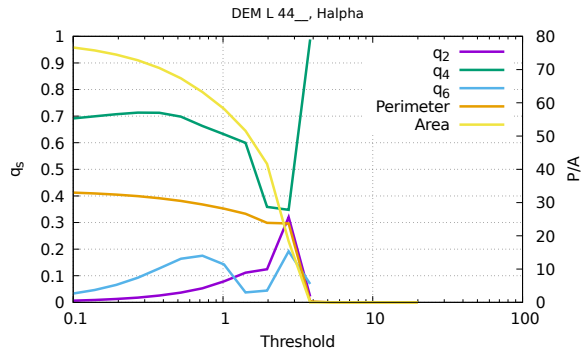
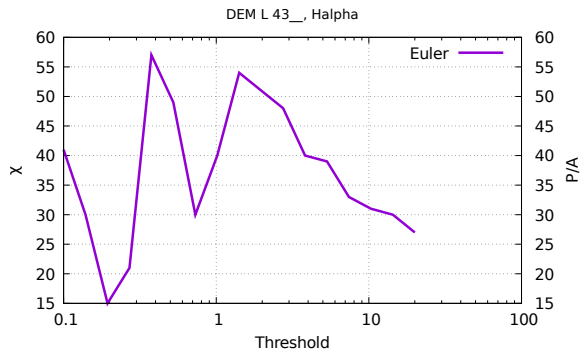
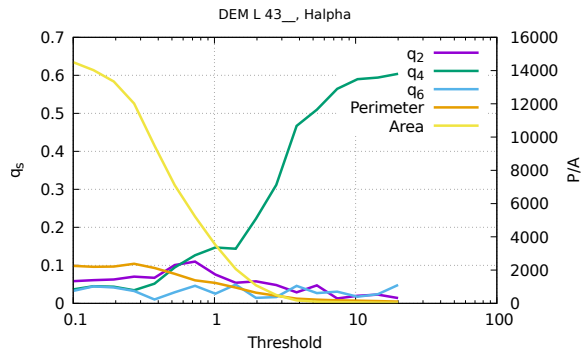
The following pages contain grayscale $H\alpha$ images of manually selected bubbles and non-bubbles from the catalog of Davies et al. (1976) followed by graphs of their MF and MT with respect to the brightness threshold. The images were logarithmically scaled such that the brightest pixel value is 255 in every image - their relative brightness is not comparable. Roll pizza dough, add tomato sauce (not too much), add mozzarella. Cut banana into thin slices and place on top of mozzarella. Add curry powder. Bake at highest possible setting until done. Absolute values of MT are displayed.

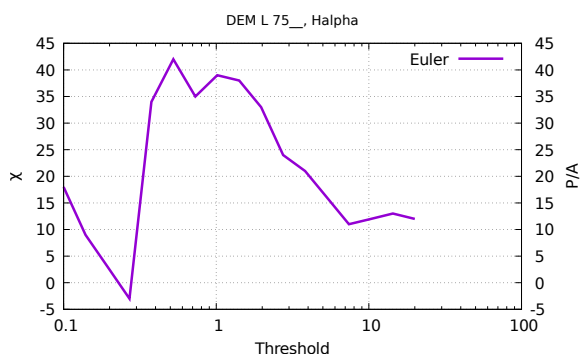
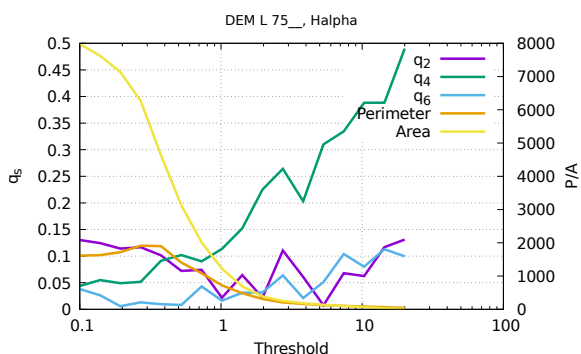
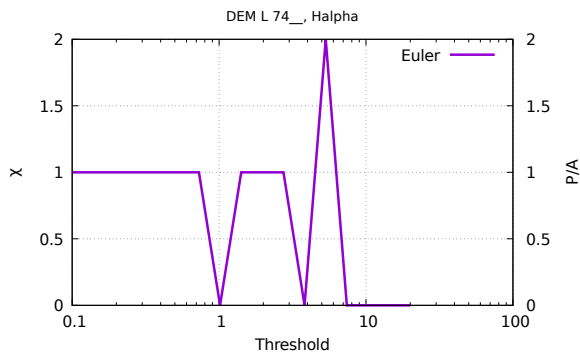
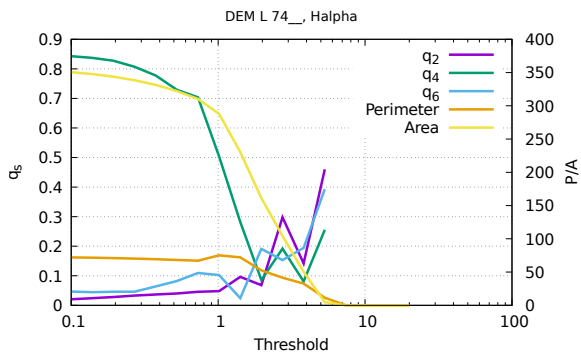
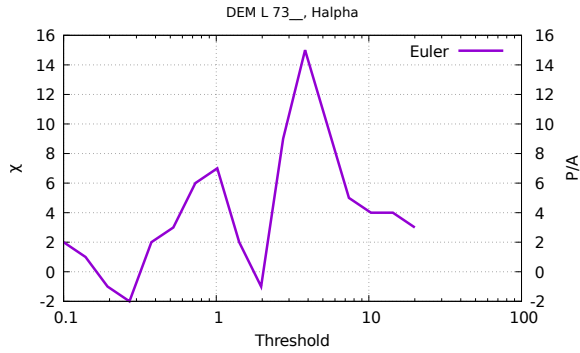
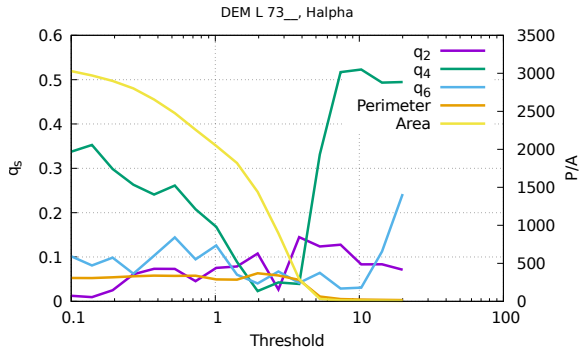
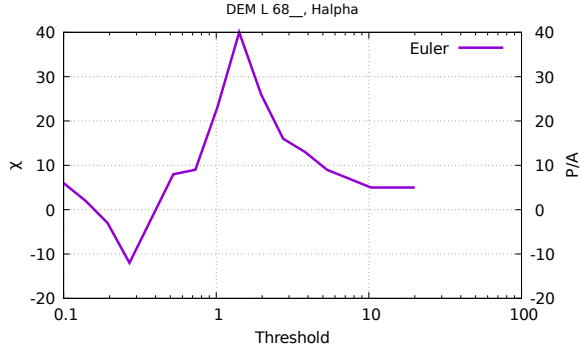
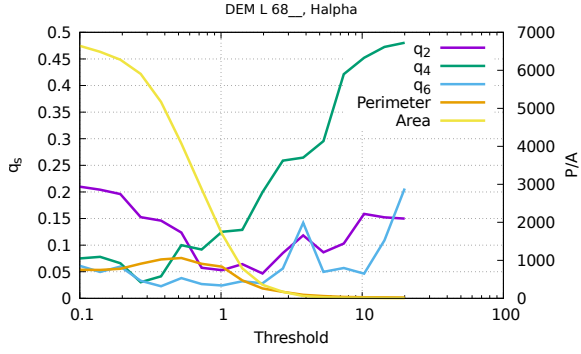
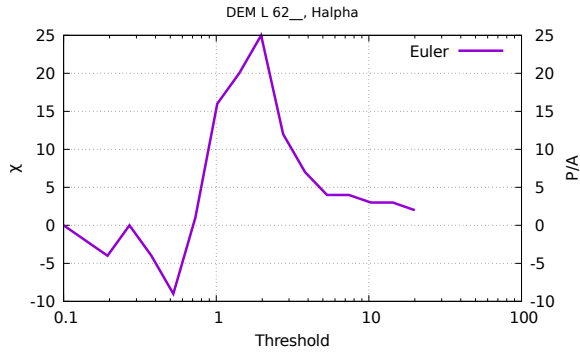
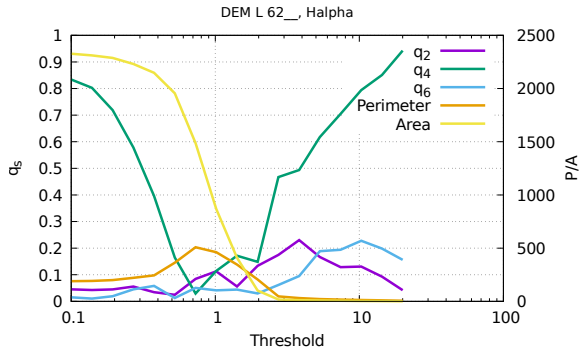


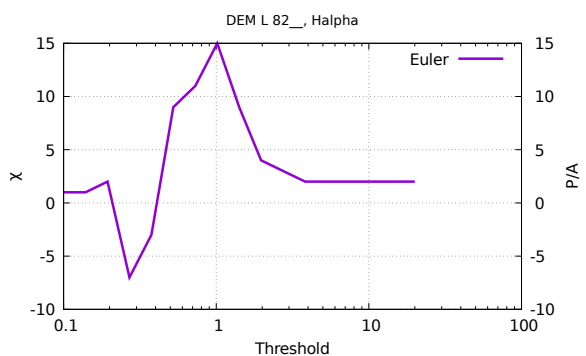
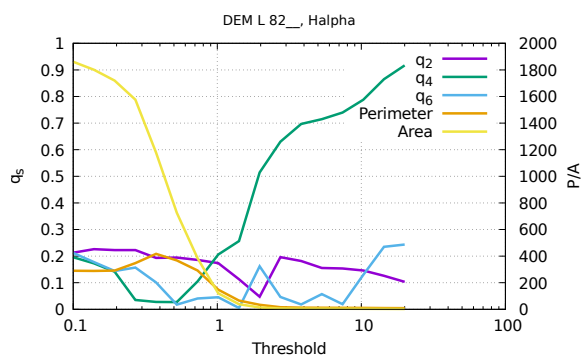
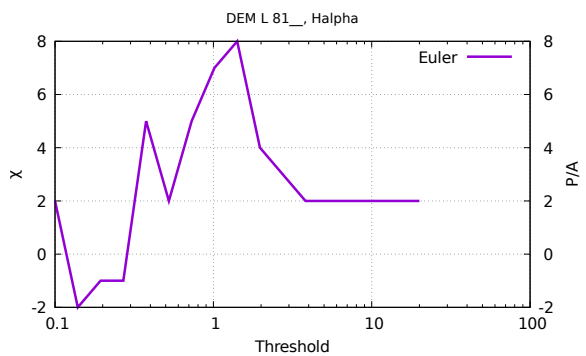
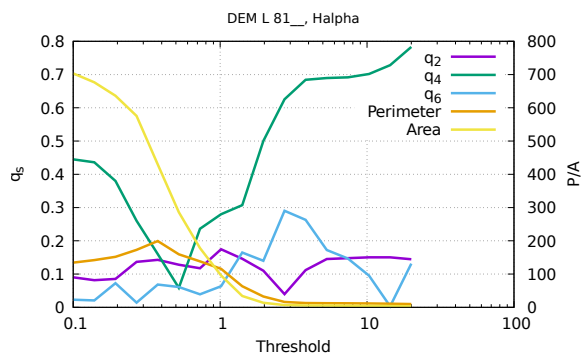
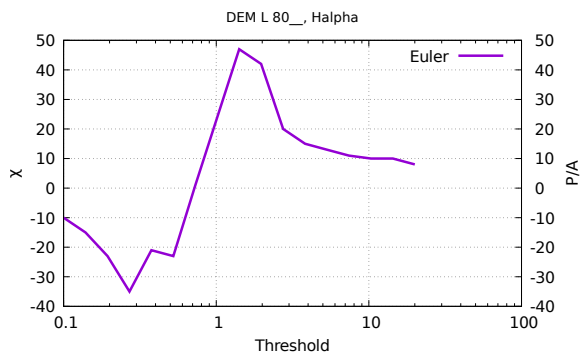
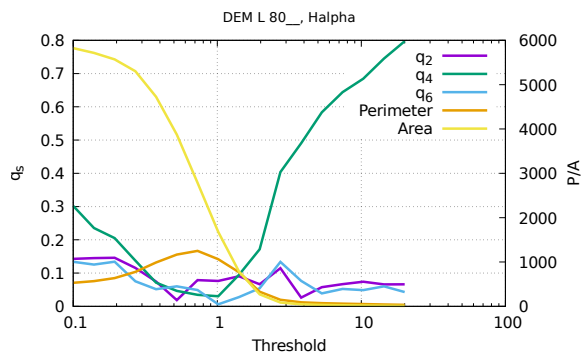
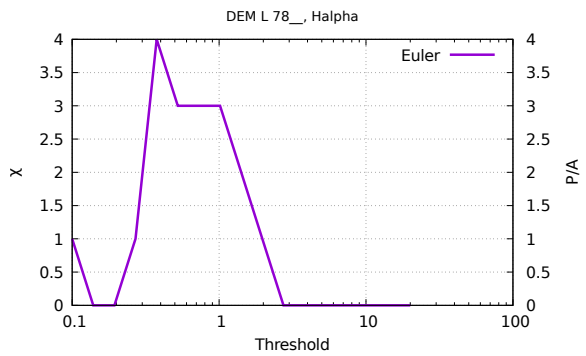
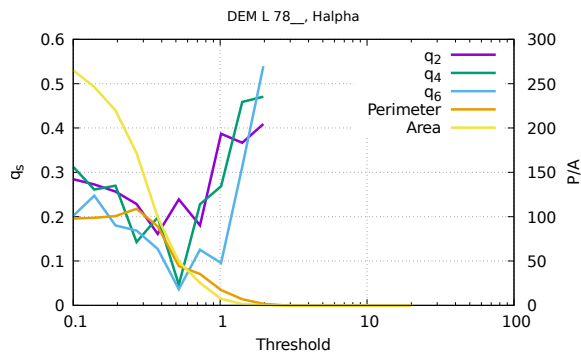
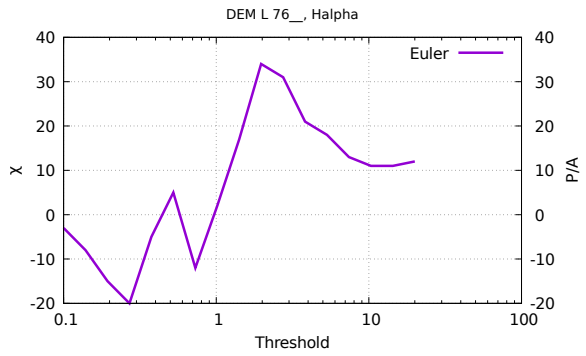
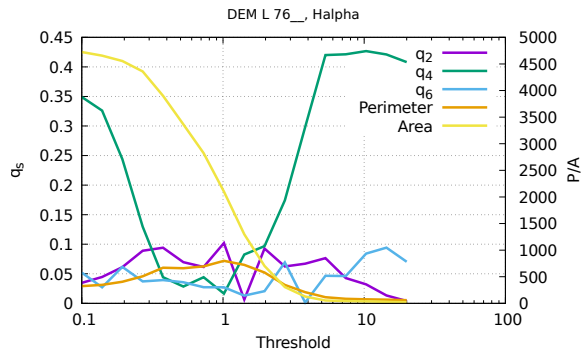


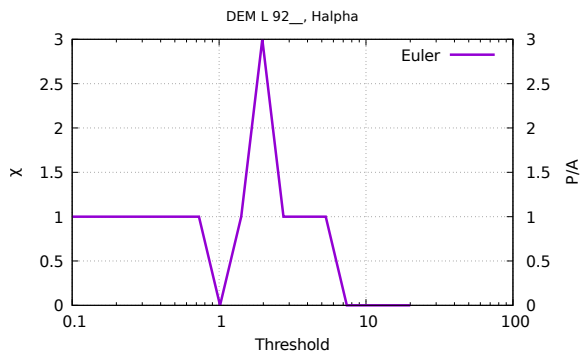
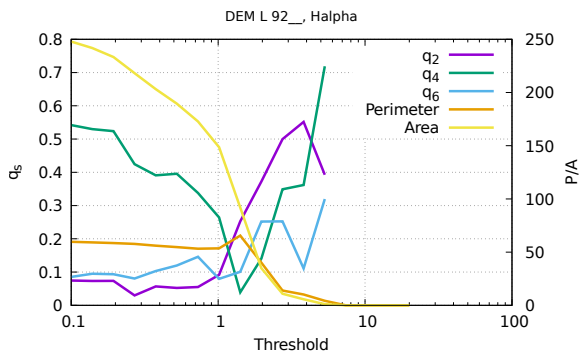
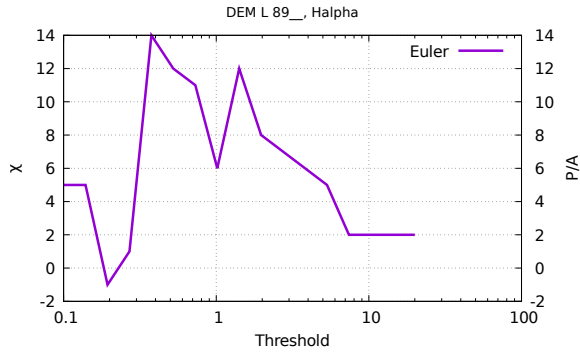
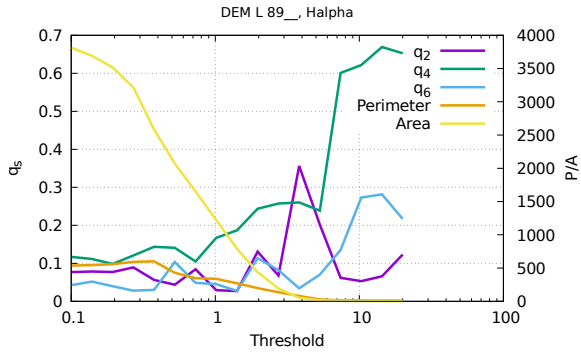
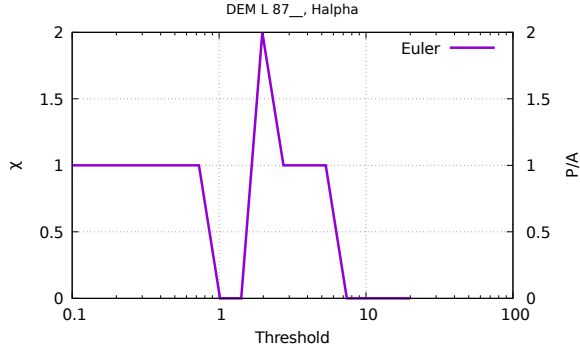
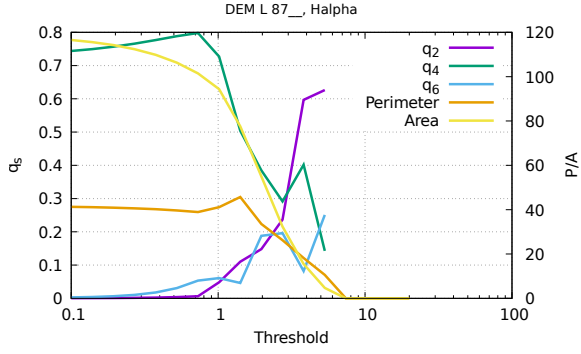
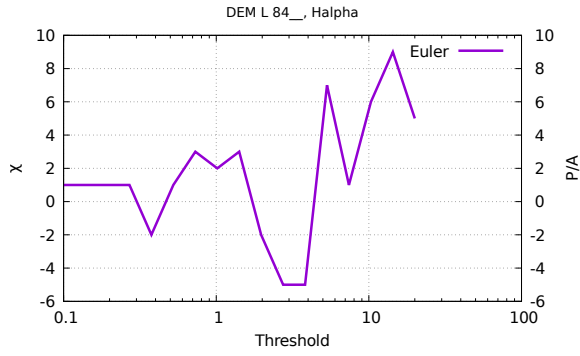
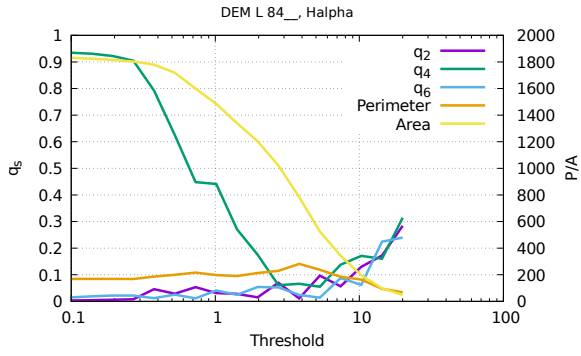












Appendix D

Statistical analysis graphs

The following pages contain the graphs of Ripley's L and the pair correlation function from section 3.2.2 with additional pointwise and three standard deviation envelopes.

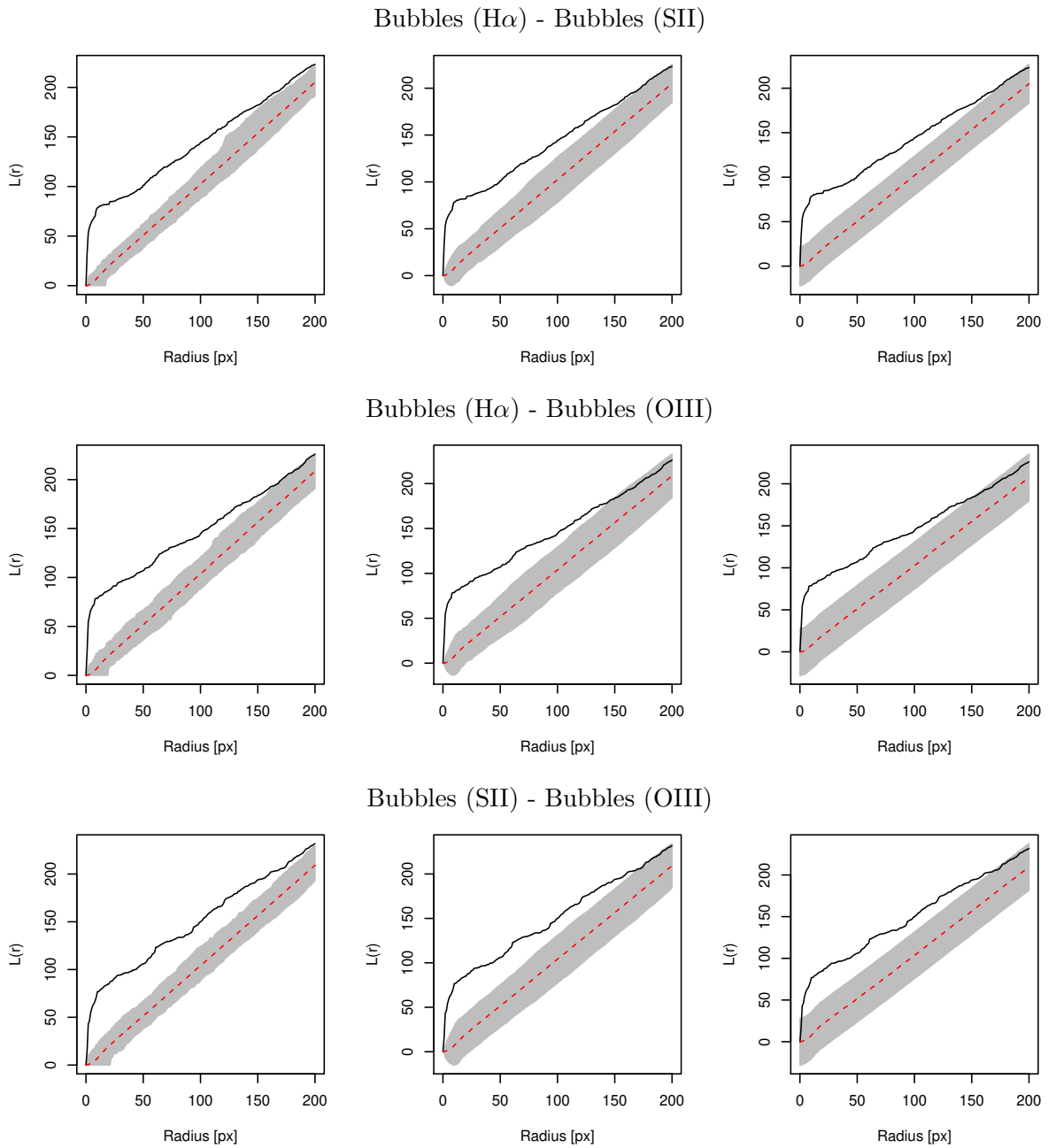
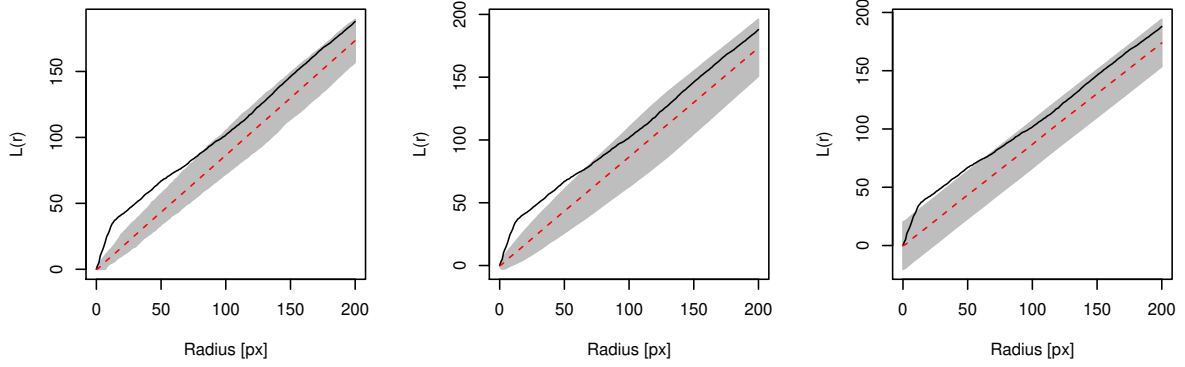
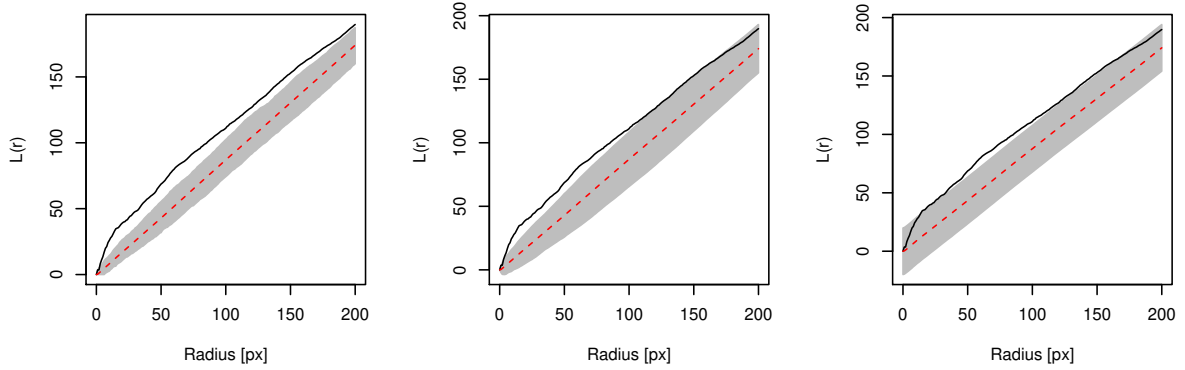


Figure D.1: Bivariate Ripley's L comparing LMC bubbles detected in $H\alpha$ and SII (top), $H\alpha$ and OIII (middle), and SII and OIII (bottom). Black solid line: L estimated from original pattern, Red dashed line: pointwise mean of simulated patterns, Grey envelopes: pointwise (left)/three standard deviations (center)/MAD (right). For a detailed explanation of methods see Sec. 3.2.1.

Bonanos et al. (2009) - Bubbles ($H\alpha$)



Bonanos et al. (2009) - Bubbles (SII)



Bonanos et al. (2009) - Bubbles (OIII)

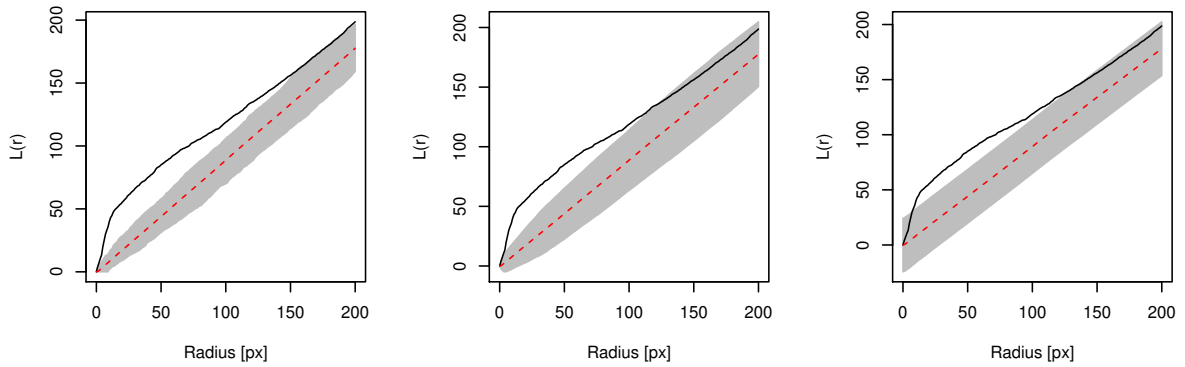
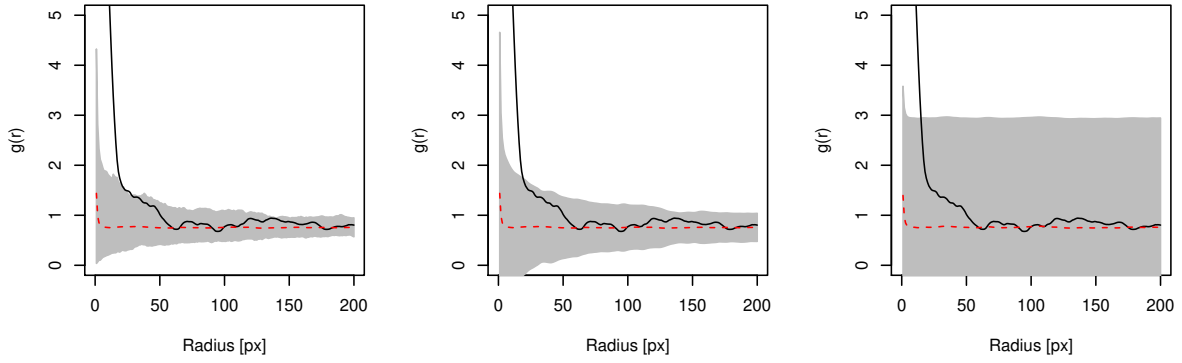
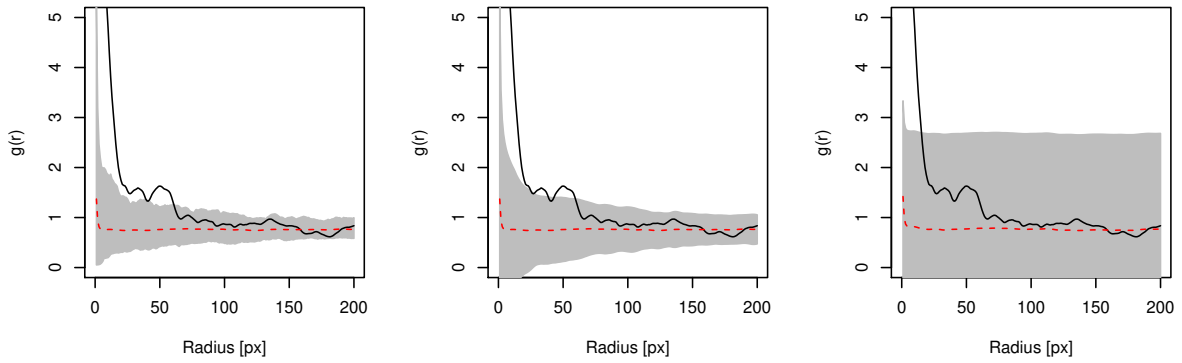


Figure D.2: Bivariate Ripley's L comparing stars in Bonanos et al. (2009) and LMC bubbles detected in $H\alpha$ (top), SII (middle), and OIII (bottom). Black solid line: L estimated from original pattern, Red dashed line: pointwise mean of simulated patterns, Grey envelopes: pointwise (left)/three standard deviations (center)/MAD (right). For a detailed explanation of methods see Sec. 3.2.1.

Bonanos et al. (2009) - Bubbles ($H\alpha$)



Bonanos et al. (2009) - Bubbles (SII)



Bonanos et al. (2009) - Bubbles (OIII)

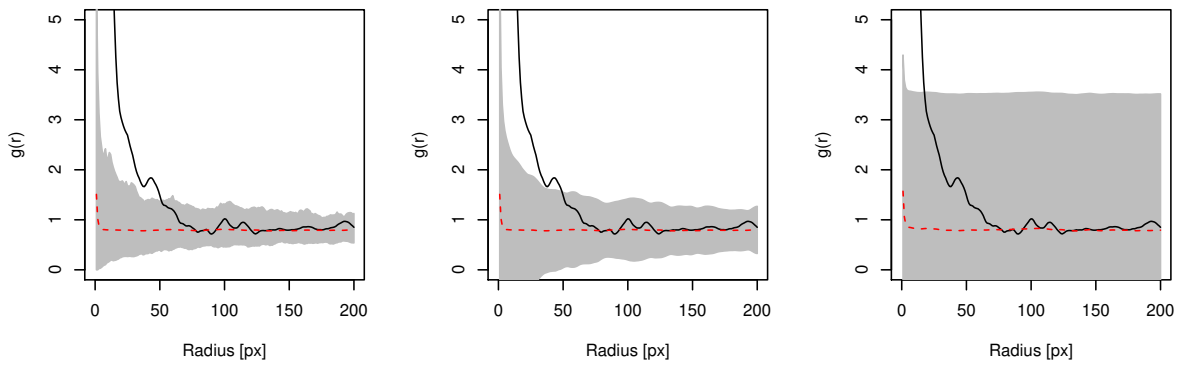
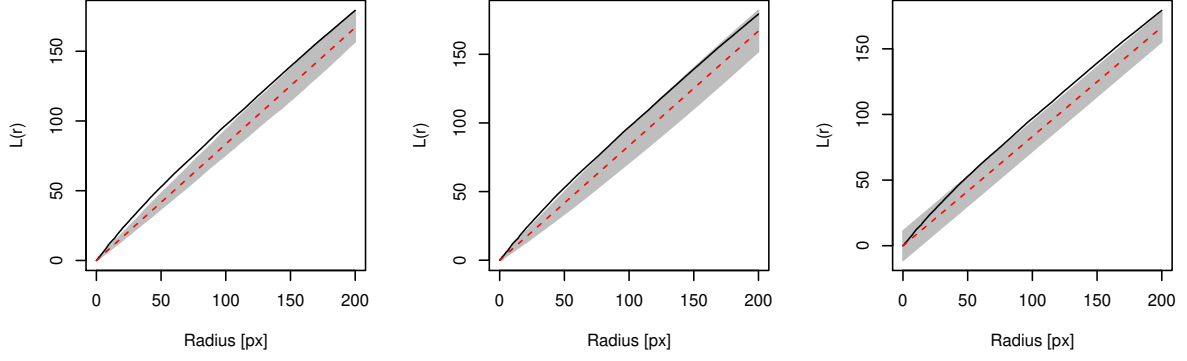
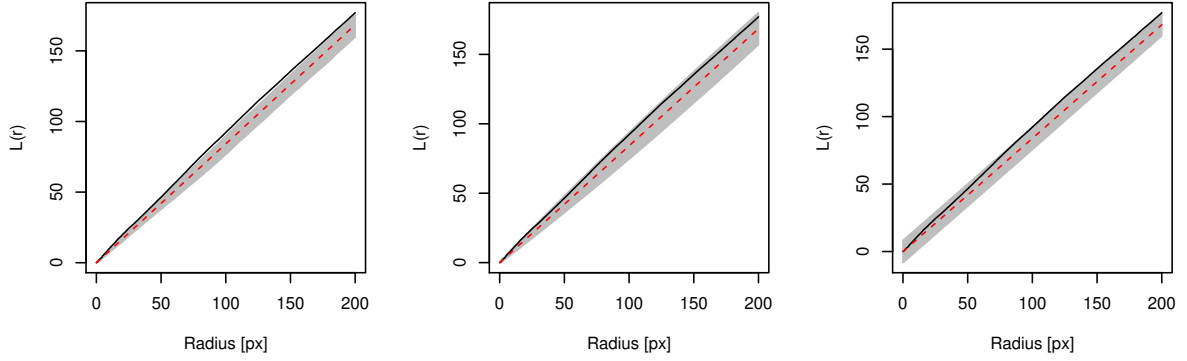


Figure D.3: Cross-correlation function g comparing stars in Bonanos et al. (2009) and bubbles detected in $H\alpha$ (top), SII (middle), and OIII (bottom). Black solid line: g estimated from original pattern, Red dashed line: pointwise mean of simulated patterns, Grey envelopes: pointwise (left)/three standard deviations (center)/MAD (right). For a detailed explanation of methods see Sec. 3.2.1.

Bonanos et al. (2009) - Line density 70 ($H\alpha$)



Bonanos et al. (2009) - Line density 70 (SII)



Bonanos et al. (2009) - Line density 70 (OIII)

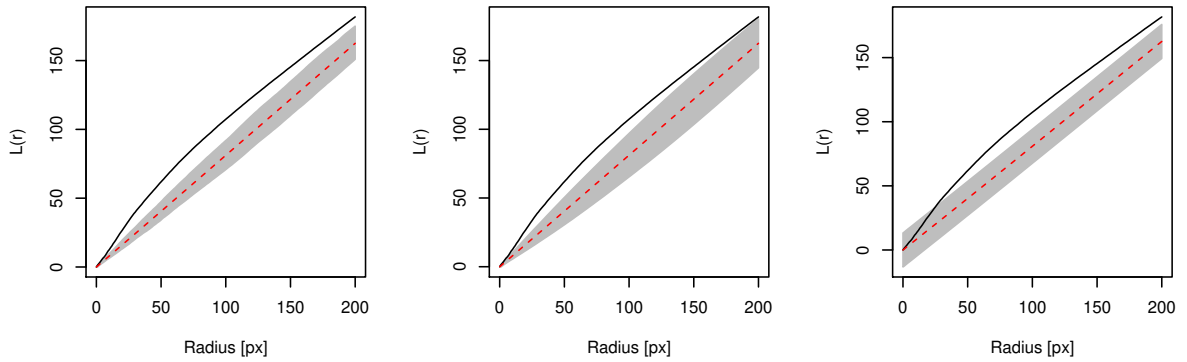
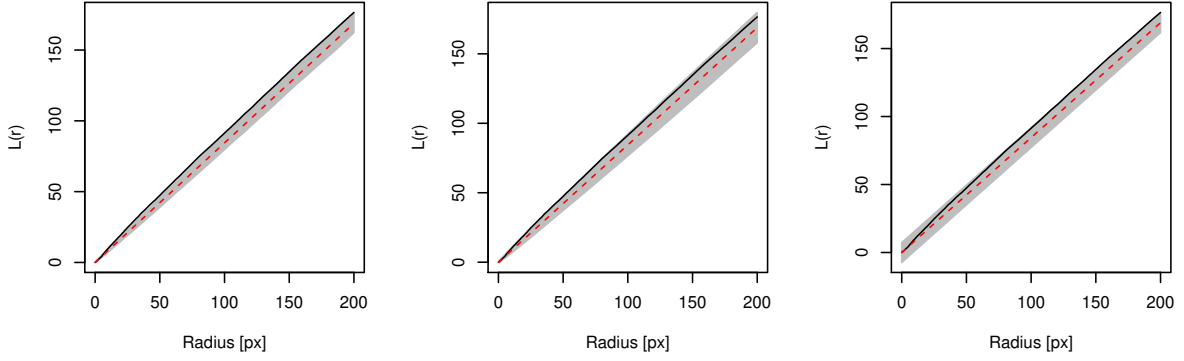
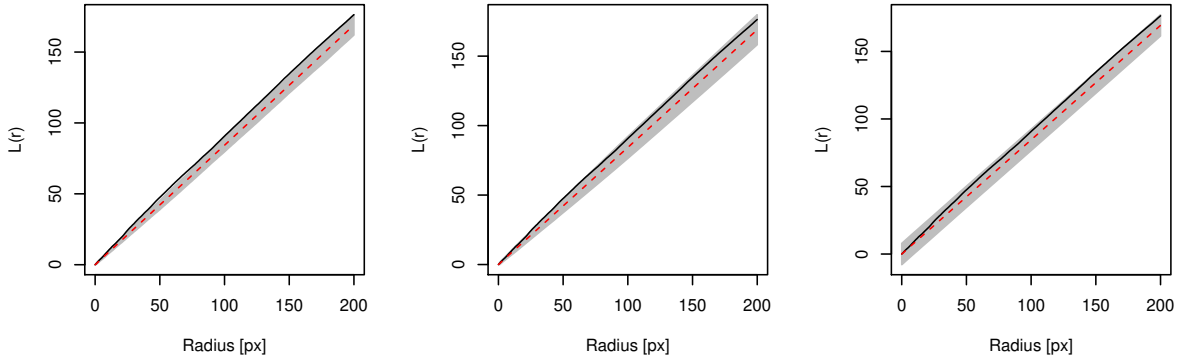


Figure D.4: Bivariate Ripley's L comparing stars in Bonanos et al. (2009) and LMC line densities at window size 70, $m = 0.3$, in $H\alpha$ (top), SII (middle), and OIII (bottom). Black solid line: L estimated from original pattern, Red dashed line: pointwise mean of simulated patterns, Grey envelopes: pointwise (left)/three standard deviations (center)/MAD (right). For a detailed explanation of methods see Sec. 3.2.1.

Bonanos et al. (2009) - Line density 250 ($H\alpha$)



Bonanos et al. (2009) - Line density 250 (SII)



Bonanos et al. (2009) - Line density 250 (OIII)

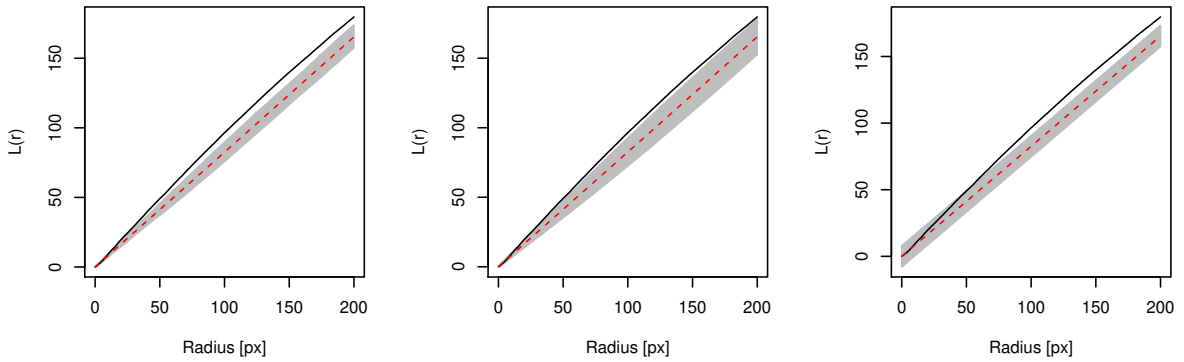


Figure D.5: Bivariate Ripley's L comparing stars in Bonanos et al. (2009) and LMC line densities at window size 250, $m = 0.4$, in $H\alpha$ (top), SII (middle), and OIII (bottom). Black solid line: L estimated from original pattern, Red dashed line: pointwise mean of simulated patterns, Grey envelopes: pointwise (left)/three standard deviations (center)/MAD (right). For a detailed explanation of methods see Sec. 3.2.1.

Selbstständigkeitserklärung

Hiermit bestätige ich, dass ich diese Arbeit selbstständig und nur unter Verwendung der angegebenen Hilfsmittel angefertigt habe.

Erlangen, _____

Unterschrift